# ON THE SELECTION OF MATERIAL MODEL FOR 3D PRINTED PLASTICS

**A Thesis Submitted to**
**The Graduate School of Engineering and Sciences of**
**Izmir Institute of Technology**
**in Partial Fulfillment of the Requirements for the Degree of**

**MASTER OF SCIENCE**

**in Mechanical Engineering**

**by**
**Berika YORULMAZLAR**

**June 2021**

**İZMİR**

# ACKNOWLEDGMENTS

First I would like to express my gratitude to my supervisor, Prof. Dr. Alper TAŞDEMİRCİ for his invaluable advice, continuous support, and also for giving me opportunity to work in the Dynamic Testing and Modelling Laboratory. His immense knowledge and plentiful experience have encouraged me in my academic research and helped me to fulfill my master's thesis. I would also like to thank Prof. Dr. Mustafa GÜDEN and Assoc. Prof. Dr. Hatice Seçil ARTEM for their theoretical knowledge and valued support during my study.

I am also grateful to my colleagues Mesut BAYHAN, Ozan BALYA, Ayda RAMYAR, Semih Berk SEVEN for their support and patient answers to all of my questions and the team of the Dynamic Testing and Modeling Laboratory; Muhammet ÇELİK, Çağatay ALBİR, Mustafa Kemal SARIKAYA and Kaan ZEYBEK for the cherished time spent together in the lab.

I owe gratefulness to my best friends Tuğba, Seren and Nazlı for their emotional support and encouragement. I am also grateful to my dearest friend Bolkar, for believing in me even when I don't believe myself.

Furthermore, my family deserves the better expression of my gratefulness, my father Ceyhun, my sister Özge and my nephew Ayas for loving me and trusting me unconditionally. I dedicate my thesis to my mother Yasemin. I can not make amends for all her labor but I will try for it all my life .

# ABSTRACT


## ON THE SELECTION OF MATERIAL MODEL FOR 3D PRINTED PLASTICS

In this study, the behavior of suitable material models which fulfil the need of representation of static and dynamic constitutive behavior ABS plastic produced with Fused Deposition Modeling (FDM) method was investigated. The accuracy of material model strongly depends on the accurate determination of its constants. These constants were obtained by conducting quasi-static and high strain rate experimental studies. The high strain rate tests of FDM built ABS samples were performed using split-Hopkinson pressure bar (SHPB) and split-Hopkinson tension bar (SHTB) and gas gun set-ups. Numerical models were conducted by using the commercial explicit finite element code LS-DYNA 971. Raw data obtained from experiments at low and high strain rates, were reduced and defined in material models. MAT_24, MAT_81, MAT_187 material models were considered in numerical models to investigate the constitutive behavior of the FDM built ABS material. Good correlation was observed between the numerical and experimental data with the use of selected material models. Then, Generalized Incremental Stress-State dependent damage Model (GISSMO) was selected to characterize the failure behavior of the FDM built ABS. Parameters and curves that defines the state necking and failure occurs at, were found by using optimisation tool, LS-OPT. After observing successful match between the numerical and experimental force-displacement curves, GISSMO parameters were defined in SHTB and gas gun numerical models. The results showed good correlation for also the gas gun and SHTB tests in terms of failure behavior, eventually. These imply that GISSMO has the potential to predict necking and localization of deformation of the 3D-printed ABS plastics for different load cases.

# ÖZET

## ÜÇ BOYUTLU YAZICI KULLANILARAK ELDE EDİLEN PLASTİKLER İÇİN MALZEME MODELİ SEÇİMİ

Bu çalışmada, eriyik yığma modelleme (Fused Deposition Modeling) (FDM) metodu ile üretilmiş ABS plastiğinin statik ve dinamik yapısal davranışının temsili ihtiyacını karşılayan uygun malzeme modellerinin davranışı incelenmiştir. Malzeme modelinin doğruluğu büyük ölçüde sabitlerinin doğru belirlenmesine bağlıdır. Bu sabitler yarı-statik ve yüksek gerinim hızlı deneysel çalışmalar yapılarak elde edilmiştir. Eklemeli üretim ile üretilmiş ABS numunelerinin yüksek gerilme deformasyonu testi, split-Hopkinson basma ve split-Hopkinson çekme barlarında gerçekleştirilmiştir. Nümerik modeller, açık sonlu elemanlar kodu LS-DYNA 971 kullanılarak oluşturulmuştur. ABS malzemenin yapısal davranışını incelemek amacıyla, nümerik modellerde MAT_24, MAT_81, MAT_187 malzeme modelleri ele alınmıştır. Daha sonra, eklemeli üretimle üretilmiş ABS malzemenin hasar karakteristiğini tanımlamak amacıyla Generalized Incremental Stress-State dependent damage Model (GISSMO) hasar modeli ele alınmıştır. Boyun verme ve kopma oluştuğunu tanımlayan parametreler ve eğriler optimizasyon aracı, LS-OPT kullanılarak bulunmuştur. Nümerik ve deneysel kuvvet-yer değiştirme eğrileri arasındaki başarılı eşleşme gözlemlendikten sonra, GISSMO parametreleri SHTB ve gaz tabancası modellerinde tanımlanmıştır. Sonuçlar, nihayetinde gaz tabancası ve SHTB testleri için de hasar kriteri açısından iyi bir bağıntı göstermiştir. Bunlar, GISSMO'nun farklı yük durumları için FDM ile üretilmiş ABS plastiklerin boyun verme ve deformasyonun lokalizasyonunu doğru modelleme potansiyeline sahip olduğu anlamına gelmektedir.

# TABLE OF CONTENTS

LIST OF FIGURES ..... vi
LIST OF TABLES ..... xi
CHAPTER 1 INTRODUCTION ..... 1
1.1. Introduction ..... 1
1.2. Literature Review ..... 5
1.3. Aim and Scope of the Study ..... 21
CHAPTER 2 PRODUCTION OF THE SPECIMENS AND EXPERIMENTAL METHOD ..... 23
2.1. Introduction ..... 23
2.2. Manufacturing of Specimens by FDM ..... 23
2.3. Experimental Method ..... 26
2.3.1. Quasi-static Testing ..... 26
2.3.2. Dynamic Testing ..... 28
CHAPTER 3 NUMERICAL MODELING ..... 33
CHAPTER 4 EXPERIMENTAL RESULTS AND CHARACTERIZATION ..... 48
4.1. Introduction ..... 48
4.2. Experimental Results ..... 48
4.2.1 Quasi-static Tension and Compression Test Results ..... 48
4.2.2 High Strain Rate Tension and Compression Tests ..... 53
4.3 Numerical Results ..... 55
4.3.1. Integration of GISSMO ..... 62
4.3.1.1. Double Notched ..... 65
4.3.1.2. Notched ..... 67
4.3.1.3. Shear 0$^{o}$ ..... 69
4.3.1.4. Shear 60$^{o}$ ..... 71
4.3.1.5 Shear 45$^{o}$ ..... 72
4.3.1.6 Mini Tensile ..... 74
CHAPTER 5 CONCLUSIONS ..... 80
REFERENCES ..... 82

# LIST OF FIGURES

**Figure** **Page**

Figure 1. Fused Deposition Manufacturing setup (Dizon et al. 2018). ..... 1

Figure 2 Chemical structure of ABS thermoplastic (MacDermott and Shenoy 1997) ..... 3

Figure 3 Applications of ABS plastics (a) Ford Thunderbird instrument panel in ABS (b) CNC Machined ABS Car Bumper ABS Plastic (c) ABS plastic camouflagehelmets. ..... 3

Figure 4 A model of a jet engine for educational purposes. ..... 4

Figure 5. Orientation of ABS specimens. ..... 5

Figure 6. Stress strain curves at quasi-static and high strain rates for different building orientations of ABS specimens ..... 6

Figure 7. Stress-strain curve of the FDM built ABS under compressive load at different strain rates ..... 7

Figure 8 Comparison of elastic modulus for specimens produced with 0.2 mm and 0.4 mm layer thicknesses. ..... 8

Figure 9. Fishbone diagram of potential parameters that effect tensile strength ..... 8

Figure 10 Tensile strength of the FDM produced ABS polymer with various rasterangles. ..... 9

Figure 11. Force vs. displacement curves for 3-point-bending at 2 velocities (quasi-static and dynamic) for the three material models. ..... 10

Figure 12. Comparison of test and simulation results for bending tests (a); tensile tests (b); dynamic bending tensile test (c) and dynamic puncture test (d) ..... 11

Figure 13. Force vs. displacement curves obtained from the experimental test and numerical models with using three different element types. ..... 12

Figure 14. Numerical vs. experimental results of tensile test of ABS with using material model with damage. ..... 13

Figure 15. Model implemented and experimental equivalent plastic strain values. ..... 14

Figure 16. Force–displacement curves of experimental and numerical results. ..... 15

Figure 17 Produced (a) shear $0^o$, (b) shear $45^o$, (c) shear $60^o$, (d) notched, (e) double notched and (f) mini tensile test specimens ..... 16

**Figure** **Page**

Figure 18. Force displacement curves for the (a) shear 0° (b) shear 45° (c) shear 60° (d) notched (e) double notched (f) mini tensile specimens both experimental data and the GISSMO simulation (D. Hörling 2015). ..... 18
Figure 19. Force displacement curves for the (a) shear 0° (b) shear 45° (c) notched (d) double notched (e) mini tensile specimens both experimental data and the GISSMO simulation ..... 20
Figure 20 The dog-bone ABS specimen that is printed using FDM method according to ASTM D638-03 for quasi-static tensile testing. ..... 24
Figure 21 Custom ABS specimen that is printed using FDM method for quasi-static and dynamic tensile testing. ..... 25
Figure 22 Cylindrical ABS specimen that is printed using FDM method for quasi-static and dynamic compression testing. ..... 25
Figure 23 a) Shear60$^{o}$, b) shear45$^{o}$, c) shear 0$^{o}$, d) double notched, e) notched, f) mini tensile ABS specimens that were printed using FDM method for GISSMO analyzes ..... 26
Figure 24 Quasi-static a) tension b) compression test set-up ..... 28
Figure 25 Split Hopkinson (a) tension (b) compression bar setup ..... 29
Figure 26 An example to a voltage-time curve for SHPB test of ABS polymer ..... 30
Figure 27 Gas gun test set-up. ..... 32
Figure 28 Specimen holder. ..... 32
Figure 29 The von Mises yield surfaces in principal stress coordinates circumscribes a cylinder (Bertarelli 2016). ..... 34
Figure 30 Table of curves defined to account strain rate effects. ..... 35
Figure 31 LS-PREPOST material keyword of the *MAT_24 material used in the simulations. ..... 35
Figure 32 Von Mises stress as a function of pressure ..... 36
Figure 33 LS-PREPOST material keyword of the *MAT_187 material used in the simulations. ..... 36
Figure 34 Effect of fading exponent (Neukamm, Feucht, and Haufe 2009). ..... 39
Figure 35 An example to a convergence process in LS-OPT ..... 41
Figure 36 The flowchart in LS-OPT® describing the combined optimization. ..... 42

**Figure** **Page**

Figure 37 (a) Stress-strain curves for the compression with different element sizes (b) compression specimens meshed with 2, 1, 0.4 and 0.2 mm element size. ..... 43
Figure 38 Custom tensile specimens meshed with 1 mm and 0.4 mm element size. ..... 44
Figure 39 Quasi-static tensile (a) and compression (b) models. ..... 45
Figure 40 SHTB and SHPB models. ..... 45
Figure 41 Gas gun model. ..... 47
Figure 42 Stress-strain curves of the material obtained from quasi-static tensile tests at (a) $10^{-3}$ $s^{-1}$s, (b) $10^{-2}$ $s^{-1}$, and (c) 10-1 s-1 strain rates. ..... 50
Figure 43 Comparison of tensile stress-strain curves at $10^{-3}$ $s^{-1}$, $10^{-2}$ $s^{-1}$, and $10^{-1}$ $s^{-1}$ strain rates. ..... 51
Figure 44. Stress-strain curves of FDM built ABS obtained from quasi-static compression tests at (a) 10-3 $s^{-1}$ s, (b) $10^{-2}$ $s^{-1}$, and (c) $10^{-1}$ $s^{-1}$ strain rates ..... 52
Figure 45 Comparison of compressive stress-strain curves at different strain rates ..... 53
Figure 46 Comparison of tensile stress-strain curves obtained from SHTB at different strain rates ..... 53
Figure 47 Comparison of compressive stress-strain curves obtained from SHPB at different strain rates ..... 54
Figure 48 Comparison of material models for quasi-static tensile test ..... 55
Figure 49 The D638 specimen at failure states (a) *MAT_24 (b) *MAT_81 (c) *MAT_187 (d) experiment. ..... 56
Figure 50 Comparison of material models for quasi-static compression test ..... 57
Figure 51 Comparison of material models for dynamic tensile test ..... 57
Figure 52 Failure states at STHB test, numerical and experimental comparison (a) *MAT_24 (b) *MAT_81 (c) *MAT_187 (d) experiment. ..... 59
Figure 53 Comparison of material models for dynamic compression test. ..... 59
Figure 54 Front and back face of the deformed ABS plate. ..... 60

**Figure** **Page**

Figure 55 Comparison of initial and final velocity of the projectile for (a) MAT_24 and (b) MAT_187 material models for different thickness values. ..... 61
Figure 56 Comparison of SAE-Displacement Graphs for (a) MAT_24 and (b) MAT_187 material models for different thickness values. ..... 62
Figure 57 Flowchart in LS-OPT analysis describing the optimization of shear 60$^o$ case. ..... 63
Figure 58 The GISSMO instability and failure criteria curves for all cases. ..... 64
Figure 59 Experimental vs. single case optimization force–displacement curves of the double notched specimen. ..... 65
Figure 60 Experimental vs. multi case optimization force–displacement curves of the double notched specimen. ..... 66
Figure 61 The state of failure of the double notched specimen in (a) experiment (b) single case optimization and (c) multi case optimization. ..... 66
Figure 62 Experimental vs. single case optimization force–displacement curves of the notched specimen. ..... 67
Figure 63 Experimental vs. multi case optimization force–displacement curves of the notched specimen. ..... 68
Figure 64 The state of failure of the notched specimen in (a) experiment (b) single case optimization and (c) multi case optimization. ..... 68
Figure 65 Experimental vs. single case optimization force–displacement curves of the shear 0$^o$ specimen. ..... 69
Figure 66 Experimental vs. multi case optimization force–displacement curves of the shear 0$^o$ specimen. ..... 70
Figure 67 The state of failure of the shear 0$^o$ specimen in (a) experiment (b) single case optimization and (c) multi case optimization. ..... 70
Figure 68 Experimental vs. single case optimization force–displacement curves of the shear 60$^o$ specimen. ..... 71
Figure 69 Experimental vs. multi case optimization force–displacement curves of the shear 60$^o$ specimen. ..... 72
Figure 70 The state of failure of the shear 60$^o$ specimen in (a) experiment (b) single case optimization and (c) multi case optimization. ..... 72

**Figure** **Page**

Figure 71 Experimental vs. single case optimization force–displacement curves of the shear 45º specimen. ..... 73
Figure 72 Experimental vs. multi case optimization force–displacement curves of the shear 45º specimen. ..... 73
Figure 73 The state of failure of the shear 45º specimen in (a) experiment (b) single case optimization and (c) multi case optimization. ..... 74
Figure 74 Experimental vs. single case optimization force–displacement curves of the mini tensile specimen. ..... 74
Figure 75 Experimental vs. multi case optimization force–displacement curves of the mini tensile specimen. ..... 75
Figure 76 The state of failure of the mini tensile specimen in (a) experiment (b) single case optimization and (c) multi case optimization. ..... 76
Figure 77 Comparison of experimental and numerical (a) true stress strain curves (b) appearance of failure for the SHTB test ..... 77
Figure 78 Experimental and numerical comparison of (a) initial and final velocity of the projectile (b) deformation on the front and back face of the plate. ..... 78

# LIST OF TABLES

**Table** **Page**

Table 1 Features of the MAT_24, MAT_124 and MAT_187 material models (P. Reithofer et al.2018). ..... 9
Table 2 Production process parameters. ..... 23
Table 3 Features of the *MAT_24 *MAT_81 *MAT_187 material models. ..... 38
Table 4 Johnson–Cook material model constants of the hardened steel projectile. ..... 46
Table 5 Mechanical properties of FDM built ABS at quasi-static strain rates. ..... 50
Table 6 The best parameters achieved from LS-OPT® for all cases ..... 64

# CHAPTER 1

# INTRODUCTION

## 1.1. Introduction

Recently, interest in 3D-printing (or Additive Manufacturing (AM)) has been increased considerably. This manufacturing system has the potential of starting an industrial revolution and in the future, machine parts may be produced with this method.

There is also an increase in preference for an AM method, Fused Deposition Modeling (FDM) technology in the manufacturing of prototypes in the last decade due to its inexpensiveness (Macdonald et al. 2014). Due to its easy access and low costs, FDM method is one of the most popular 3D printing processes. FDM technology provides to manufacture components or structures having good mechanical, chemical and thermal resistance (Edgar and Tint 2015) .

Scott Crump who is the founder of the Stratasys patented the FDM in 1989 (Crump 1991). The principle of this manufacturing system is, extruding or melting a material and depositing it onto a platform to create a three dimensional component for the desired shape or the topology (Vaezi, Seitz, and Yang 2013). Generally the material used for the filaments are thermoplastics such as ABS, PC and PLA.

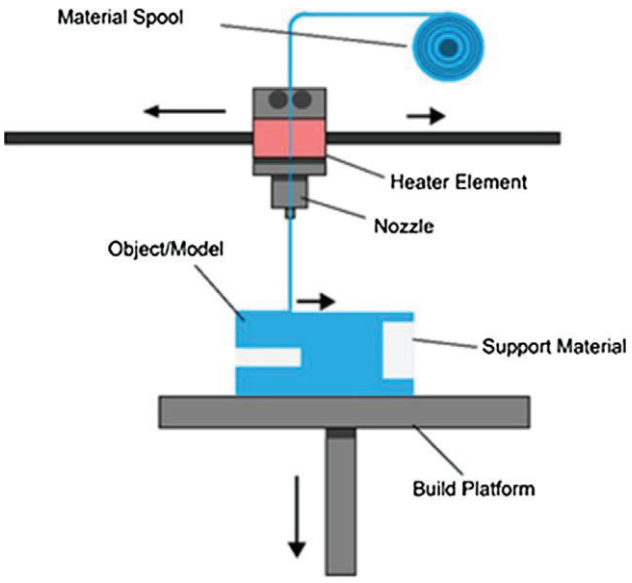


Figure 1. Fused Deposition Manufacturing setup (Source: Dizon et al. 2018).

Figure 1 shows the schematic representation of the FDM setup. As it is seen in the figure, a polymer material is heated through the nozzle and it is printed to a build platform to solidify and this way actual printed model is built from the layers (Wang et al. 2017). The raster patterns on the printing process is predetermined and it follows the geometry of a part. Until a single layer is completed, this process continues in the XY plane, then to create the layers in the Z direction the build platform moves down to produce the objects in three dimensions.

To make the material overcome tension and compression loads and melting operations, high quality fabrication should be preferred in the manufacturing of the objects (Dizon et al. 2018). And also in the manufacturing process, when the design of a geometry is complex, it is required to use support structures (Sood, Ohdar, and Mahapatra 2010).

Polymers produced by FDM are one of the strongest polymers that are additively manufactured (Edgar and Tint 2015). Generally, strength of the plastics are lower than the metals but the density of the plastics are relatively lower than metals and failure strains are higher for the plastics also. Therefore, in many applications plastics could have more advantages considering their inexpensiveness and suitability for complex designs (Kazmer 2017).

Thermoplastics are one of the most preferred materials in FDM system since the mechanical characteristics and manageability at low temperatures of these materials are suitable for the FDM method (Edgar and Tint 2015).

One of the most common thermoplastics that is used in FDM is Acrylonitrile butadiene styrene (ABS) due to its unique properties. ABS is a thermoplastic that is obtained from the polymerization of acrylonitrile and styrene monomers in the presence of butadiene rubber shown in Figure 2.

The advantages of ABS can be listed as high strength and rigidity, its good chemical resistance, good processability and low cost. These properties make the ABS polymer one of the most frequently used thermoplastics in engineering applications.

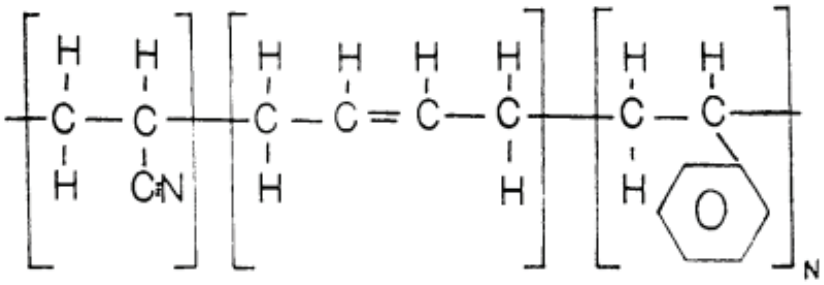

Figure 2 Chemical structure of ABS thermoplastic (Source: MacDermott and Shenoy 1997)

ABS plastics are widely used in many areas. One of the important use of ABS as an engineering plastic is in automotive instrument panels. As it is seen in Figure 3.a ABS was used in a panel because of its low cost and its impact resistance comparing to other materials that were also adequate for the use. Another use of ABS as a car bumper is seen in Figure 3.b. ABS, PC/ABS plastics are generally used to absorb the impact and protect the chrome metal bumper. ABS plastic is also widely used in helmets because it's low cost and it is chemical and heat-resistant (Figure 3.c.).

(a) (b) (c)

Figure 3 Applications of ABS plastics (a) Ford Thunderbird instrument panel in ABS (Source: MacDermott and Shenoy 1997) (b) CNC Machined ABS Car Bumper (Source: https://sgprototype.en.made-in-china.com, 2018) (c) ABS plastic camouflage helmets. (Source: https://www.dhgate.com,2017)

A solid ABS structure can easily be turned into a softer structure when it is heated to high temperatures without melting into a viscous liquid which makes it advantageous in the use of FDM systems. Some studies stated that the low strength of the FDM built ABS compared to the injection molded ABS can be compensated by good compliance properties.(Croccolo, De Agostinis, and Olmi 2013) FDM built ABS polymers can be used to manufacture complex parts such as automotive and aerospace prototypes. NASA

and several air force bases use 3D printers to prototype tools for educational purposes for astronauts working on the International Space Station (Figure 4). FDM built ABS parts can also be used as interim parts or tools until permanent replacements are available.

Figure 4 A model of a jet engine for educational purposes (Source: https://www.3dhubs.com).

It is important to know the mechanical behavior of a material when designing mechanical and structural components. With the advancement of computer technology, finite element analysis (FEA) has become a popular method for predicting structural deformations and stress distributions of the materials.

FEA tools such as LS-DYNA, can be used in the modeling of the behavior of materials under static and dynamic loadings. For these applications, material models which are dependent on the stress, strain rate and temperature are required to describe the material responses for different loading conditions. So that the stress, strain values could be calculated through the governing equations and conservation laws (Zhang, Chen, and Liu 2017).

In these applications reliability of the calculations relies on the definition of material model parameters. To obtain the parameters and constants for the material models an extensive data of the static and dynamic properties of materials are required.

One of the key process in finite element analysis is the selection of material model. When finite element models are created to conduct stress analysis for designs, among a library of material models correctly representing constitutive behavior needs to be selected. The accuracy of material model strongly depends on the accurate determination

of its constants. These constants can be obtained by conducting experimental studies. The aim of this study is to investigate the behavior of material models available in LS-DYNA that already been implemented for polymers and plastics for the use of FDM built materials.

## 1.2. Literature Review

Some studies have been carried out to investigate the effect of building direction and strain rate effects on material strength and behavior. High strain rate tests of the FDM built ABS parts have been mainly conducted using Split Hopkinson Pressure Bar (SHPB). Jami et al. investigated dynamic behavior of ABS parts manufactured with FDM in vertical, horizontal at $0^o$ and horizontal at $45^o$ build-up orientations. In this study, in order to determine stress-strain curve at the high strain rates, cylindrical ABS specimens were manufactured by an FDM machine. Produced parts in three different build orientations are shown in Figure 5. They also studied the effect of building orientations on the parts evaluating dynamic and quasi-static strain rate mechanical properties.

In the study, high strain rate compression tests were performed by using Split Hopkinson Pressure bar apparatus. Also quasi-static compression tests were conducted on the same specimens with a speed of 1 mm/min.

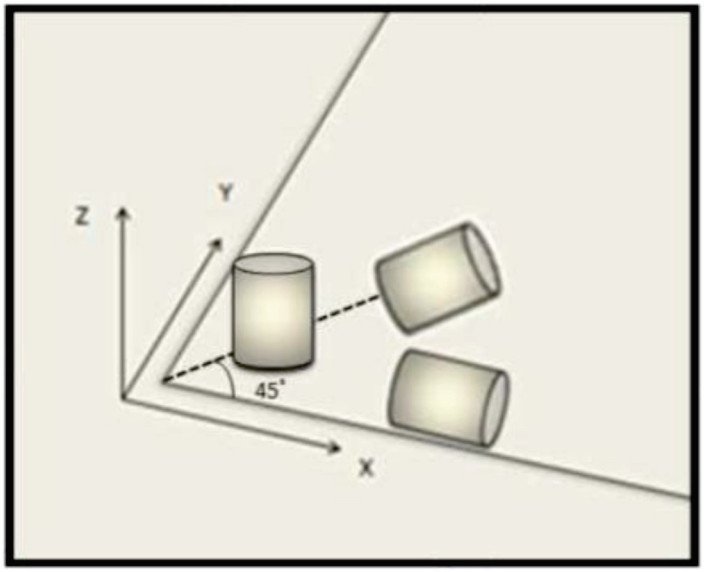


Figure 5. Orientation of ABS specimens (Source: Jami, Masood and Song 2013).

They reported that (Figure 6) build orientation is an effective parameter for both of the dynamic response of the parts under compressive loads. And they reported good capability of the FDM built ABS parts under dynamic loading conditions.(Jami, Masood, and Song 2013).

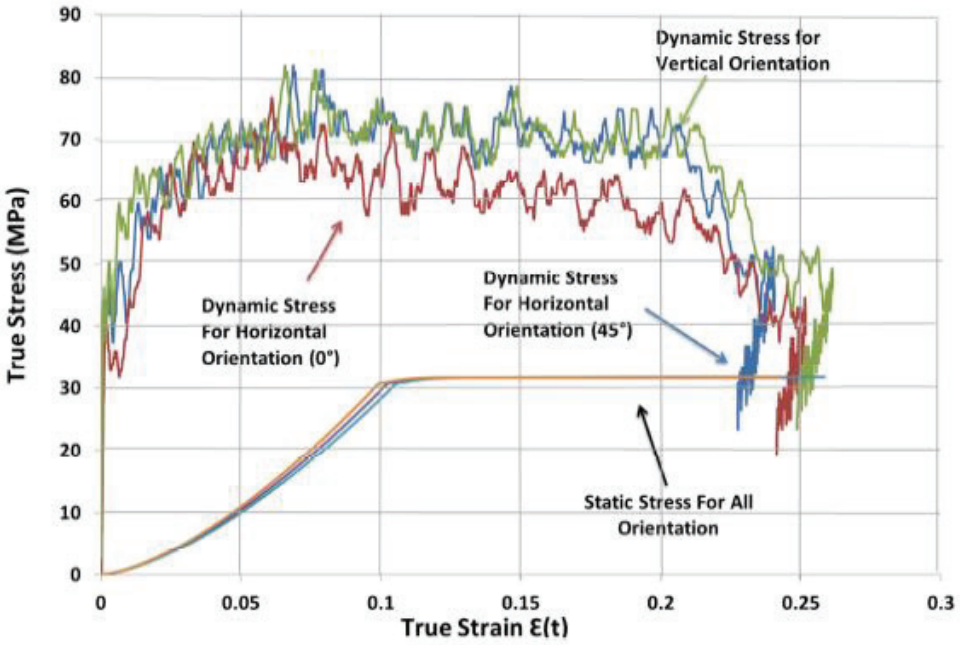


Figure 6. Stress strain curves at quasi-static and high strain rates for different building orientations of ABS specimens (Source: Jami, Masood, and Song 2013)

In order to investigate the anisotropy of the shear properties of the FDM built ABS and PC parts, Cantrell et al. investigated experimental methods and results for the mechanical characterization. It was observed that build orientation was an important parameter for the the modulus of rigidity and shear strength. In the study, while anisotropy was found to be a function of the build orientation for the ABS material, for the PC material it was found to be a function of raster orientation(Cantrell et al. 2017).

Potential energy absorption benefits of FDM built ABS specimens were investigated by Peterson et al. In order to investigate strain rate dependency of the material, quasi-static and dynamic compression tests were conducted. Split Hopkinson Pressure Bar used to investigate the stress-strain response of the material at high strain rates.

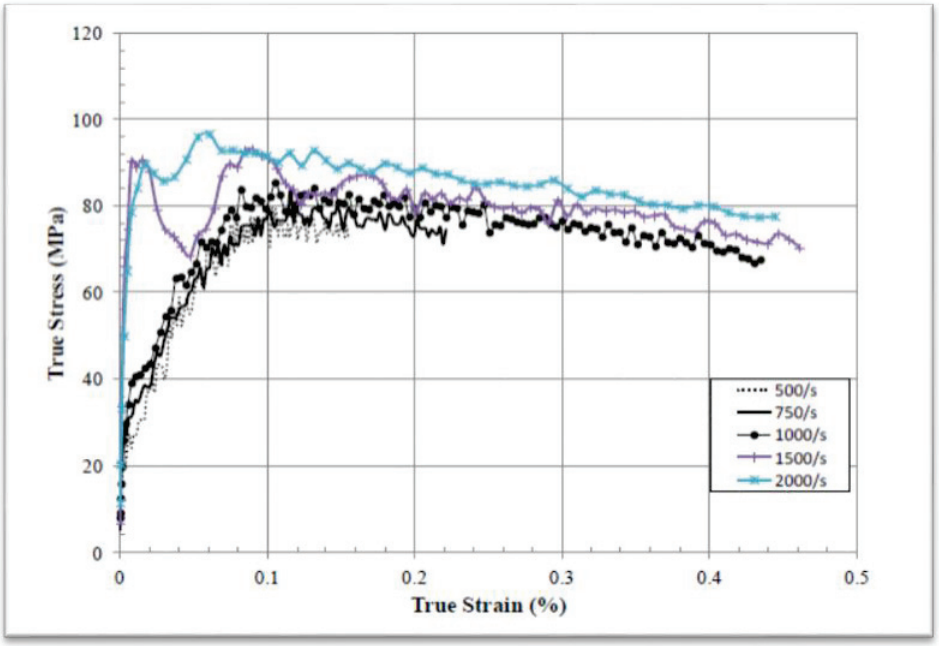


Figure 7. The Stress versus strain curve of the FDM built ABS under compressive load at different strain rates (Source: Peterson et. al. 2015)

Results showed that (as seen in Figure 7) as strain rate was increased from 500/s to 2000/s, plastic deformation and stress values was increased as well. The deformation behavior of the specimens under compressive load at lower strain rates implied a potential for a energy absorption mechanism. It was seen that strain rate effects have influence on the compression strength of the specimen (Peterson et al. 2015).

Diaconescu et al. tested ABS parts produced with FDM under tensile loadings. They investigated different raster angles and concluded that tensile strength of parts manufactured using $45^o/45^o$ raster angle was higher than the parts manufactured using $0^o/90^o$ raster angle (Diaconescu, Tabacu, and Oltean 2017).

Layer thickness effects on the mechanical behavior of the FDM built ABS parts was investigated by Rankouhi et al. Comparison of parts printed with 0.2 mm and 0.4 mm layer thickness was conducted. They reported that, as it is seen in Figure 8, tensile strength and elastic modulus higher in samples produced with 0.2 mm layer thickness than the specimens produced with 0.4 mm layer thickness. This was attributed to the reason of observing air gaps in specimens that was fabricated with the 0.2 mm in layer thickness (Rankouhi et al. 2016).

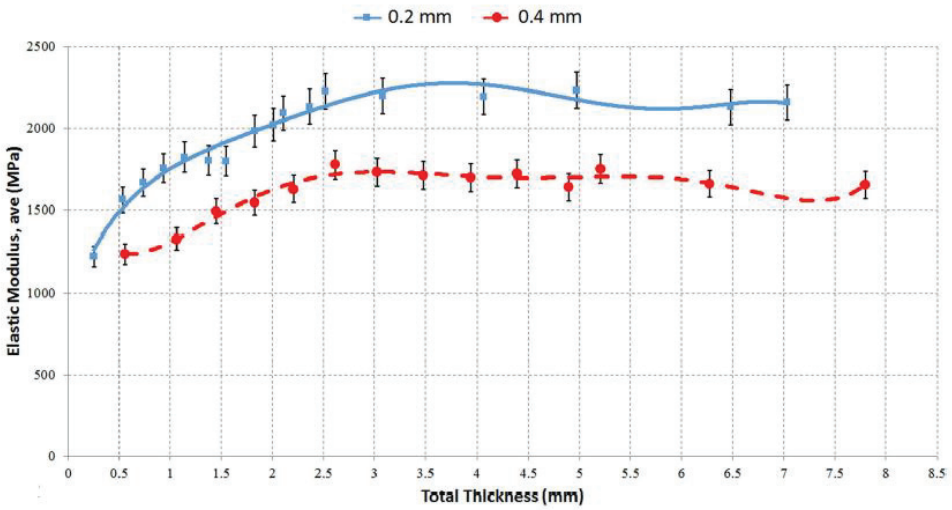


Figure 8 Comparison of elastic modulus for specimens produced with 0.2 mm and 0.4 mm layer thicknesses (Source: Rankouhi et al 2016).

Ahn et al. used a Design of Experiment method to investigate the production parameter effects on the mechanical properties of ABS parts produced using FDM (Figure 9).

As it is seen in Figure 10 they reported that the tensile strength of the FDM built ABS was higher than the strength of injection molded ABS and they observed that strength of the FDM parts were dependent in the raster direction.

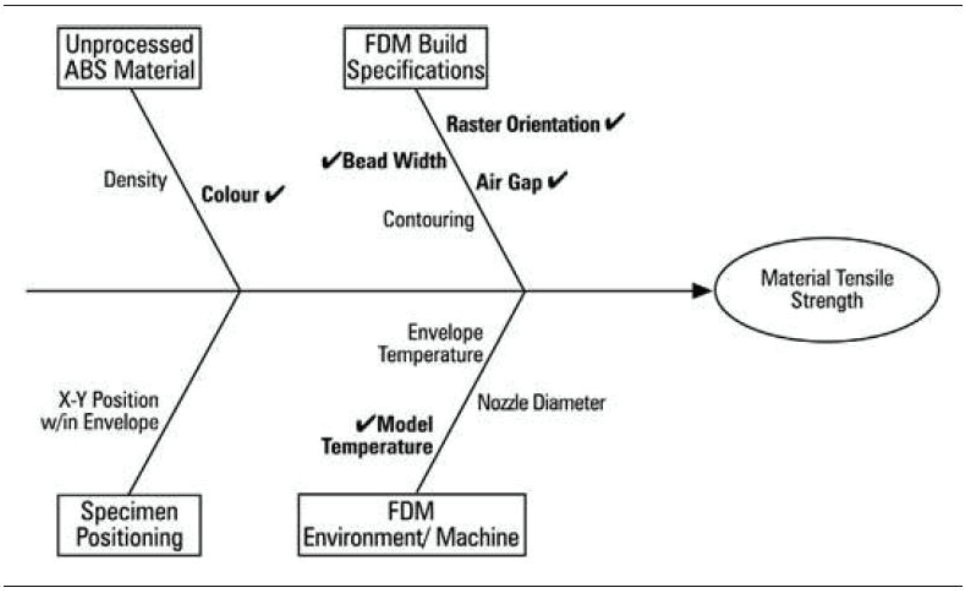


Figure 9. Fishbone diagram of potential parameters that effect tensile strength (Source: Ahn et al. 2002)

FDM built ABS specimens exhibited anisotropic characteristics unlike the injection molded ABS. At final, they presented some build rules these were; if the specimens will be subjected to tensile loads, the highest strength would be obtained along the fibers. At the sharp transition to the radiused corners stress concentrations would be observed. Failure strains are higher under the compressive loads rather than under the tensile loads (Ahn et al. 2002).

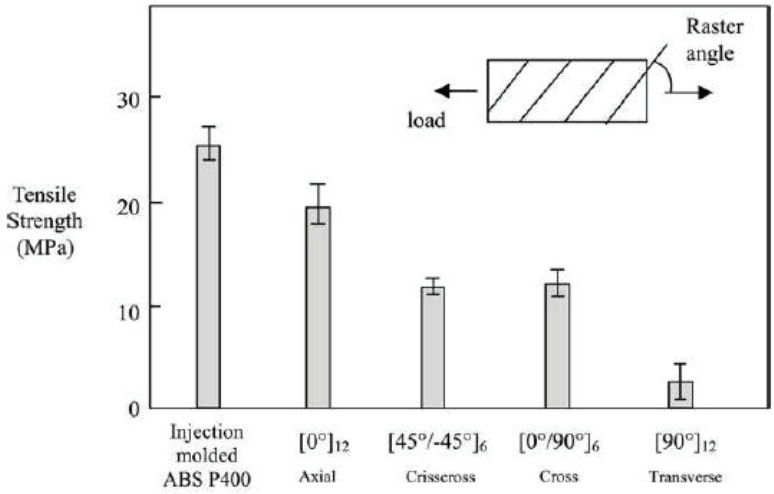


Figure 10 Tensile strength of the FDM produced ABS polymer with various raster angles (Source: Ahn et al. 2002).

There are some studies investigating and comparing the material models for thermoplastics in literature. In the study of Reithofer et al. the individual advantages and disadvantages of the *MAT_24, *MAT_124 and *MAT_187 material models in predicting the behavior of plastics under different states of loadings were investigated.

Table 1 Features of the MAT_24, MAT_124 and MAT_187 material models (Source: P. Reithofer et al.2018).

| Material model | Yield surface | Visco-elasticity | Visco-plasticity | comp./tension symmetry | plastic Poisson's ratio |
|---|---|---|---|---|---|
| ***MAT_024** | von Mises | × | ✓ | × | 0.5 |
| ***MAT_124** | 2x von Mises | ✓ Pronyseries | ✓ | ✓ | 0.5 |
| ***MAT_187** | General over triaxiality | ✓ Table | ✓ | ✓ | ✓ |

They presented features of the *MAT_24, MAT_124, MAT_187 material models with not considering failure (Table 1).

Results were obtained from static and dynamic tension bending test and compared with the simulation results. As it is seen from Figure 11 that results were quite accurate, in terms of peak force and failure. In the case of the dynamic tests, they observed that *MAT_024 failed to simulate this test as the other material models.

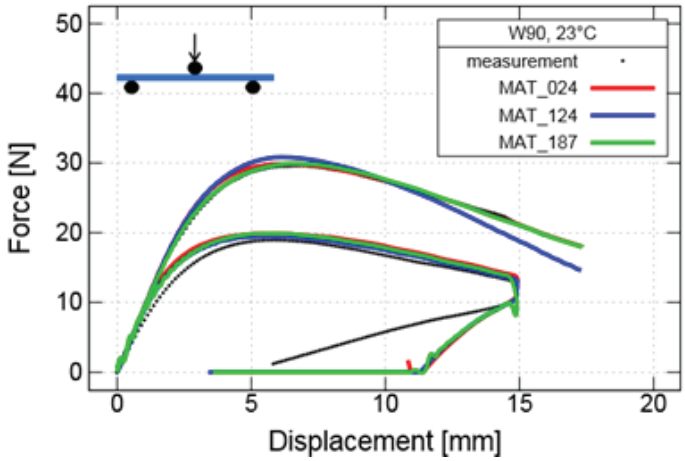


Figure 11. Force vs. displacement curves for the bending at quasi-static and high strain rates for the three material models (Source: P. Reithofer et al.2018).

Then, to obtain more accurate results in terms of plastic deformation the *MAT_ADD_ GISSMO was implemented to *MAT_187 and results were compared for the bending, tensile, dynamic bending tensile and dynamic puncture tests (Figure 12).

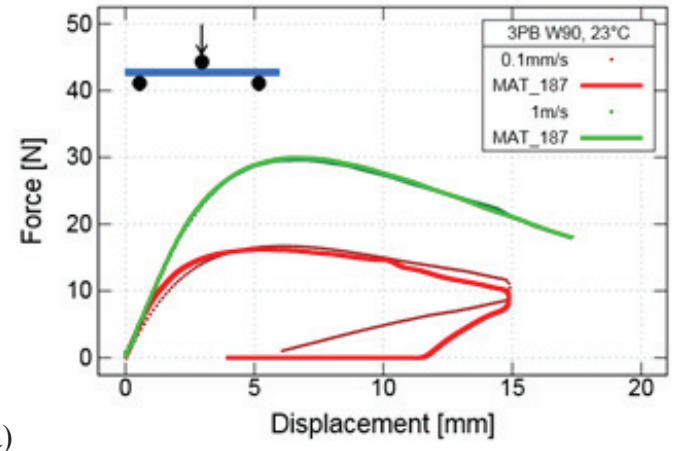


(a)

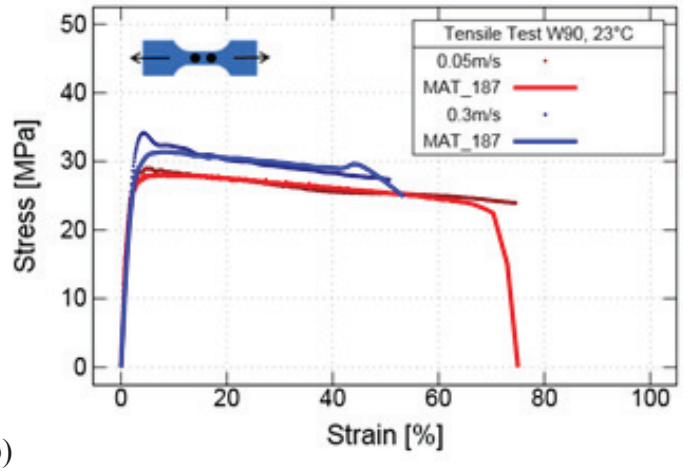


(b)

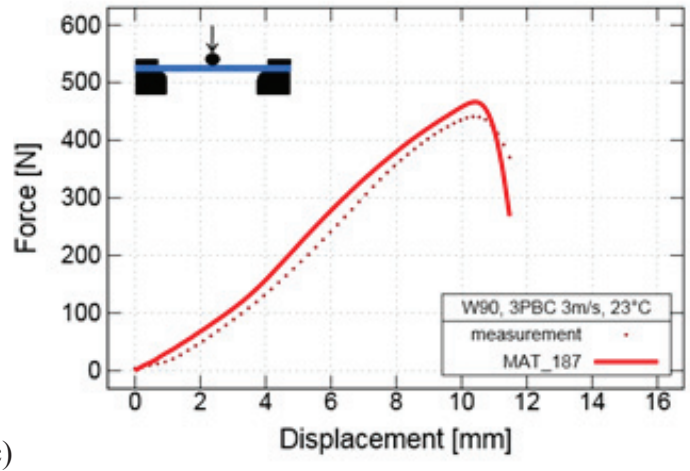


(c)

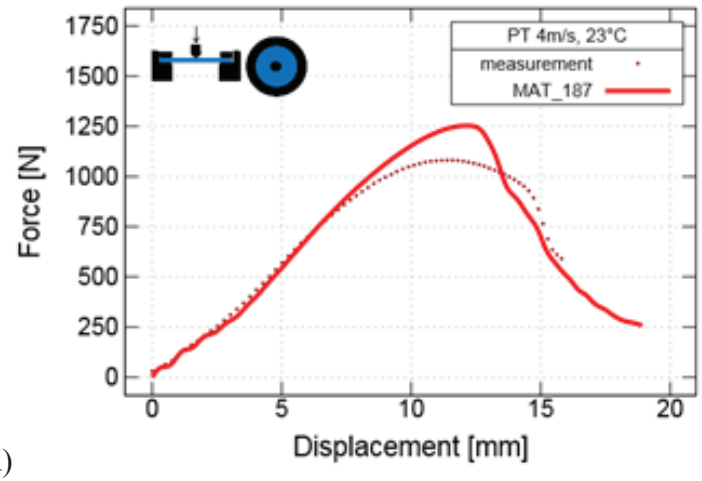


(d)

Figure 12. Comparison of test and simulation results for (a); tensile tests (b); dynamic bending tensile test and (c) dynamic puncture test (Source: P. Reithofer et al.2018).

In the study, the fittings of the simulation and experiment curves were consistent and material models were able to simulate the beginning of failure and GISSMO model showed potential predicting the damage and failure (Reithofer et al. 2018).

M. Kucewicz et al. characterized the process of deformation of a FDM built ABS structure under static loadings. MAT_24 material model from the material library of LS-Dyna was considered for the numerical models, and in order to access model parameters, material properties were determined and stress- plastic curves were defined in model.

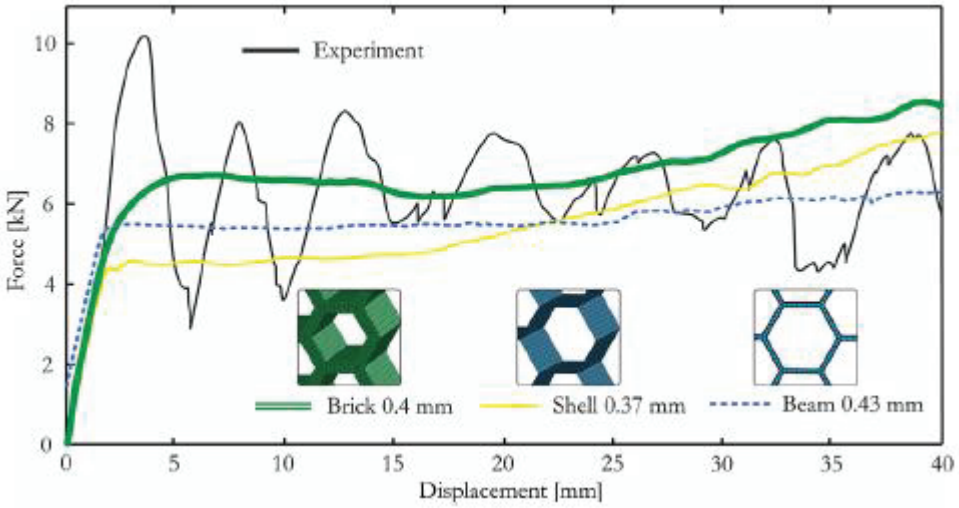


Figure 13. Force vs. displacement curves obtained from the experiments and numerical analyzes for three different element types (Source: Kucewicz et al. 2018).

The comparison of the results of experiments and numerical analyzes (shown in Figure 13) showed good correspondence in terms of deformation, maximum displacement and force. Mesh sensitivity study was also investigated and results showed that the lowest values of force were obtained with finer mesh (Kucewicz et al. 2018) .

Tabacu and Ducu investigated the deformation characteristics and energy absorption of the hybrid structures which contained of and aluminum tube and FDM built ABS multi-cell insert. For characterization, samples were manufactured with stacking configuration of -45°/0°/45°/90°. *MAT_81 which is a material model with damage was used in numerical simulations. Results of the tensile tests of a specimen following ASTM specification were presented and compared with numerical results. They observed that (Figure 14), numerical results correlated with experimental data in terms of failure stress and strain with the use of *MAT_81. And also they reported that by adding the 3D printed ABS structure to the tube, the compressive strength was increased comparing to the structure having aluminum tube only (Tabacu and Ducu 2018).

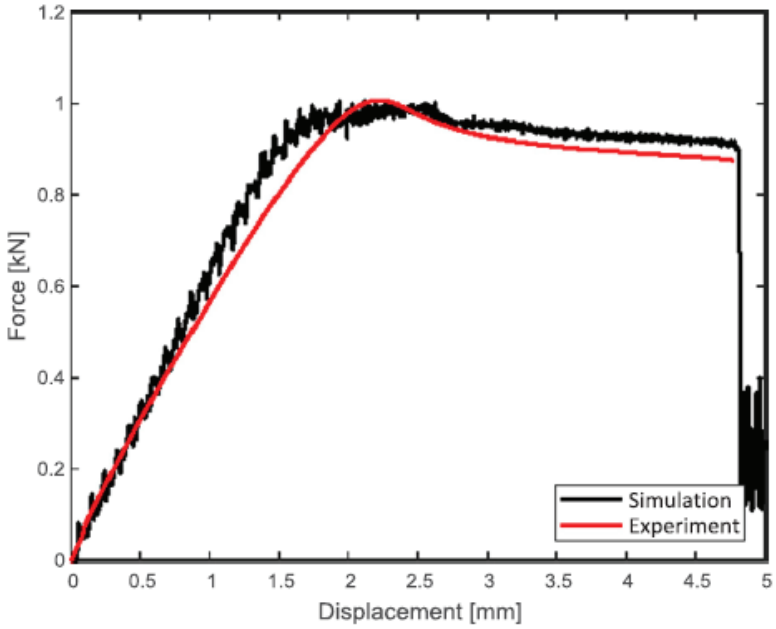


Figure 14. Numerical vs. experimental results of tensile test of ABS with using material model with damage (Source: Tabacu and Ducu 2018).

Tabacu and Ducu investigated the FDM built ABS structures under compressive loads. Stress-strain curves which were determined from tension and compression tests were defined to a *MAT_124 material model. A softening characteristic which was attributed to the damage of the ABS structure was observed in the stress–strain data under tensile load. To predict the erosion of the material, *MAT_ADD_DAMAGE_GISSMO was added to the *MAT_124 material model. To obtain failure strains at different triaxiality values under tensile load, shear 0$^{o}$, shear 45$^{o}$, smooth tension and notched specimens representing different triaxiality values were fabricated. Exact failure strain values of the ABS structures could not be determined through the experiments. For example, in the testing of a shear 0$^{o}$ specimen, the recorded failure strain was obtained as 0.11 although, in the target area, the exact strain had a maximum value of 0.02 (2%). Therefore, the value of failure strain for the triaxiality of 0, was changed from 0.11 to 0.2. Figure 15 presents the values introduced in the model and the experimental values of the failure strain vs. triaxiality.

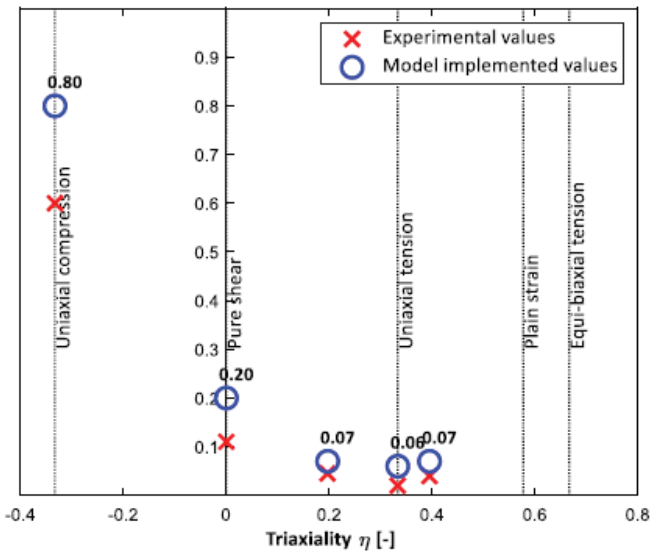


Figure 15. Model implemented and experimental equivalent plastic strain values (Source: S. Tabacu and C. Ducu. 2020).

Then, experimental and numerical results of the samples at each triaxiality value were compared. As it can be seen in Figure 16, peak force values was well correlated between the numerical and experimental data. They came to a conclusion that because there is a delamination in printed specimens, force decreased smoothly after reaching peak force.

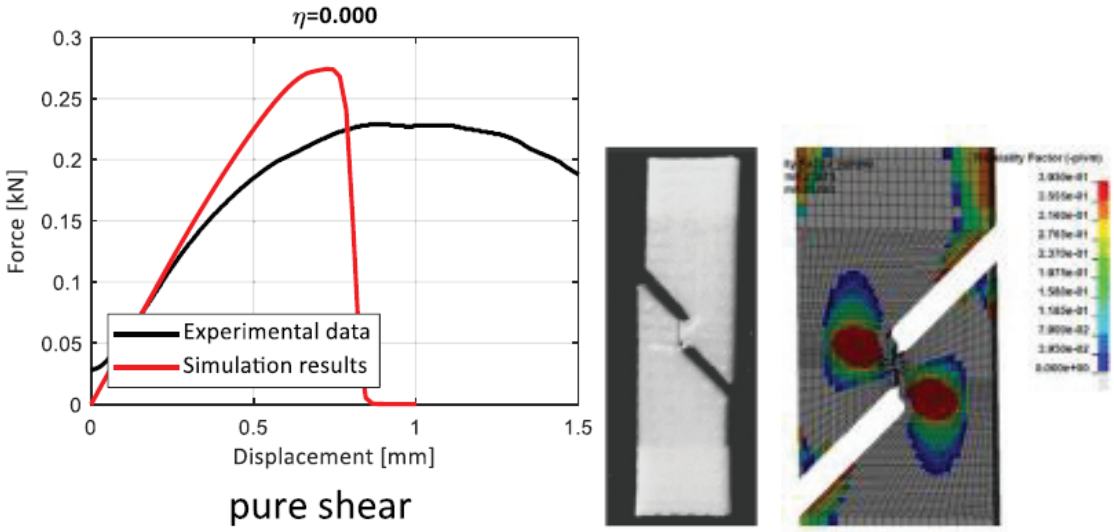

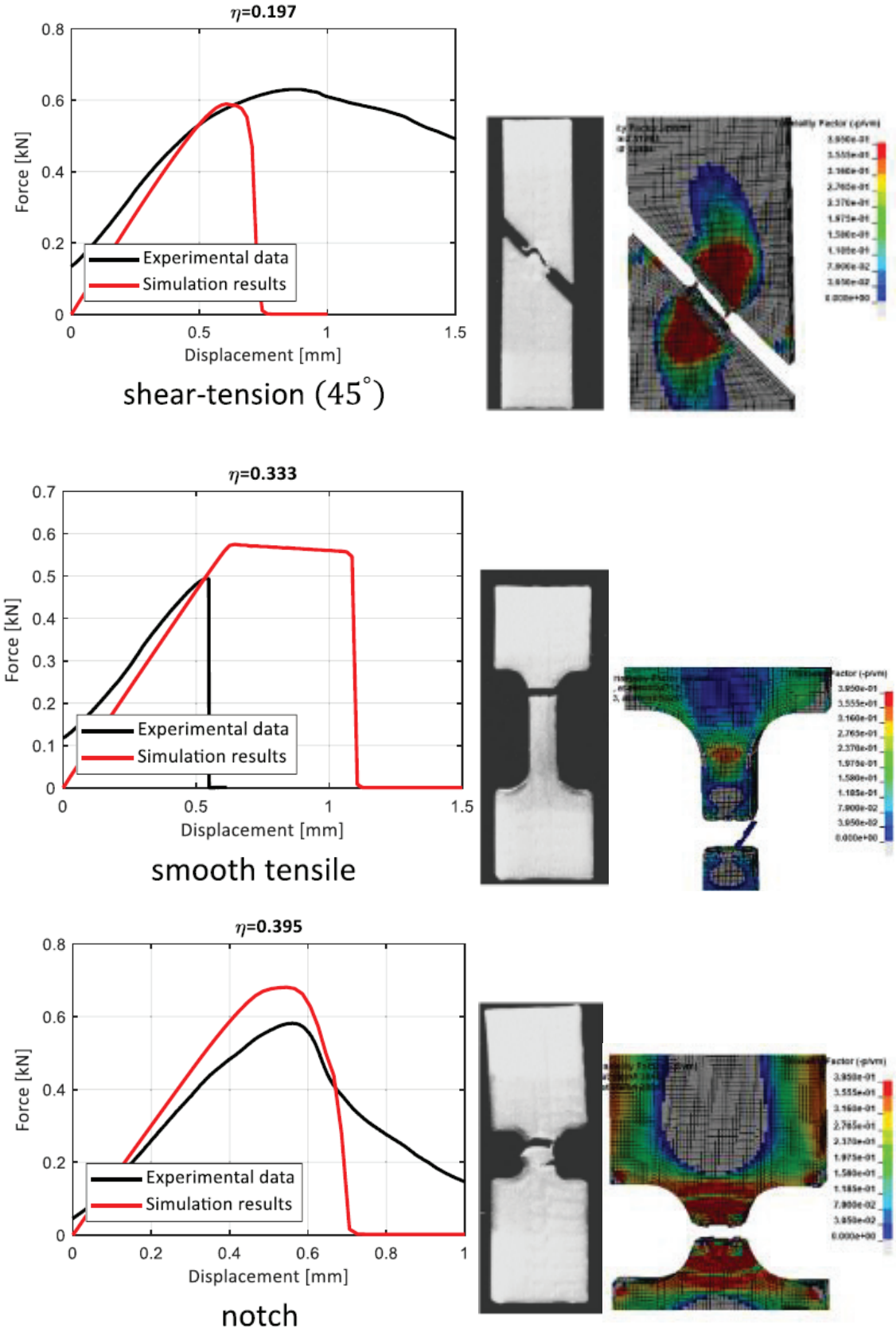


Figure 16. Force–displacement curves of experimental and numerical results (Source: S. Tabacu and C. Ducu. 2020).

Subsequently, the comparison of the results between the experiments and numerical models for the lattice, honeycomb and rectangular structures was found to be in good agreement in terms of the value of peak load. The inconsistency between the experimental and the numerical model results were found to be reasonable because there were uncertainties in the physical model (Tabacu and Ducu 2020).

In the previous study, the exact failure strain could not be recorded by experiments so the minimum value was evaluated then defined in the model. Optimization may be a beneficial method to obtain exact parameter values for the simulations. D. Hörling et al. studied GISSMO damage model on a high strength steel grade DOCOL 1200M. Failure strain, $\varepsilon_f$, equivalent plastic strain, $\varepsilon_{v,loc}$, damage exponent , n, fading exponent, m, parameters and curves defining the time necking and failure occurs at was found. In order to find the parameters, shear 0°, shear 45°, shear 60°, notched, double notched and mini tensile test specimens (seen in Figure 17) were produced and tested in uniaxial tension with 5 mm/min test speed.

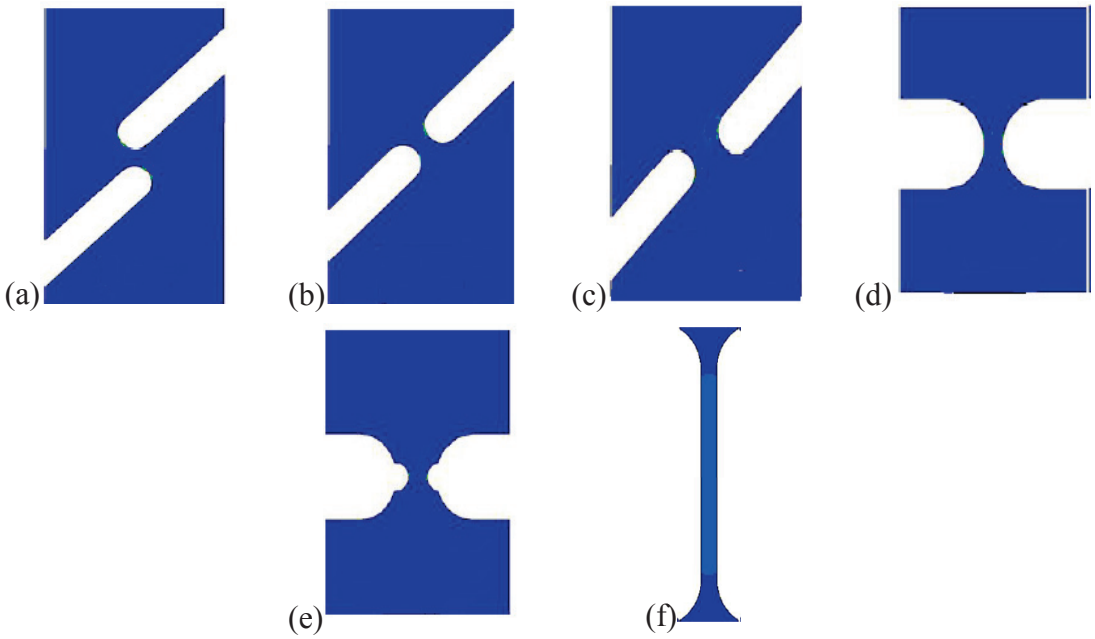


Figure 17 Produced (a) shear 0°, (b) shear 45°, (c) shear 60°, (d) notched, (e) double notched and (f) mini tensile test specimens (Source: D. Hörling et al.).

Then a LS-OPT model was created with feedforward neural-networks and space filling point selection for each case separately.

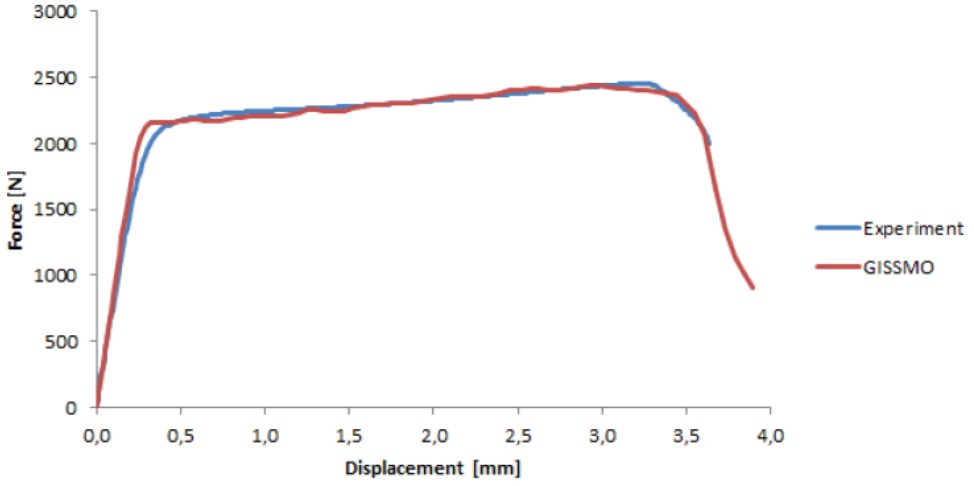
3000
2500
2000
1500
1000
500
0
Force [N]
0,0
0,5
1,0
1,5
2,0
2,5
3,0
3,5
4,0
Displacement [mm]
Experiment
GISSMO

(a)

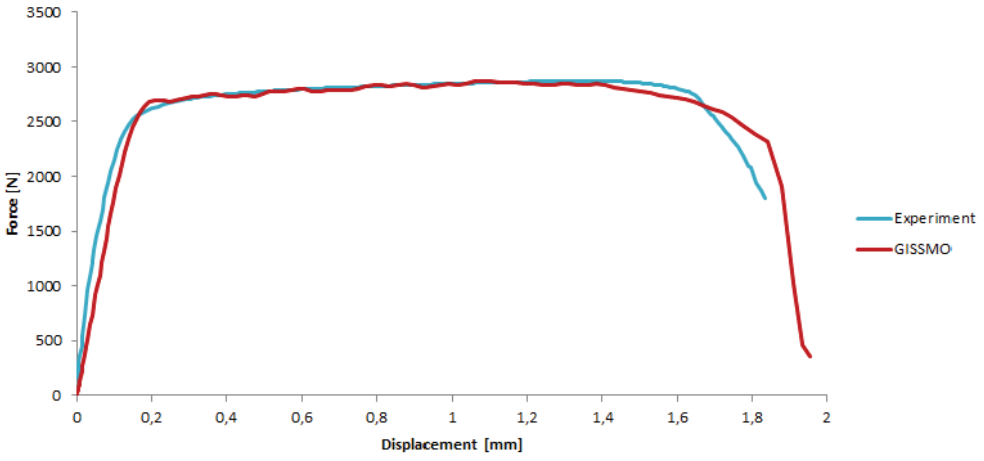
3500
3000
2500
2000
1500
1000
500
0
Force [N]
0
0,2
0,4
0,6
0,8
1
1,2
1,4
1,6
1,8
2
Displacement [mm]
Experiment
GISSMO

(b)

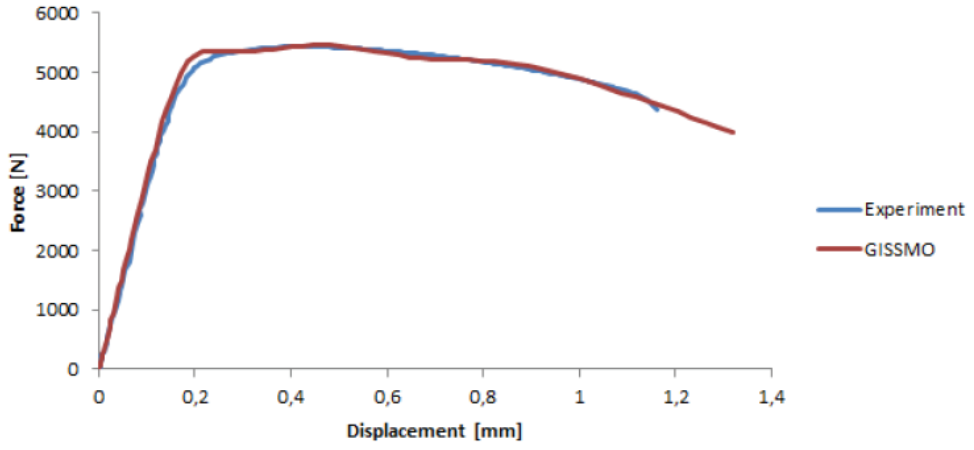
6000
5000
4000
3000
2000
1000
0
Force [N]
0
0,2
0,4
0,6
0,8
1
1,2
1,4
Displacement [mm]
Experiment
GISSMO

(c)

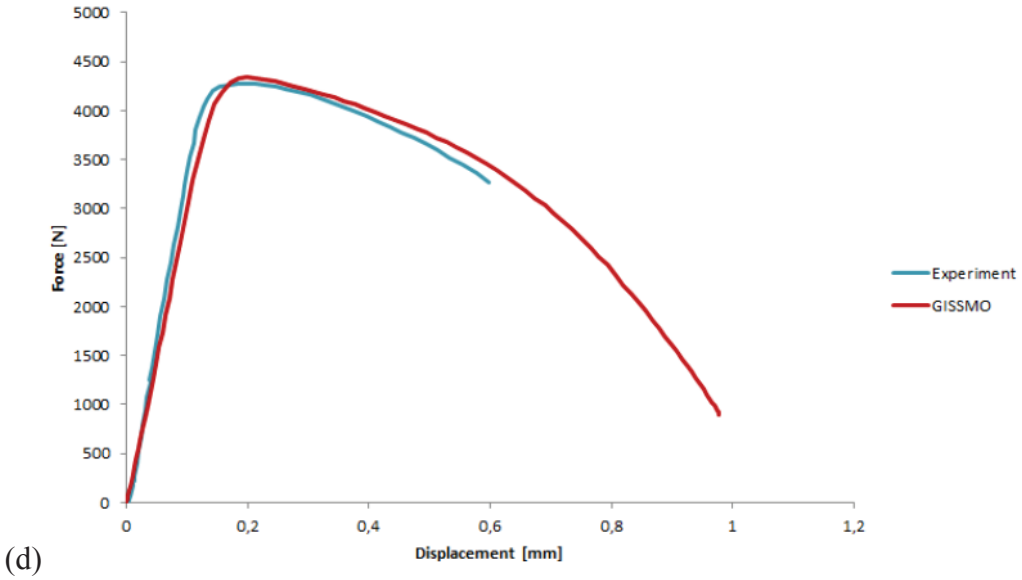


(d)

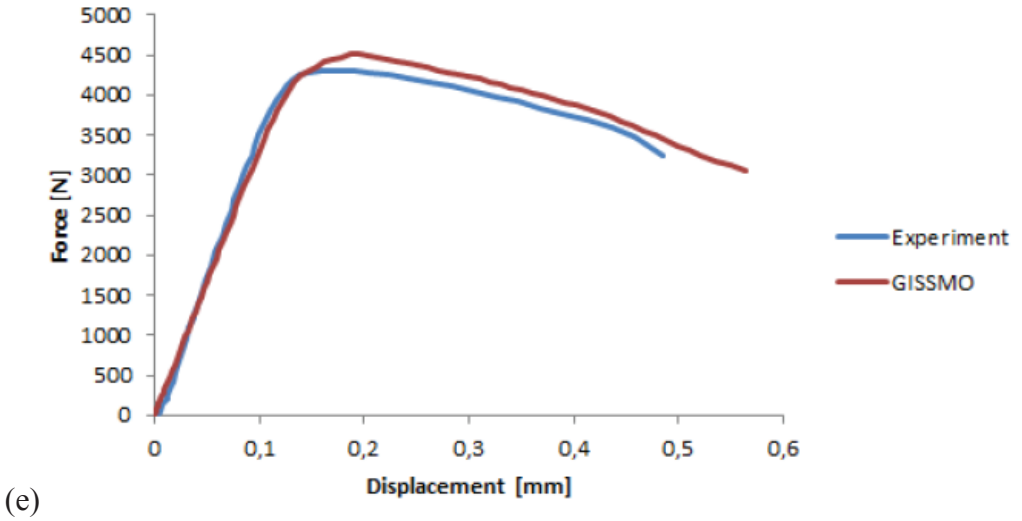


(e)

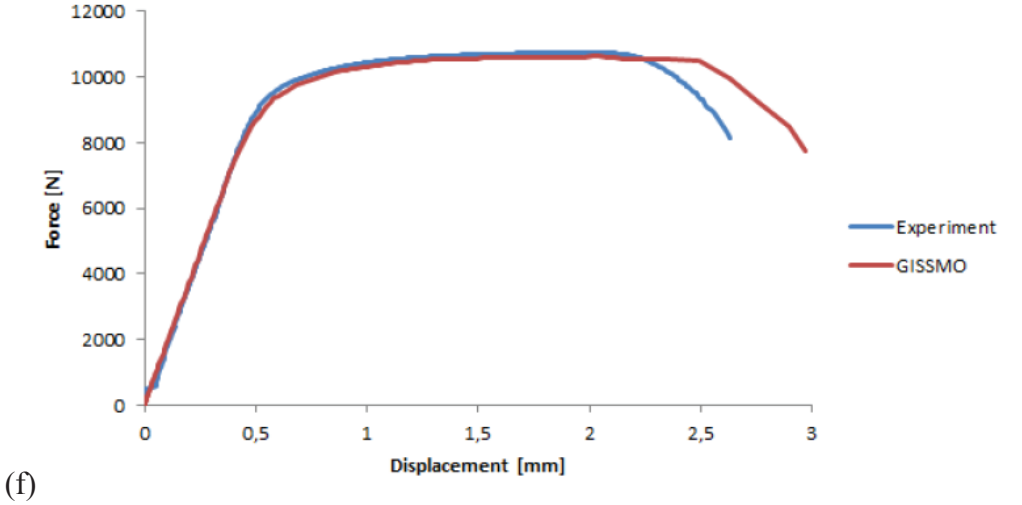


(f)

Figure 18. Force displacement curves for the (a) shear 0° (b) shear 45° (c) shear 60° (d) notched (e) double notched (f) mini tensile specimens both experimental data and the GISSMO simulation (Source: D. Hörling et al.).

The fitting curves of the numerical and experimental results (Figure 18) were presented. They observed that when the specimens were optimized individually, simulation and experimental results matched quite well in terms of peak force and failure strain. The mean value of the achieved parameters was used as initial values for the last optimization. Obtained experimental and numerical results of the optimization which was done for five specimen types at the same time are illustrated in Figure 19.

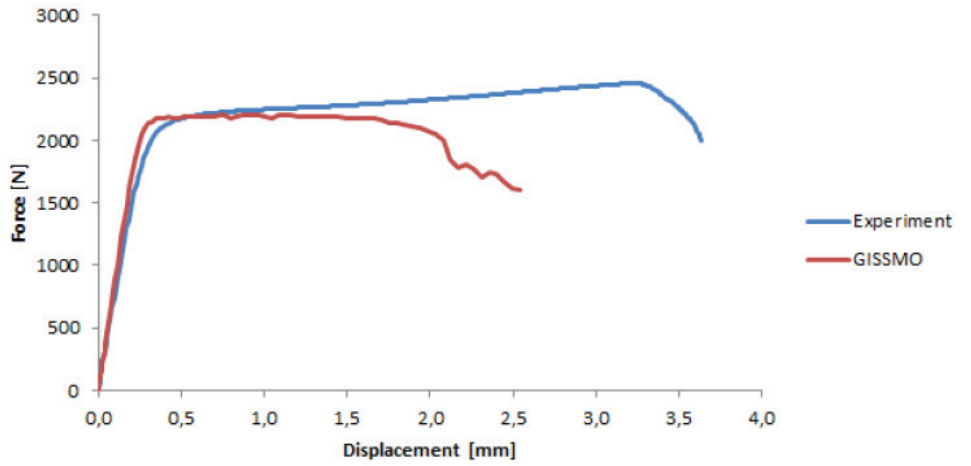


(a)

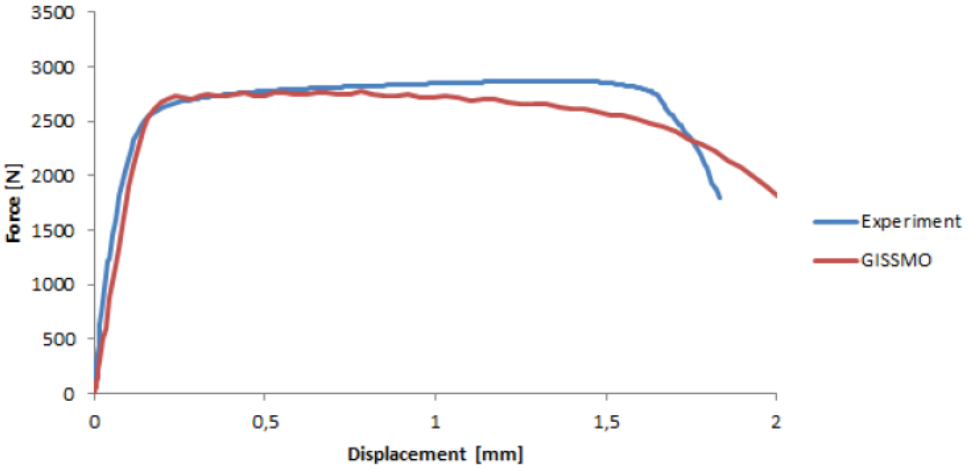


(b)

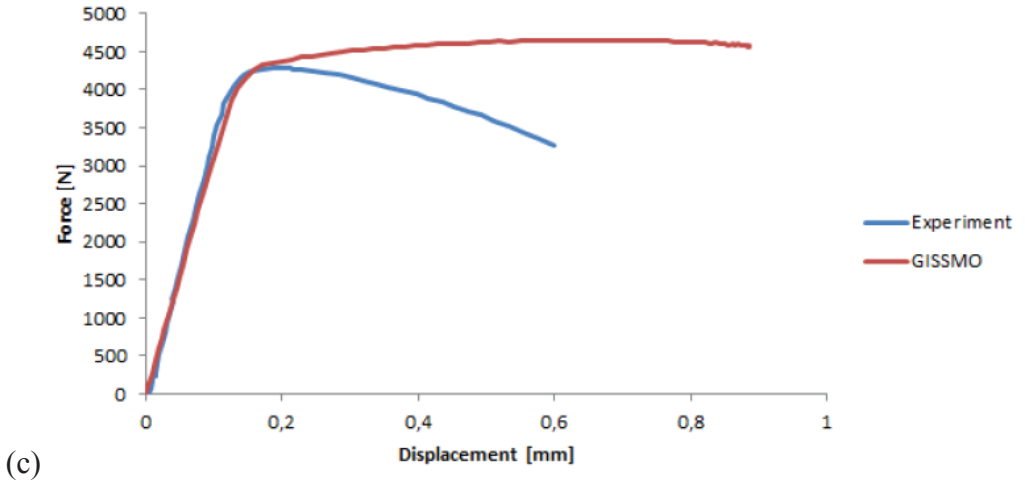


(c)

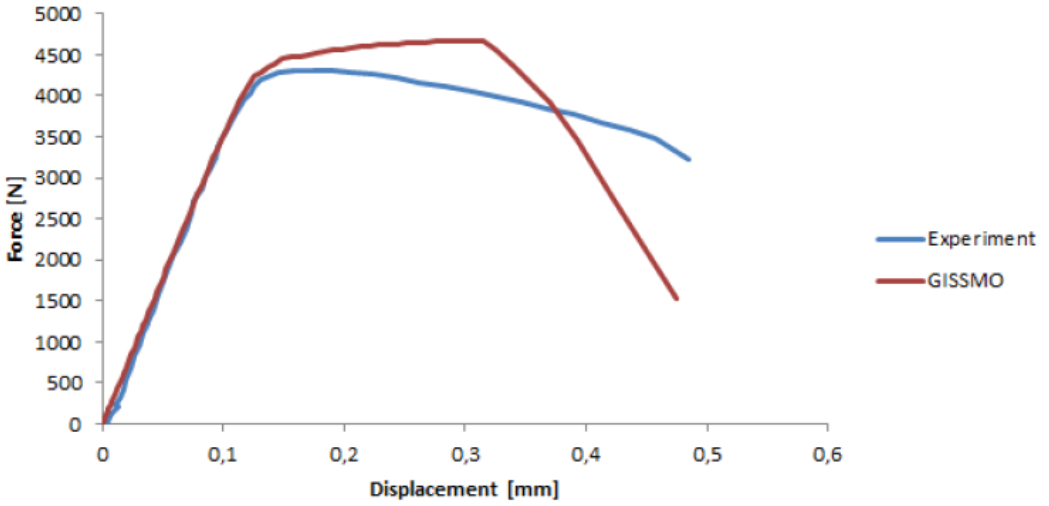


(d)

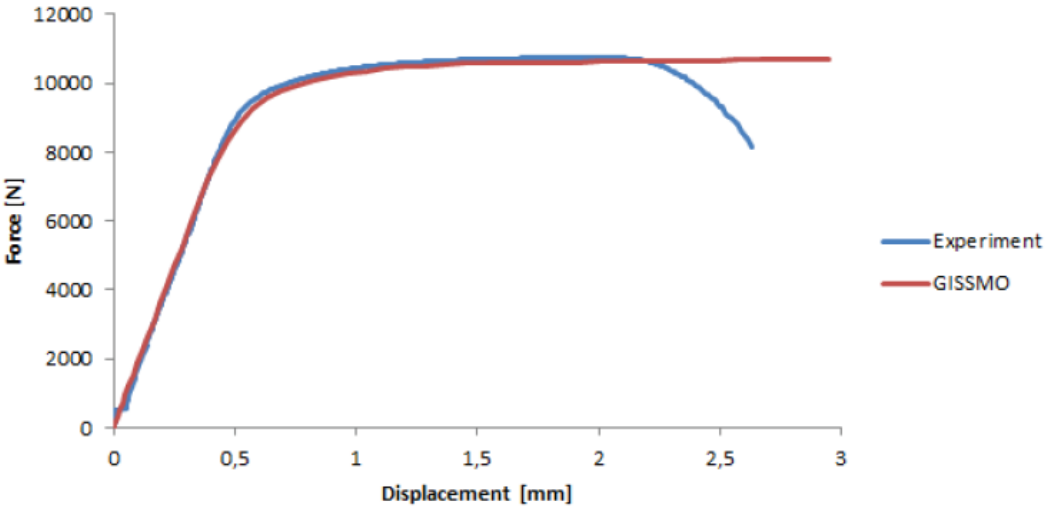


(e)

Figure 19. Force displacement curves for the (a) shear 0° (b) shear 45° (c) notched (d) double notched (e) mini tensile specimens both experimental data and the GISSMO simulation (Source: D. Hörling et al.).

They reported that the matched curves in the combined optimization simulations behaved more ductile than the experiments. Because the necking and localization of deformation was clearly seen in individual optimizations, they showed better match between simulations and experiments than the multi case optimization. The result showed that GISSMO damage model has the potential to predict the failure behavior well. Author suggested that to make the GISSMO model work for a wider range of stress states a pure shear test, such as a butterfly specimen, could be used and also compressive tests could be involved to cover the negative triaxialities(Hörling 2015).

## 1.3. Aim and Scope of the Study

Past researches who have focused on static and dynamic characteristics of FDM built ABS concluded that, even though the material used in FDM is isotropic, due to the nature of the manufacturing route the obtained product is not unfortunately isotropic, instead anisotropic. There is a need of the representation of constitutive behaviour of the FDM built ABS plastics in the literature.

This thesis aims to identify the suitable material models which fulfil the need of representation of static and dynamic constitutive behavior of FDM built ABS that have already been implemented in LS-Dyna. For this purpose, promising alternative material models from the material library of LS-Dyna were identified. Raw data obtained from experiments at quasi-static and high strain rates, were reduced and defined in material models. Following these, an advanced damage model was selected to characterize the failure behavior of the FDM built ABS. In this damage model, *MAT_ADD_DAMAGE_GISSMO, the effect of stress triaxiality on the damage accumulation is descripted (Hallquist 2006). GISSMO includes parameters which identify the damage criteria and in order to determine these parameters, LS-OPT optimisation tool that successfully works with LS-Dyna was used.

A brief introduction about manufacturing method Fused Deposition Modelling, its history and mechanical properties of ABS polymer were presented as an introduction. A literature review which covers characterizations of FDM built ABS and investigations of the effect of additive manufacturing on the mechanical behaviors of ABS polymer, and numerical studies about selection of proper material models for different materials are presented in the first chapter.

The second chapter started with the explanation of manufacturing and preparation

of test specimens. Following this, quasi-static and high strain rate testing methodologies are explained respectively. Subsequently the material model explanation and the preparation of the numerical models were presented. In the fourth chapter, quasi-static and high strain rate experimental test results and the numerical results are presented. Conclusions and findings are given in the fifth chapter.

# CHAPTER 2

# PRODUCTION OF THE SPECIMENS AND EXPERIMENTAL METHOD

## 2.1. Introduction

In this chapter, manufacturing method of the FDM built ABS parts and conducted experimental studies are described in detail. The tests were performed at quasi-static and high strain rates to characterize the mechanical properties of the FDM built ABS parts. First, manufacturing process and geometric properties of the test specimens are explained. Then, quasi-static testing standards and procedures are described with stress-strain data acquisition. Lastly, high strain rate testing methodology is explained.

## 2.2. Manufacturing of Specimens by FDM

Testing specimens were manufactured by using FDM machine (Stratasys uPrint SE Plus) and ABS thermoplastic filament used in the printer. The raster angle is [+45/-45] and the specimens were built in vertical direction to the platform. Some work (Dawoud, Taha, and Ebeid 2016) indicated that the maximum tensile and impact strength was observed on the specimens having [+45/-45] raster angle. The maximum build area of the printer was 203 x 203 x 152 mm (8 x 8 x 6 inch). Parameters of the production process are given in Table 2.

Table 2 Production process parameters.

| Parameter | Value |
|---|---|
| Extruder temperature | 300$^{o}$ C |
| Layer thickness | 0.254 mm |
| Infill | 100% |
| Raster angle | +45/-45$^{o}$ |
| Air gap | Default |

For determining material model parameters of the thermoplastic material, tensile and compression samples were prepared. ASTM D638-03 standard (International 2015) was used as a dimension reference for the printed dog-bone specimens. Specimens were subjected to quasi-static tensile testing. Geometric shape with dimensions and produced specimen are shown in Figure 20. Specimens were built in flat orientation with high infill density.

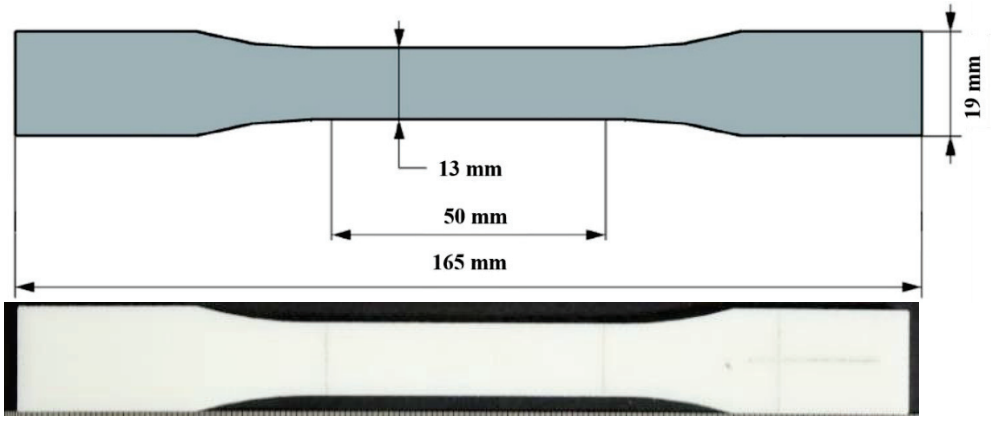


Figure 20 The dog-bone ABS specimen that is printed using FDM method according to ASTM D638-03 for quasi-static tensile testing.

Custom tensile specimen was manufactured for high strain tensile tests. To observe mechanical behavior of the material under quasi-static loading condition, specimens were subjected to quasi-static tensile tests, also. Specimens having 5 mm in gage length were used, since shorter gage length is more desirable for SHTB tests. Object is to break the specimen by one mechanical wave. These specimens were also built in flat orientation with high infill density. Geometric shape with dimensions and produced specimen are shown in Figure 21.

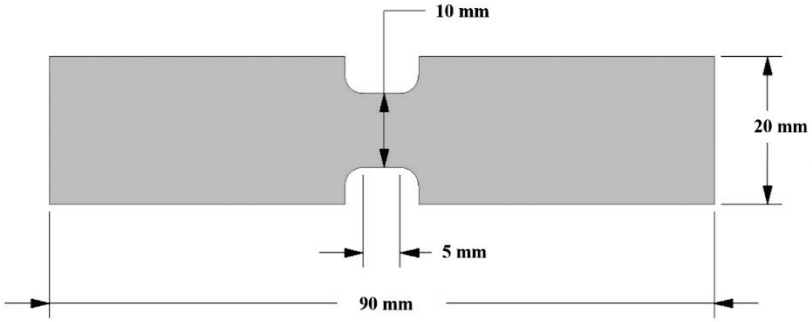

Figure 21 Custom ABS specimen that is printed using FDM method for dynamic tensile testing.

Then, for compression tests at quasi-static and high strain rates, cylindrical compression specimens were manufactured. Specimens were printed in vertical direction, having 8 mm in diameter and 8 mm in length. Geometric shape with dimensions and produced compression specimens are shown in Figure 22.

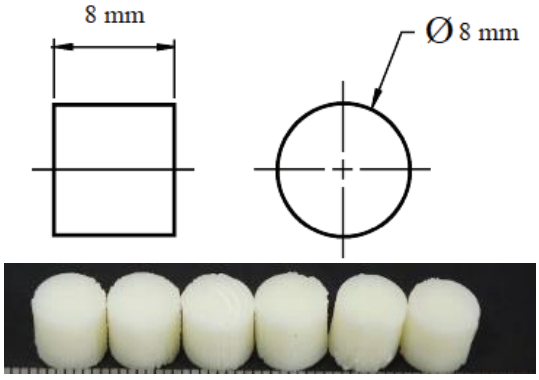


Figure 22 Cylindrical ABS specimen that is printed using FDM for quasi-static and dynamic compression testing.

In order to acquire accurate results from GISSMO analyzes, range of experimentally achieved triaxialities should be as wide as possible. Since the adopted test method is uniaxial tension, desired triaxiality range is between 0 and 2/3. $\eta = 0$ indicates pure shear, $\eta = 0{,}33$ indicates uniaxial tension and $\eta = 0{,}67$ indicates biaxial tension. To cover a big part of the triaxiality range of $0 \leq \eta \leq 0.6$ ; shear, notch and mini tensile test specimens were manufactured. Geometric shape and the size of the specimens (Figure 23) were chosen according to Effelsberg et al.

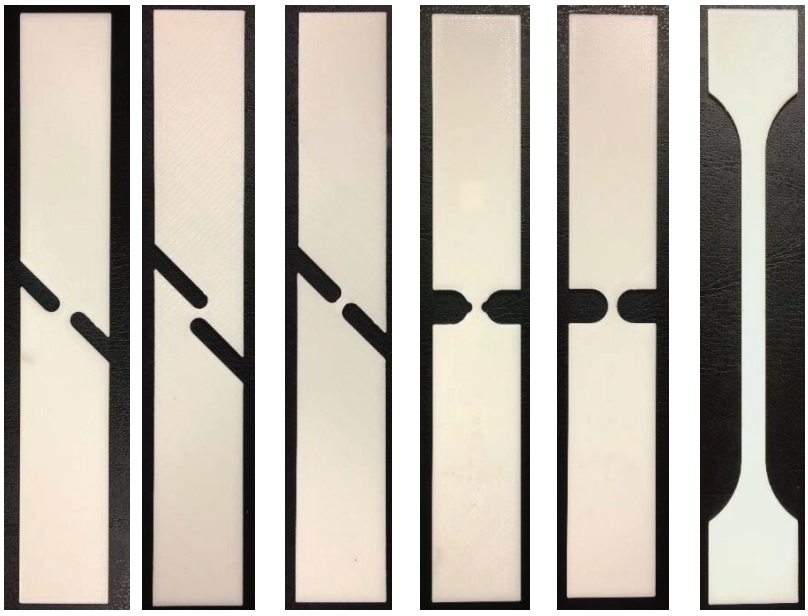

Figure 23 a) Shear60$^{o}$, b) shear45$^{o}$, c) shear 0$^{o}$, d) double notched, e) notched, f) mini tensile ABS specimens that were printed using FDM method for GISSMO analyzes

Finally for gas gun test, sample plates were manufactured in 150 mm length, 200 mm width and 5mm thickness in flat building orientation.

## 2.3. Experimental Method

Quasi-static and high strain rate tests were conducted on the FDM built ABS, and these tests are explained in the following sections in detail. Quasi-static tests were conducted with Shimadzu AG-X universal test machine and high strain rate tests were conducted with split Hopkinson pressure bar, split Hopkinson tension bar and gas gun apparatus in the Dynamic Test and Modelling Laboratory.

### 2.3.1. Quasi-static Testing

In the current study, by using Shimadzu AG-X universal testing machine, tests can be conducted between strain rates of $10^{-4}$ to $10^{-1}$ $s^{-1}$. In order to determine the strain rate sensitivity in the low strain rate range and to measure quasi-static compressive and tensile strength of FDM built ABS different strain rates were chose.

The particular quasi-static testing device (shown in Figure 24) is equipped with a load cell having a capacity of 300 kN. Testing machine may be used with constant cross-

head speeds up to 8 mm/sec. In quasi-static tensile test, specimen is attached between upper and bottom heads and similarly in quasi-static compression test, specimen in placed between upper and bottom plates. In both of the tests, upper part of the machine moves with a controlled constant velocity. A video extensometer is also coupled with the device.

The displacement of gage markers which were located on the specimens, were tracked by two video extensometers to read the displacement so that the stress–strain values could be obtained. The true stress–strain values of the tensile and compression tests were obtained by following equations (2.1)-(2.4), respectively.

$$\varepsilon_e = \frac{\delta}{L_0} \tag{2.1}$$

$$\varepsilon_t = \ln(L/L_0) \tag{2.2}$$

$$\sigma_e = \frac{F}{A_0} \tag{2.3}$$

$$\sigma_t = \frac{F}{A} \tag{2.4}$$

Where F is the load, $L_0$ is the initial gage length, Δl is the instantaneous value of the length, A is the cross-sectional area of specimen at which the load is applied, $A_0$ is the cross-sectional area of specimen before deformation has taken place and δ is the total elongation (the subscript t denotes the true values and e denotes the engineering values).

(a)

(b) 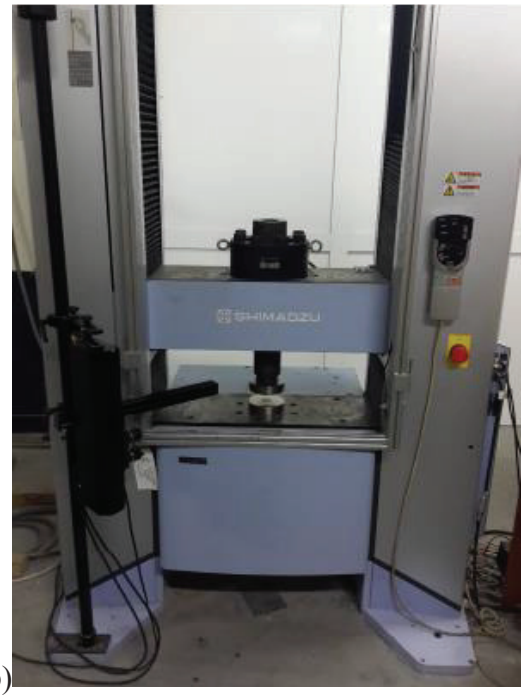


Figure 24 Quasi-static a) tension b) compression test set-up

## 2.3.2. Dynamic Testing

High strain rate tests were conducted with Split Hopkinson Pressure Bar (SHPB) and Split Hopkinson Tension Bar (SHTB) shown in Figure 25 in order to obtain strain rate dependent behaviors of the FDM built ABS plastic under dynamic loadings.

(a)

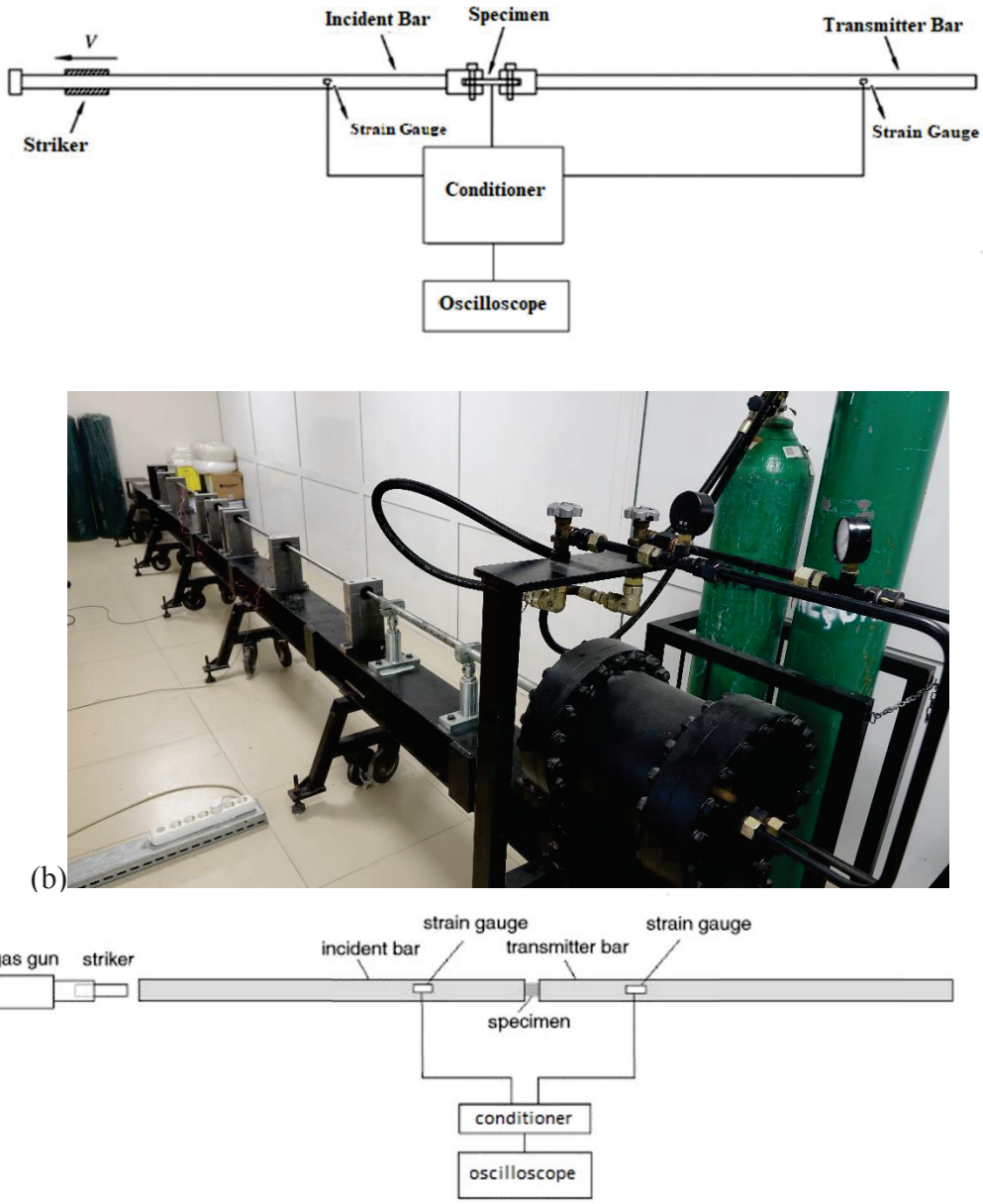


Figure 25 Split Hopkinson (a) tension (b) compression bar setup

In the design of the SHTB and SHPB, specimen is placed between incident and transmitter bars. A stress wave is created by a striker bar, which propagates through incident bar toward specimen and it is measured as an incident pulse with the strain gages placed on incident bar. When specimen undergoes plastic deformation, some part of the stress wave reflects back to the incident bar and other part passes through the transmitter bar. Strain gages placed on the incident bar and transmitter bar capture the reflected and transmitted waves. Then the measured waves were transferred into a signal conditioner. Then the voltage wave versus time curve is displayed on the screen of an oscilloscope. As an example, a voltage-time history graph obtained from a Split-Hopkinson pressure

bar test is illustrated in Figure 26.

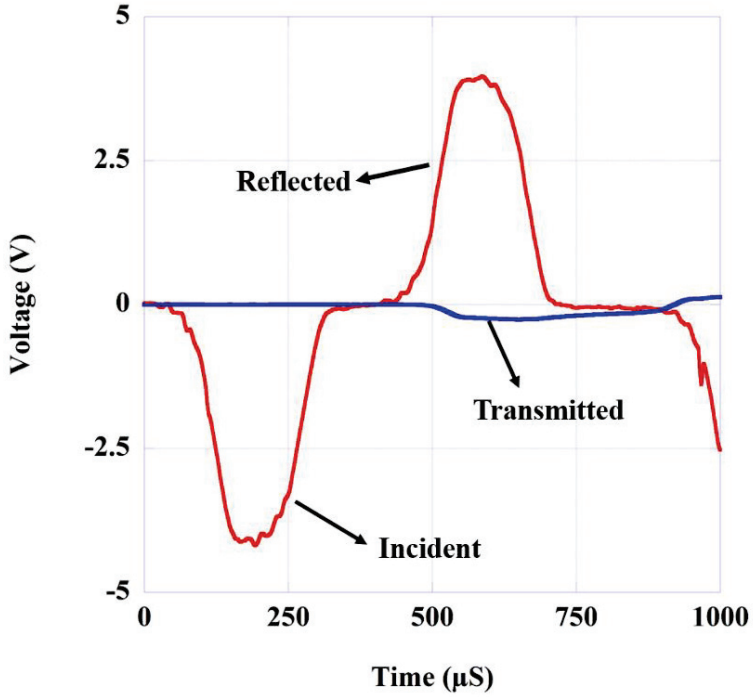


Figure 26 An example to a voltage versus time curve obtained from SHPB testing of FDM built ABS.

The determination of the stress ($\sigma_b$), strain ($\varepsilon_b$) that occurs in the incident and transmitter bars, and the duration of the incident pulse (T) after the striker bar hits the incident bar was obtained by following equations (2.5)-(2.7), respectively.

$$\sigma = \frac{c_b \rho_v v_o}{2} \tag{2.5}$$

$$\varepsilon = \frac{\sigma_b}{E_b} \tag{2.6}$$

$$T = \frac{2L_{striker}}{c_b} \tag{2.7}$$

where $\sigma$ is the stress pulse, $c_b$ is the wave velocity, $v_o$ indicates impact velocity of the striker bar, $\rho_b$ indicates density of the bar, $L_{striker}$ is the length of the striker and $E_b$

is the Young's modulus of the bar.

To obtain dynamic response of the specimens, the voltage values obtained from the oscilloscope needs to be converted into strain value ($\varepsilon(t)$) first by using following equation;

$$\varepsilon(t) = \frac{2V(t)}{V_{exc} \cdot GF \cdot K_{gain} \cdot (1 + v)} \tag{2.8}$$

where; $V_{exc}$ is the excitation voltage which is set to 10V , $K_{gain}$ indicates the value which is set to 200 for incident and 800 for transmitted waves, GF is the gage factor of the strain gage, and $v$ stands for the Poisson's ratio of the bar material.

Then, stress, strain and strain rate of the specimens can be determined by using following equations

$$\sigma_s(t) = \frac{A_b E_b \varepsilon_t(t)}{A_s} \tag{2.9}$$

$$\varepsilon_s(t) = -\frac{2C_b}{L_s} \int_0^t \varepsilon_{ref}(t)\, dt \tag{2.10}$$

$$\dot{\varepsilon}_s(t) = -\frac{2C_b}{L_s}\, \varepsilon_{ref}(t) \tag{2.11}$$

where; $E_b$ is modulus of elasticity of the bars and $C_b$ indicates the wave velocity of the bars. $A_b$ and $A_s$ refer to the cross-sectional areas of bars and specimens, respectively. $\varepsilon_t$ and $\varepsilon_{ref}$ are the transmitted and reflected strain values, $L_s$ is the initial length of the specimen.

Gas-gun tests were also studied for the FDM built ABS plastics. Experimental setup (Figure 27) is designed of specimen holder (Figure 28) and laser barriers, used to measure the impact and exit velocity of the projectile after penetrating ABS plates, in a closed room covered with iron sheets.

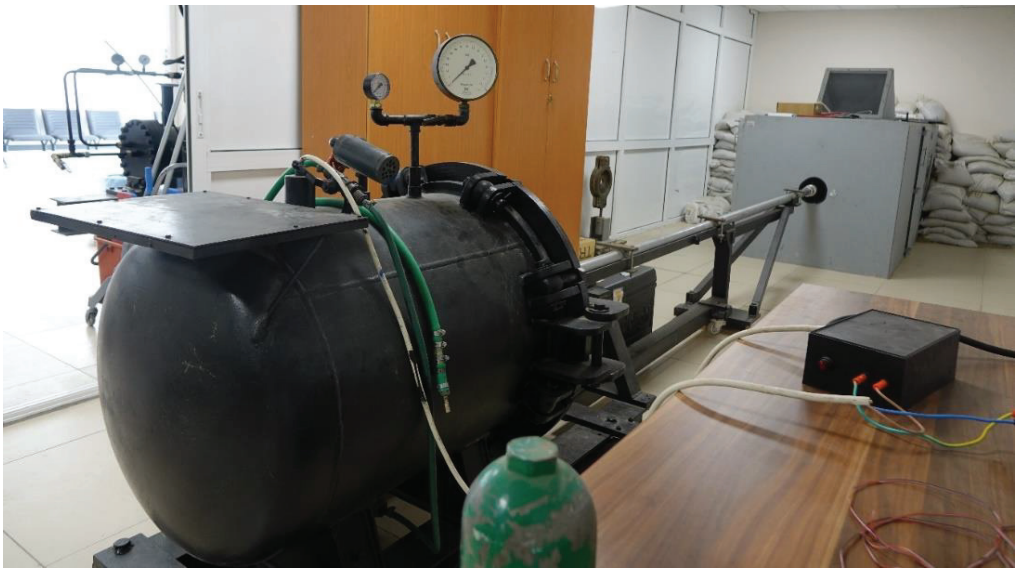

Figure 27 Gas gun test set-up.

Trigger mechanism accelerates the projectile and polyurethane sabot helps the projectile to move centrally in a gun barrel. Projectile having 110 g in weight and 30 mm in diameter was used for the tests.

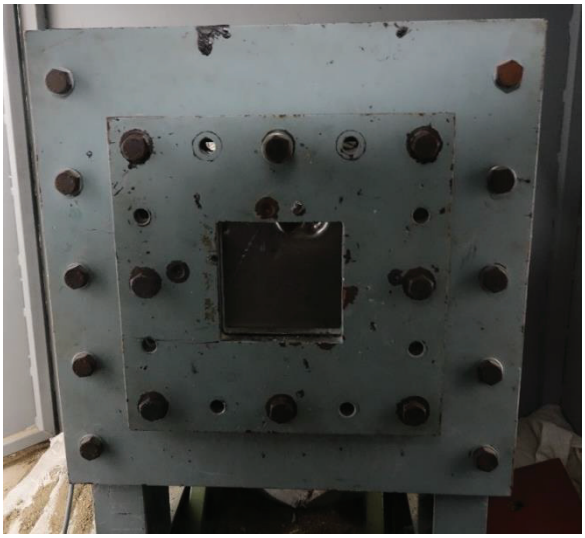

Figure 28 Specimen holder.

# CHAPTER 3

# NUMERICAL MODELING

Finite element simulations of the quasi-static and high strain rate tests were performed in a finite element software, LS-DYNA which is capable of simulating events that are occurring in a short time with large structural deformations. It has become an important product development tool in many industries, especially in automotive, aerospace and defense due to its comprehensive material models, complex contact condition identification features and solution algorithms.

Explicit solutions are suitable when there is acceleration (dynamic) whereas an implicit approach can solve the dynamic and the static problems. All transient solutions, whether implicit or explicit, solve the fundamental equation of motion (Erhart 2016) given in Equation 3.1.

$$ma^n + cv^n + kd^n = f^n \tag{3.1}$$

where $n$ denotes time step, $m$ is the mass and $c$ is the damping coefficient matrices, $kd^n$ is the internal force and $f^n$ is the external force in the structure. $a, v, d$ are acceleration, velocity and displacement vectors respectively. Generally main problem is to determining the displacement at some future time in other words, to determine $d^{n+1}$ at time $t^{n+1}$. Explicit analysis solves directly by using central difference method as:

$$d^{n+1} = f(d^n, v^n, a^n, d^{n-1}, v^{n-1}, \dots) \tag{3.2}$$

Implicit analysis solves using forward difference method given in Equation 3.3 and the solution depends on the velocities and accelerations of the nodes at state $n + 1$

$$d^{n+1} = f(v^{n+1}, a^{n+1}, d^n, v^n, \dots) \tag{3.3}$$

Given these unknowns, an iterative solution at each time step is required.

There are almost 300 different material model in the material library of LS-DYNA

for all kind of material classes. Especially for the polymers, three *MAT_024 *MAT_081 and *MAT_187 material models are commonly used.

*MAT_024 material model has a cylindric von Mises yield surface (Hallquist 2006) in other words, in numerical models, *MAT_24 checks if the yield function is satisfied or not. Equation for the definition of the yield function is given in Equation 3.4.

$$\Phi(\sigma) = \sigma_{eq} - \sigma_y(\varepsilon^p) = 0 \tag{3.4}$$

Where $\sigma_{eq}$ is the equivalent stress, and $\sigma_y$ is the yield stress which can be a function of the plastic strain,$\varepsilon^p$ which is accumulated throughout the deformation process. In Figure 29 yield function is plotted in principal stress coordinates.

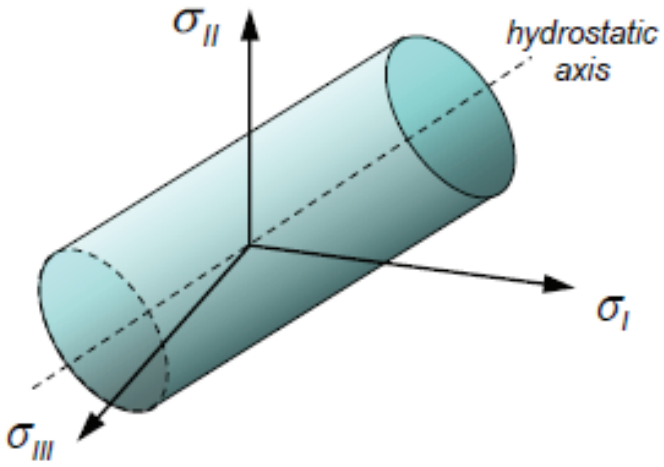


Figure 29 The von Mises yield surfaces in principal stress coordinates (Source:(Bertarelli 2016).

*MAT_24 material model includes strain rate effects. By defining a table curve in the model, seen in Figure 30, strain rate effects were taken into consideration. Corresponding yield stress-effective plastic strain curves for each strain rate were defined in this model.

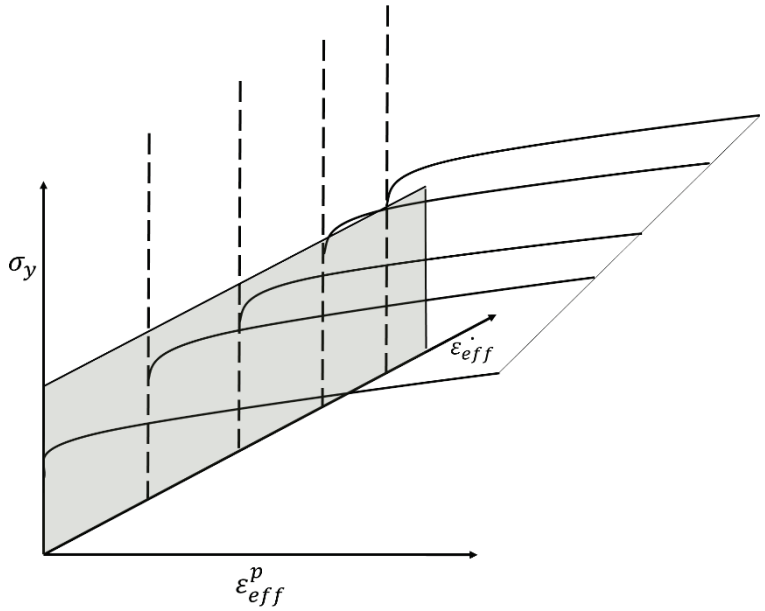


Figure 30 Table of curves defined to considerate strain rate effects.

The LS-PREPOST material keyword of the *MAT_24 material is seen Figure 31. sigy represents the yield stress, lcss is where the table of curves defined. ro is the mass density, vp is the formulation for rate effects, fail gives the equivalent plastic strain at failure.

```
*MAT_PIECEWISE_LINEAR_PLASTICITY
$#     mid        ro         e        pr      sigy      etan      fail      tdel
         1       0.0       0.0       0.0       0.0  0.01.00000E21       0.0
$#       c         p      lcss      lcsr        vp
       0.0       0.0         0         0       0.0
$#    eps1      eps2      eps3      eps4      eps5      eps6      eps7      eps8
       0.0       0.0       0.0       0.0       0.0       0.0       0.0       0.0
$#     es1       es2       es3       es4       es5       es6       es7       es8
       0.0       0.0       0.0       0.0       0.0       0.0       0.0       0.0
```

Figure 31 LS-PREPOST material keyword of the *MAT_24 material used in the simulations.

In *MAT_187 material model as it is presented in Figure 32, by defining stress vs. strain curves obtained from the tension, compression and shear tests, the yield surface is expressed with using a von Mises cylinder, Drucker-Prager cone. In Drucker-Prager criterion, yield surface is a function of the pressure and the second invariant of the deviatoric part of the Cauchy stress, $J_2$ and (Alejano and Bobet 2012) can be expressed as

$$\sqrt{J_2} = \lambda I_1 + \kappa$$

where λ and κ are material constants and $I_1$ is the first invariant of the Cauchy stress.

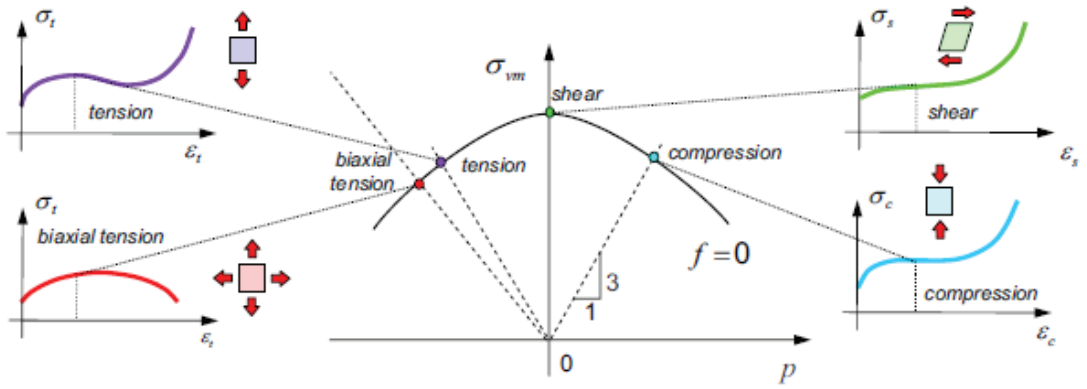


Figure 32 Von Mises stress as a function of pressure

MAT_187 material model is capable of including a plastic Poisson's ratio of ≤0.5. As it is seen in the LS-PREPOST material keyword of the *MAT_187 material in Figure 33, additionally bulk modulus, bulk, and shear modulus, gmod, were introduced in the model. A table of curves for the tension test, lcid-t and compression test, lcid-c, were implemented also.

```
*MAT_SAMP-1
$#     mid        ro      bulk      gmod      emod       nue     rbcfac    numint
         1       0.0       0.0       0.0       0.0       0.0       0.0         0
$#  lcid-t    lcid-c    lcid-s    lcid-b     nuep    lcid-p                incdam
         0         0         0         0       0.0         0         0         0
$#  lcid_d    epfail    deprpt  lcid_tri  lcid_lc
         0  100000.0       0.0         0         0
$#   miter     mipds              incfail     iconv      asaf
         0         0         0         0         0         0
$#  lcemod      beta      filt
         0       0.0       0.0
```

Figure 33 LS-PREPOST material keyword of the *MAT_187 material used in the simulations.

*MAT_81 (MAT_PLASTICITY_WITH_DAMAGE) material model requires the definition of a damage curve, The nominal stress in a damaged material in axial load (LSTC 2020) is defined as

$$\sigma_{\text{nominal}} = \frac{F}{A'} \tag{3.5}$$

Where F is the load applied to a material and A indicates cross sectional area of the specimen. As stated before, the true stress is defined as

$$\sigma_{\text{true}} = \frac{F}{A - A_{\text{loss}}} \tag{3.6}$$

where $A_{\text{loss}}$ represents the void area. Then the damage parameter can then be calculated as follows

$$\omega = \frac{A_{\text{loss}}}{A} \tag{3.7}$$

Damage parameter can be defined as a linear formulation as in Equation 3.8.

$$\omega = \frac{\varepsilon^{p}_{\text{eff}} - \varepsilon^{p}_{\text{failure}}}{\varepsilon^{p}_{\text{rupture}} - \varepsilon^{p}_{\text{failure}}} \text{ if } \varepsilon^{p}_{\text{failure}} \leq \varepsilon^{p}_{\text{eff}} \leq \varepsilon^{p}_{\text{rupture}} \tag{3.8}$$

where $\varepsilon^{p}_{\text{failure}}$ is the effective plastic strain at failure, $\varepsilon^{p}_{\text{eff}}$ indicates effective plastic strain, and $\varepsilon^{p}_{\text{rupture}}$ is the effective plastic strain at rupture. Features of three material models are shown in Table 3.

*MAT_ADD_DAMAGE_GISSMO (Generalized Incremental Stress State Dependent Damage Model) is a phenomenological damage mechanics model that uses a constitutive model to predict the uniformly plastic behavior before necking (Hallquist 2006).

Table 3 Features of the *MAT_24 *MAT_81 *MAT_187 material models.

| Material model | *MAT_024 | *MAT_81 | *MAT_187 |
|---|---|---|---|
| **Yield surface** | von Mises | von Mises | General over triaxiality |
| **Compression/Tension Symmetry** | × | × | ✓ |
| **Plastic Poisson's ratio** | 0.5 | 0.5 | ✓ |
| **Damage/Failure Model** | GISSMO | GISSMO | GISSMO |
| **Load Curves** | LCSS Tension | LCSS Tension | LCSS Tension/Compression |

Material model includes triaxiality dependent failure strain curve, $\varepsilon_f$, equivalent plastic strain to localization as a function of triaxiality, $\varepsilon_{v,loc}$ , the fading exponent, m and the damage exponent, n.

GISSMO gives different final results for different strain paths since the calculation is path-dependent. Measurement of damage has been developed as (Andrade[1], Feucht, and Haufe[1] 2014)

$$\Delta D = \frac{n}{\varepsilon_f} D^{\left(1-\frac{1}{n}\right)} \Delta\varepsilon_v \tag{3.6}$$

Where the exponent n is the nonlinear description of the damage, $\varepsilon_f$ failure strain that is dependent on the triaxiality and $\Delta\varepsilon_v$ is the incremental step in equivalent plastic strain. These failure strain values have to be obtained from experiments and defined as a function of triaxiality in order to cover a wide range of triaxiality values.

To simulate the instability of a material formability intensity which is covering nonlinear plastic deformation is introduced in Equation 3.9.

$$\Delta F = \frac{n}{\varepsilon_{v,loc}} F^{\left(1-\frac{1}{n}\right)} \Delta\varepsilon_v \tag{3.9}$$

Where $\varepsilon_{v,loc}$ is defined as a curve in the models and it is equivalent plastic strain to localization. Defined curve is a function of the triaxiality. $F = 0$ means material is

undeformed and $F = 1$ corresponds to a point where necking occurs.

Dcrit, is a damage threshold value that can defined as a fixed value or as a function of the forming intensity at the actual state of deformation. When the damage reaches this curve at actual triaxiality, the damage parameter *D* will be converted to critical damage, Dcrit. Hence damage is coupled to the effective stress tensor with the fading exponent m by following equation (Lemaitre 1985):

$$\sigma_r = \sigma_n \left(1 - \left(\frac{D - D_{crit}}{1 - D_{crit}}\right)^m\right) \tag{3.10}$$

The fading exponent FADEXP stands for elements that have failed in the model and do not carry any load, illustrated in Figure 34. According to the result, the elements where D=1 will be deleted (Hallquist 2006).

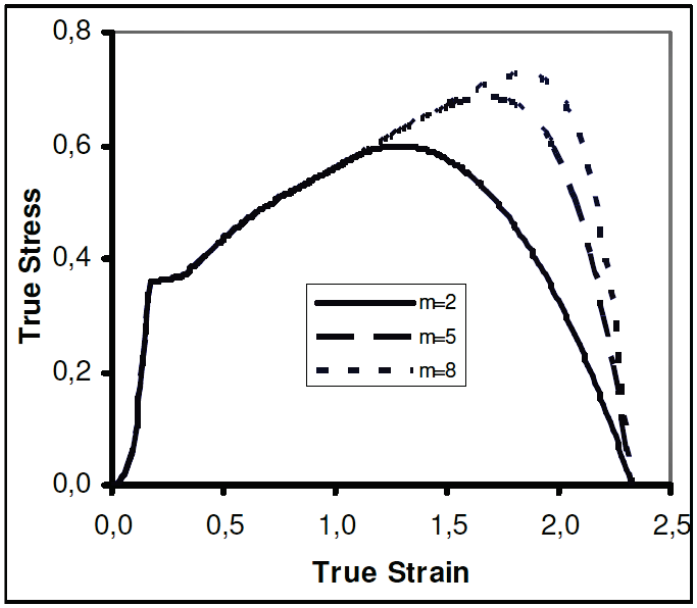


Figure 34 Effect of fading exponent (Source: Neukamm, Feucht, and Haufe 2009).

These parameters have to be found by LS-OPT which is graphical optimisation tool that successfully works with LS-DYNA. This tool provides optimal designs according to predetermined objectives, and controls simulations and post-process optimization data.

There are several approximation techniques available in LS-OPT, in this study

approximation is done with Response Surface Methodology which is used when the response of objective is affected by many of influence factors and the objective of this methodology is to optimize the response (Aydar 2018).

Force displacement curves were created from the force vs. time and displacement vs. time curves for each simulation by using crossplot feature. The number of simulations for each iteration was determined by using Equation 3.11 where i is the number of unknown parameters (Witowski, Feucht, and Stander 2011).

$$1.5 \cdot (i + 1) + 1 \tag{3.11}$$

Metamodeling techniques are necessary for design approximation due to their inexpensive computation (Wang and Shan 2007). Forward feeding neural network with space filling point selection metamodel was used for simulations which consists of neurons (seen in Figure 35) that are connected with the inputs and outputs to the system. In this network, the data moves from the input nodes to the output nodes. The objective for the optimization is to match the force vs. displacement curves obtained from the simulations with the experimentally achieved curves.

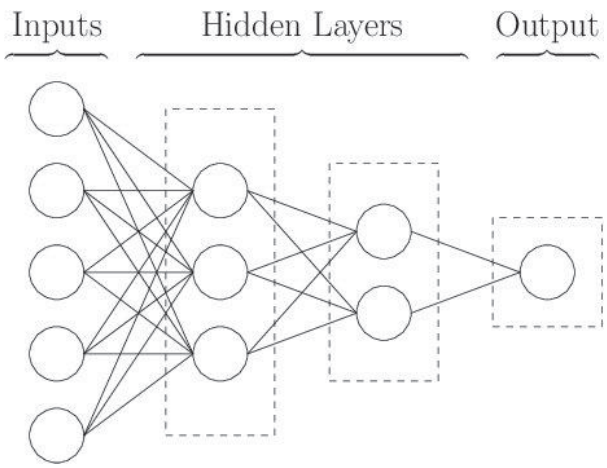


Figure 35 Neural network diagram (Source: Cinelli, Chaves, and Lima 2018)

As it is seen in Figure 36 software tries to converge to the experimentally achieved values in each step and iteration continues for a specified number of iterations or until the error is sufficiently small.

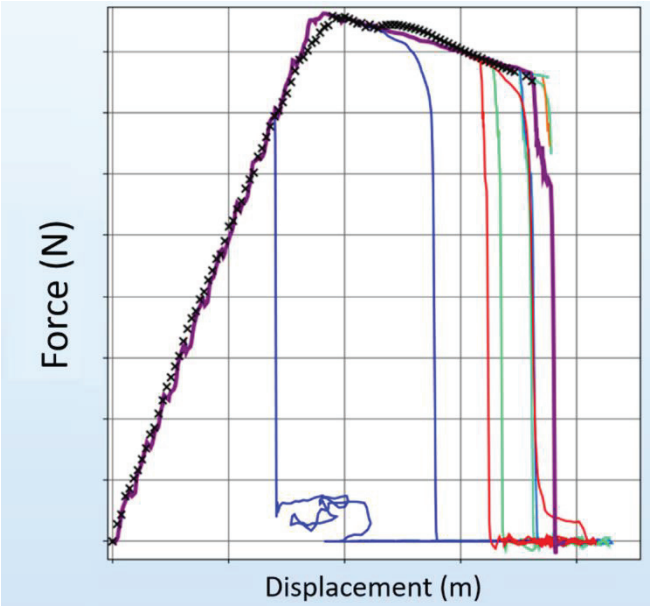

Figure 36 An example to a convergence process in LS-OPT

Parameters that need to be obtained from LS-OPT were defined in LS-PREPOST model input. LCSDG represents triaxiality dependent failure strain curve and the ECRIT denotes critical equivalent plastic strain curve. These parameters were defined as a function of triaxiality.

When finding the GISSMO parameters from the LS-OPT optimisation tool, the methodology of a study of Hörling et al. was followed and to obtain initial values and upper and lower bounds for the last optimization, numerical analyzes were done for each case separate. Then, combined LS-OPT analysis including six specimens were done to achieve global parameter values for the material (Hörling 2015). The flowchart for the combined optimization is seen in Figure 37**.**

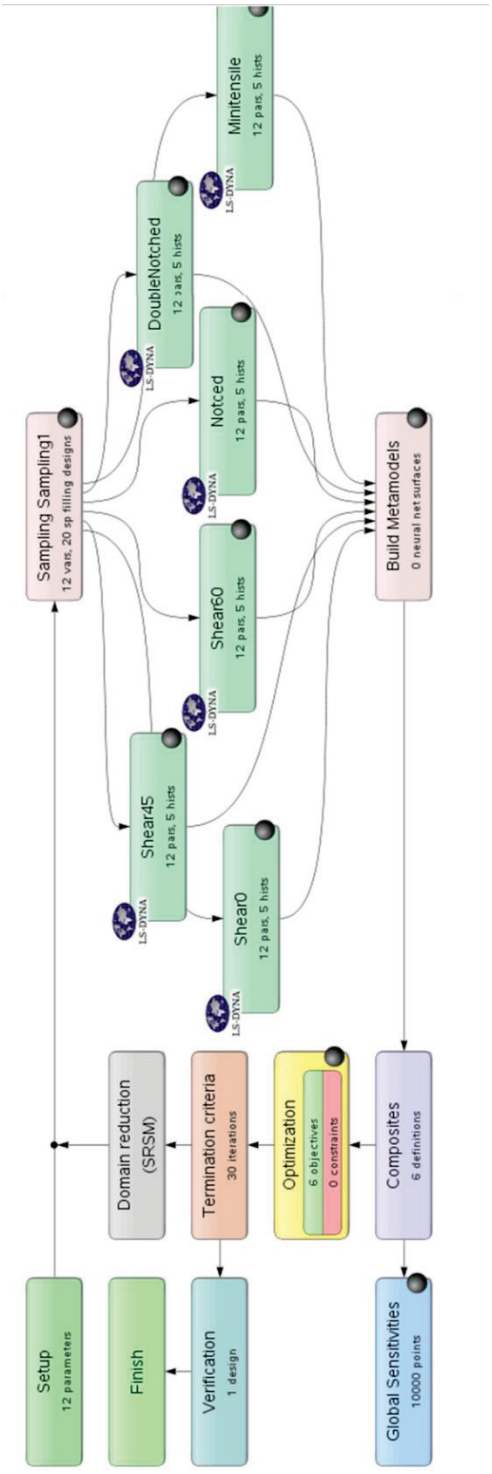


Figure 37 The flowchart in LS-OPT describing the combined optimization.

The geometries of the samples were drawn via Solidworks and meshed in Hypermesh. In Ls-PrePost, boundary conditions, material model and numerical parameters were specified.

To reduce the computational time of the quasi-static numerical models, mass scaling was defined by a positive time step of 0.001 in CONTROL_TIMESTEP card.

An element size dependency study was conducted on the quasi-static compression test with element size of 0.2 mm, 0.4 mm, 1 mm and 2 mm and as it is seen in Figure 38.a elements were independent of the size and there were no significant difference between the models until the element size of 2 mm.

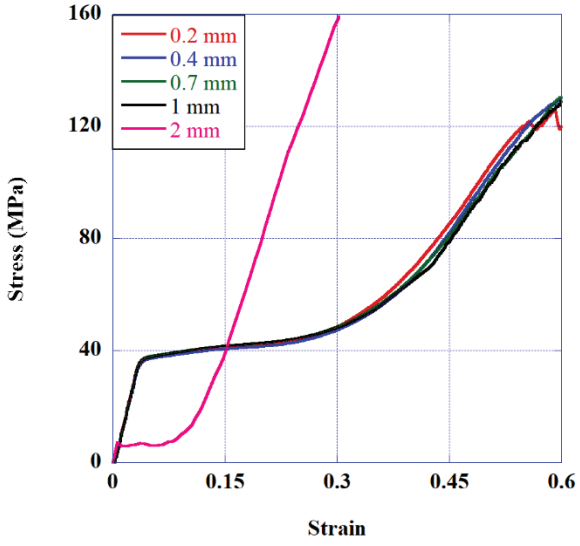


(a)

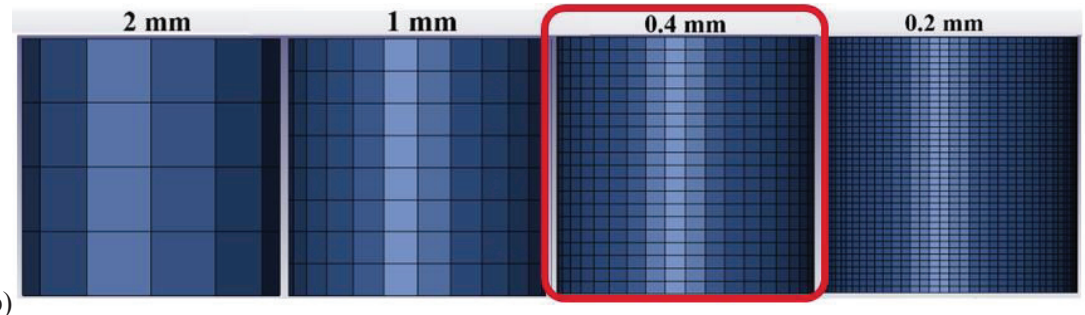


(b)

Figure 38 (a) Stress-strain curves for the compression with different element sizes (b) compression specimens meshed with 2, 1, 0.4 and 0.2 mm element size.

Element size of 1 mm could be used instead of 0.4 mm to reduce the computational cost. But as it is seen in Figure 39 with the use of 0.4 mm element size, corner radius of

the tensile specimen was well presented. Thus, element size of 0.4 mm was used in the modeling of the specimens.

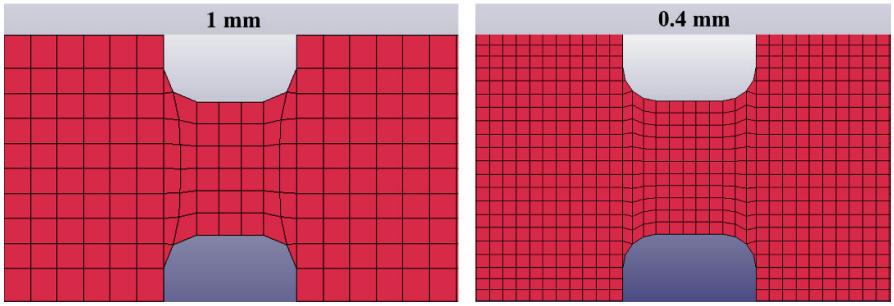


Figure 39 Custom tensile specimens meshed with 1 mm and 0.4 mm element size.

Quasi-static tensile model seen in Figure 40.a included tensile ABS sample with all DOFs locked at the bottom and all DOFs except translation in x-direction locked at the top. A displacement curve was defined in *BOUNDARY_PRESCRIBED_MOTION_SET card to a set of nodes on the upper part of the specimen in order to imitate the testing as much as possible.

In quasi-static compression model in Figure 40.b, ABS compression sample was sandwiched between upper moving plate and the bottom fixed plate. Upper plate was allowed to move only in y-direction with a constant velocity as the same as the experimental cross head velocity and all DOFs were locked for the bottom plate to prevent moving. Two *AUTOMATIC_SURFACE_TO_SURFACE contact formulation was defined between upper plate and specimen and bottom plate and specimen. An *AUTOMATIC_SINGLE_SURFACE contact was defined for specimen itself. Upper and bottom plates were modeled as *MAT_RIGID.

(a)

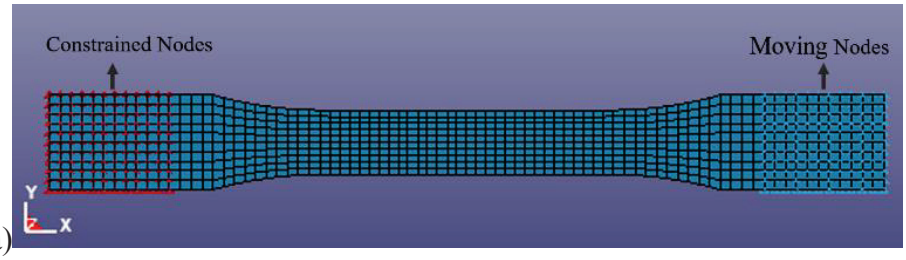

(b)

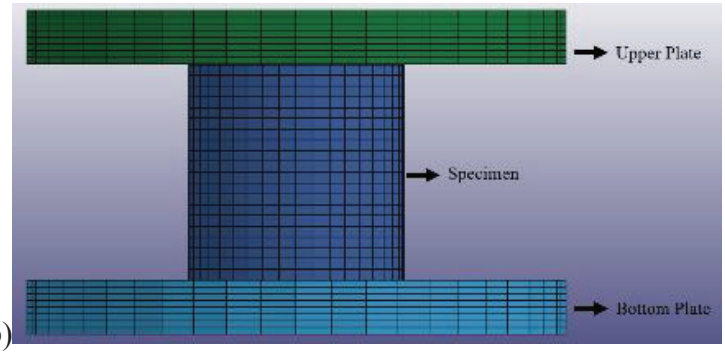


Figure 40 Quasi-static tensile (a) and compression (b) models.

For SHTB, and SHPB models explicit solver was used. Both of the SHTB and SHPB models seen in Figure 41 included ABS specimen, incident and transmitter bars and did not included striker bar. Instead, the incident stress pulse curve obtained from experiments were defined to a set of nodes on the top surface of the incident bar by using LOAD option in SEGMENT_SET keyword. In SHPB model, *ERODING_SINGLE_SURFACE contact formulation was defined between the bars and the specimen. In SHTB model, there is a matching mesh topology between the specimen and the support parts of the transmitted and incident bar. Thus matching nodes of both bars and the specimen were merged by *DUPNOD keyword so that there was no need of defining a contact formulation.

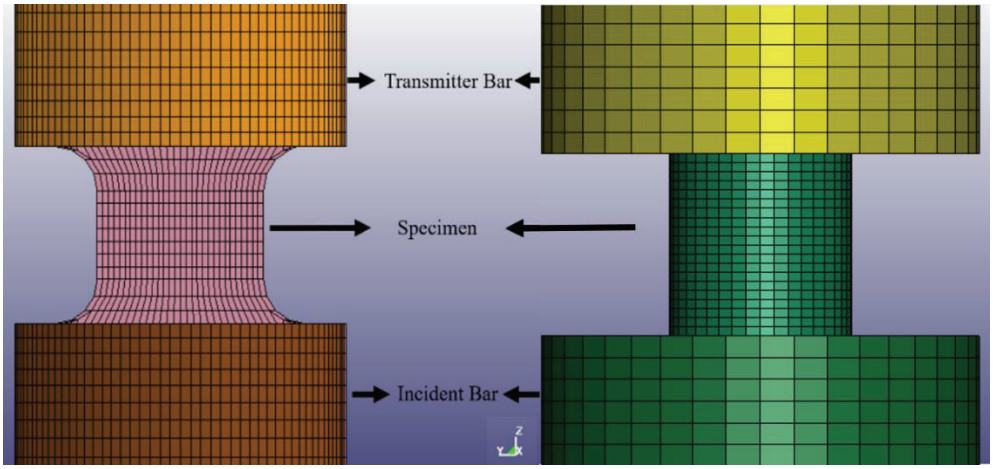


Figure 41 SHTB and SHPB models.

The displacement measurement was carried out by using *HISTORY_NODE for two nodes located at equal distance from the center.

Distance between the nodes in the models were the same with the gage length in the experiments. In the numerical models of the tensile tests, force was measured by *SECFORC and *CROSS_SECTION, the cross section was located in the center of the specimens.

Gas gun numerical model (Figure 42) consisted of ABS plate having 150 mm in length, 200 mm in width and 5mm in thickness and hardened steel projectile having 30 mm in diameter. For the projectile *JOHNSON_COOK material model was used and the velocity of the projectile was set to 121 m/s by using *VELOCITY_GENERATION option in INITIAL keyword. The JOHNSON_COOK material model constants of the hardened steel used in the model was taken from literature (Tasdemirci and Tunusoglu 2017) and are presented in Table 4.

Table 4 Johnson–Cook material model constants of the hardened steel projectile (Source: (Tasdemirci and Tunusoglu 2017).

| **Constant** | **Description** | **Value** |
|---|---|---|
| ρ(g/cm3) | Density | 7.75 |
| G (GPa) | Shear modulus | 81.8 |
| A (MPa) | Yield stress | 2000 |
| B (MPa) | Hardening constant | 477 |
| N | Hardening exponent | 0.18 |
| M | Thermal softening exponent | 1.00 |
| $T_m$ (K) | Melting temperature | 1763 |
| $T_r$ (K) | Reference temperature | 300 |
| C | Strain rate constant | 0.012 |
| $C_p$ (J/kgK) | Specific heat | 477 |
| $\varepsilon_f$ | Erosion strain | 2.0 |
| $\dot{\varepsilon_0}$ (1/s) | Reference strain rate | 1.0 |

To apply boundary conditions, set of nodes located on the top surface and bottom surface of each right and left sides of the ABS plate were fully constrained in translational and rotational displacements by using *SPC_SET keyword. ERODING_SINGLE_SURFACE contact was used between the projectile and ABS plate.

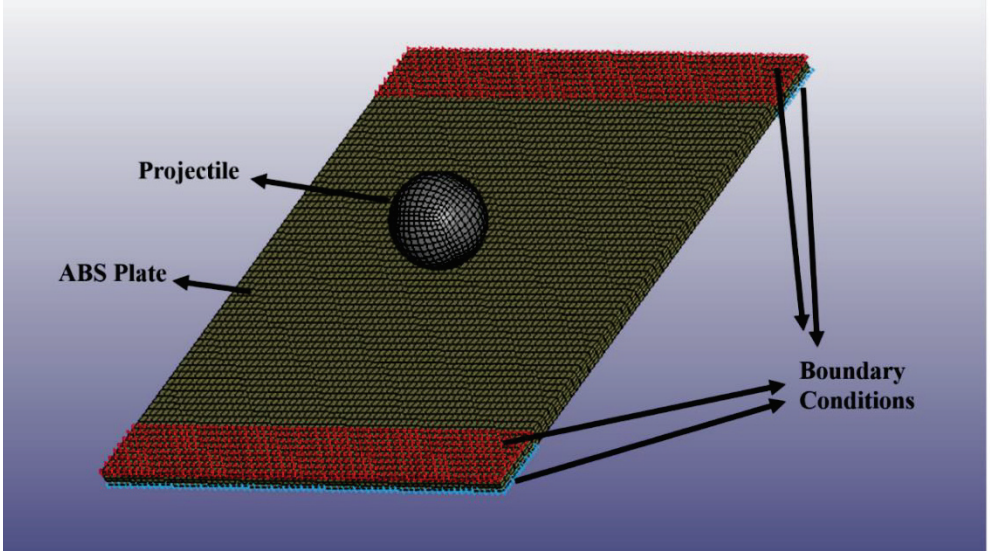


Figure 42 Gas gun model.

Material model constants were determined using both results of experiments and numerical analysis. First, the mass density of the FDM built ABS samples was found by dividing the mass by volume and it was calculated as 1000 kg/m$^3$. Effective stress vs. effective plastic strain curves which were determined from experiments were defined in *DEFINE_CURVE keyword. To take strain rate sensitivity into account effective stress vs. effective plastic strain curves corresponding for each strain rate value were defined in *DEFINE_TABLE keyword and these tables were defined in used material models by *LCSS option.

# CHAPTER 4

# EXPERIMENTAL RESULTS AND CHARACTERIZATION

## 4.1. Introduction

To determine material model parameters and strain rate sensitivity of the FDM buit ABS material tests at quasi-static and high strain rates were performed. Thus, three different strain rates for quasi-static tests and three different striker velocities for the tests were aimed. Stress-strain curves of each test were calculated accordingly. Strain rate and stress equilibrium histories for the static and dynamic test are presented.

## 4.2. Experimental Results

Experimental results were explained in the following sections. First, numerical model parameters were obtained through quasi-static and high strain rate tests.

### 4.2.1 Quasi-static Tension and Compression Test Results

Quasi-static test results are presented in this section. Using these results most of the material model constants were obtained. Tensile tests were performed to determine tensile strength of the FDM built ABS polymer. For the quasi-static tests, specimens were tested at three different strain rates which are $10^{-3}$, $10^{-2}$, and $10^{-1}$ $s^{-1}$ respectively to determine the strain rate dependent material model parameters. Crosshead speeds of 0.05 mm/s, 0.5 mm/s and 5 mm/s corresponding to strain rates of $10^{-3}$ $s^{-1}$, $10^{-2}$ $s^{-1}$, $10^{-1}$ $s^{-1}$, respectively, were selected for the test machine.

First, quasi-static tension tests were completed at $10^{-3}$ $s^{-1}$ strain rate. Tensile stress-strain curves for the tests recorded by video extensometers are presented in Figure 43. Two gage markers were bonded to the specimens in order to trace the displacement during the test. It was found that yield stress and failure strain values are approximately 21 MPa and 0.065 respectively for three tests. The duration of tests at $10^{-3}$ $s^{-1}$ strain rate

took 240 seconds approximately. Figure 43.b shows that tests has approximately 25 MPa yield stress and 0.07 failure strain.

The last group of quasi-static tensile tests was performed at 10-1 s-1 strain rate having 5 mm/s cross-head speed. It was found that yield stress and failure strain values are approximately 29 MPa and 0.049 respectively for three tests.

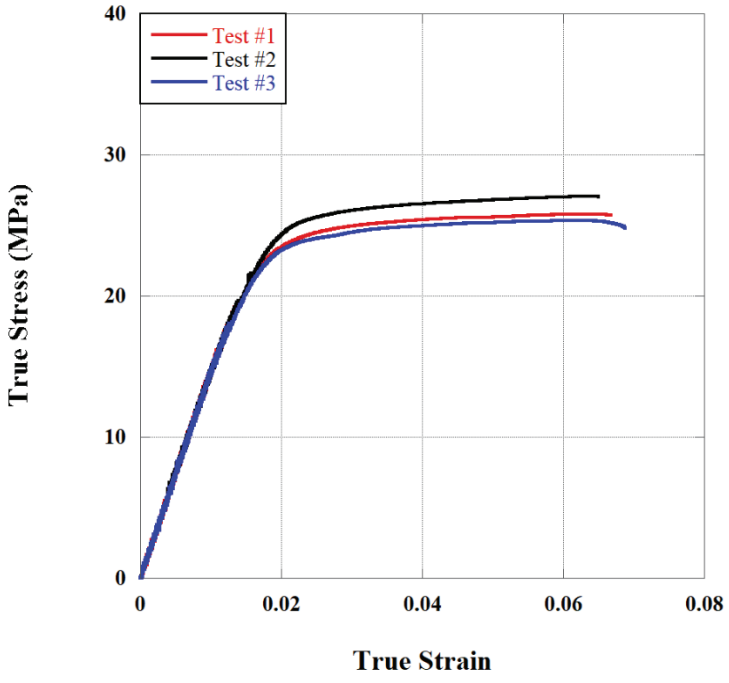


(a)

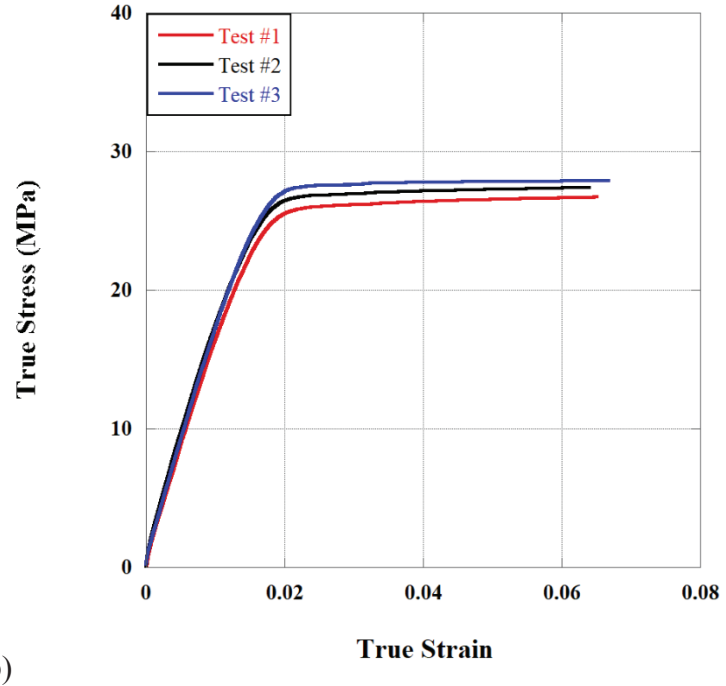


(b)

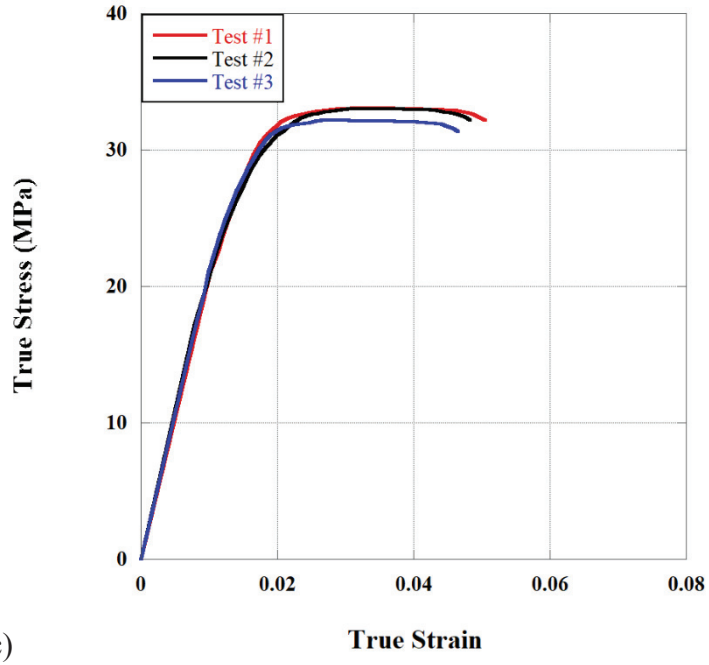


(c)

Figure 43 Stress-strain curves of the FDM built ABS obtained from quasi-static tensile tests at (a) $10^{-3}$ $s^{-1}$s, (b) $10^{-2}$ $s^{-1}$, and (c) 10-1 s-1 strain rates.

It is clearly seen that strength increased with increasing strain rate. Similar findings were also observed in the literature (Peterson et al. 2015). Yield stresses were recorded approximately as 21 MPa, 25 MPa, and 29 MPa for strain rates of $10^{-3}$ $s^{-1}$, $10^{-2}$ $s^{-1}$, and $10^{-1}$ $s^{-1}$, respectively (Figure 44). On the contrary, it is seen that failure strains of specimens decrease with increasing strain rate. Average stress and strain values corresponding for each strain rate are presented in Table 5.

Table 5 Mechanical properties of FDM built ABS at quasi-static strain rates.

| **Strain Rate ($s^{-1}$)** | **Avg. Stress (MPa)** | **Avg. Strain** |
|---|---|---|
| $10^{-3}$ | 25 | 0.068 |
| $10^{-2}$ | 27 | 0.065 |
| $10^{-1}$ | 32 | 0.049 |

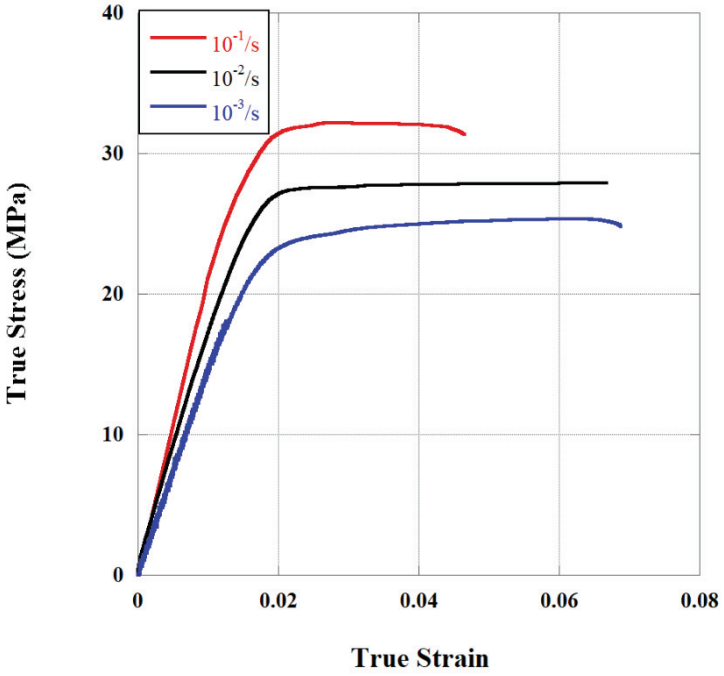


Figure 44 Comparison of tensile stress-strain curves at strain rates of $10^{-3}$ $s^{-1}$, $10^{-2}$ $s^{-1}$, and $10^{-1}$ $s^{-1}$ .

Quasi-static compression tests were also performed on the FDM built ABS specimens having 8mm diameter and 8 mm height to determine compressive strength of the polymer. Velocities of 0.008 mm/s for $10^{-3}$ $s^{-1}$ strain rate, 0.08 mm/s for $10^{-2}$ $s^{-1}$ strain rate, and 0.8 mm/s for $10^{-1}$ $s^{-1}$ strain rate were selected as crosshead speed. Two gage markers were also used to record displacement in the specimens. The quasi- static compression stress strain curves for the strain rates of $10^{-3}$/s, $10^{-2}$/s and $10^{-1}$/s are illustrated in Figure 45. The yield stress values were recorded as 36.7, 38.7 and 43 MPa, respectively.

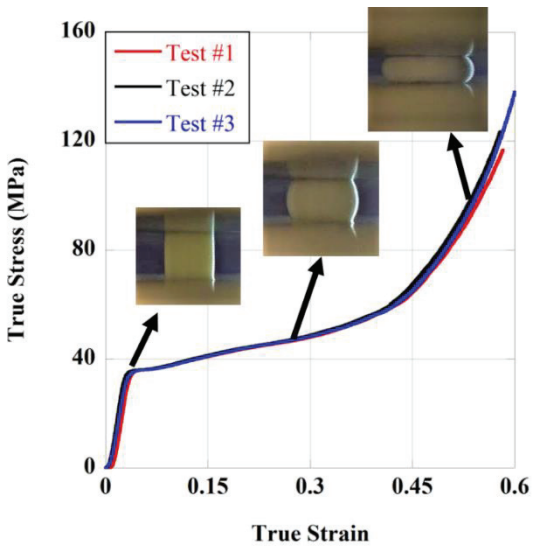


(a)

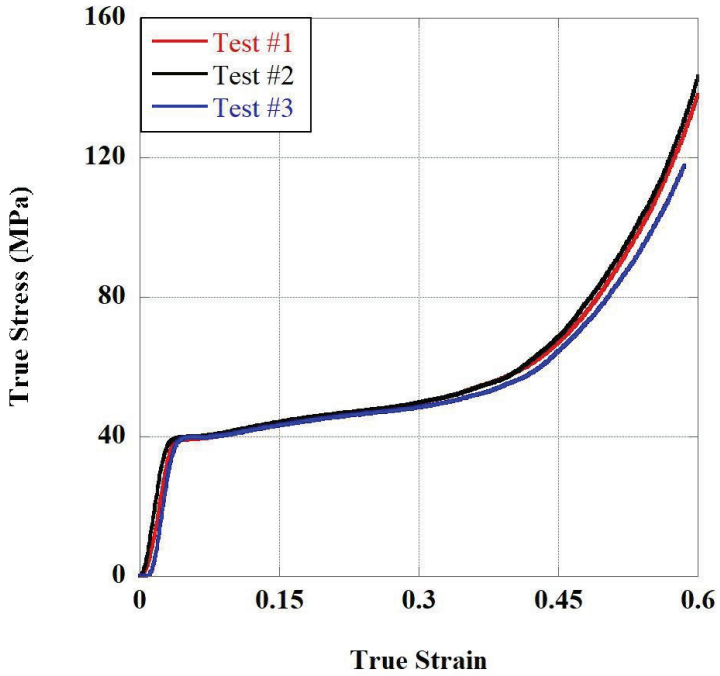


(b)

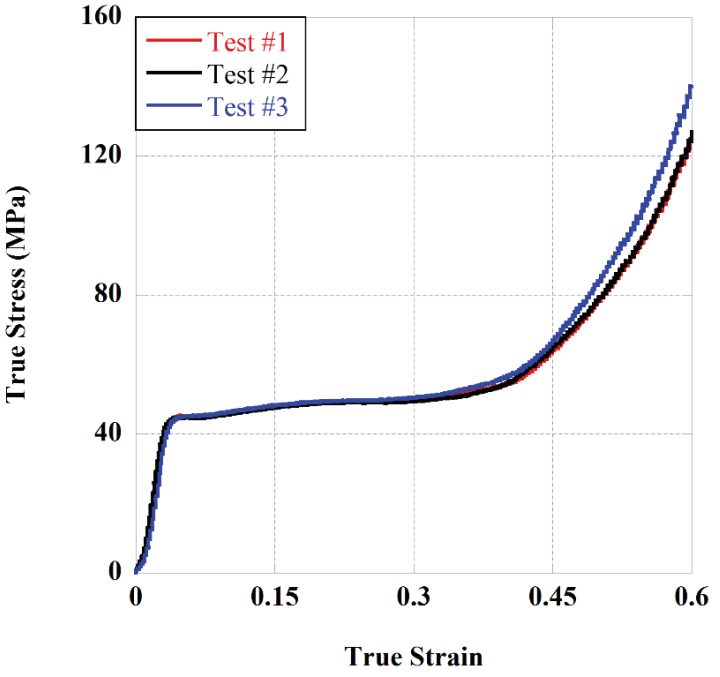


(c)

Figure 45. Stress-strain curves of FDM built ABS obtained from quasi-static compression tests at (a) 10-3 $s^{-1}$ s, (b) $10^{-2}$ $s^{-1}$, and (c) $10^{-1}$ $s^{-1}$ strain rates

Comparison of the stress-strain curves of the FDM built ABS polymer at strain rates of are illustrated in Figure 46. The material exhibited strain rate dependent behavior under compression similar to the behavior under tension loads.

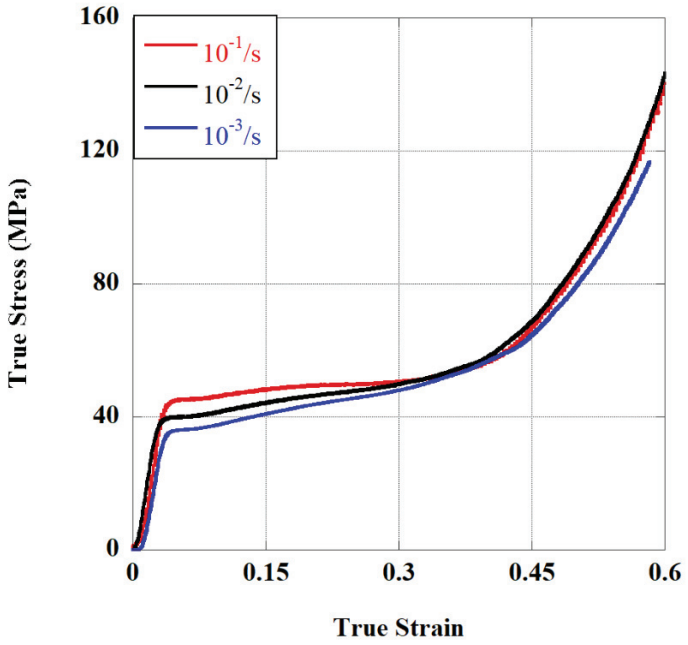


Figure 46 Comparison of compressive stress-strain curves at different strain rates

### 4.2.2 High Strain Rate Tension and Compression Tests

For dynamic mechanical characterization of FDM built ABS, SHTB and SHPB tests were conducted. For SHTB tests of the FDM built ABS, custom specimen shown in Figure 21 was used.

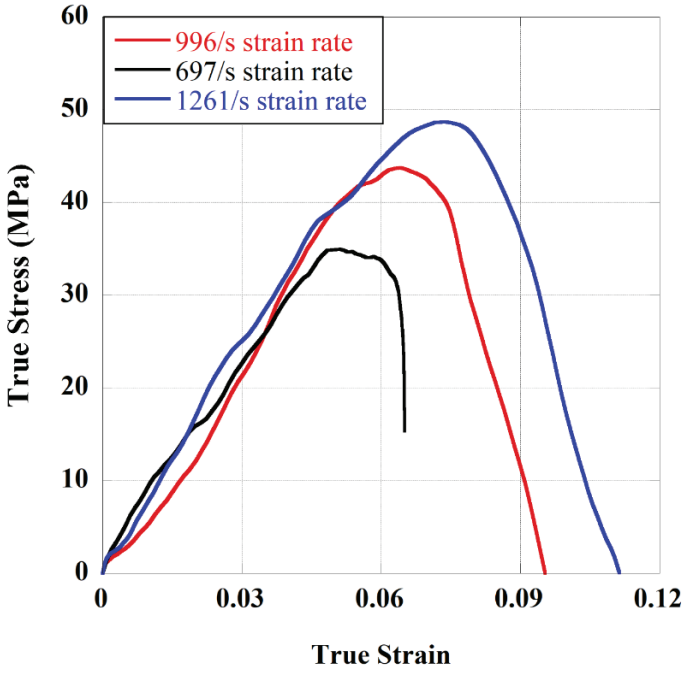


Figure 47 Comparison of tensile stress-strain curves obtained from SHTB at different strain rates

The dynamic tensile mechanical behavior of the specimen is shown in Figure 47. The failure strain values recorded approximately as 0.0061, 0.079, 0.083 for the average strain rates of 697/s, 996/s, 1261/s and the tensile strength at failure was measured as 30MPa, 35MPa, 46.5 MPa, respectively. Results of the dynamic tensile tests showed that the tensile strength is increased when the applied loading rate is increased as well. In contrast, at high strain rate tensile tests, as the strain rate increased failure strain is increased also.

Subsequently, SHPB tests were conducted on the specimen having 8mm in diameter and 8 mm in length.

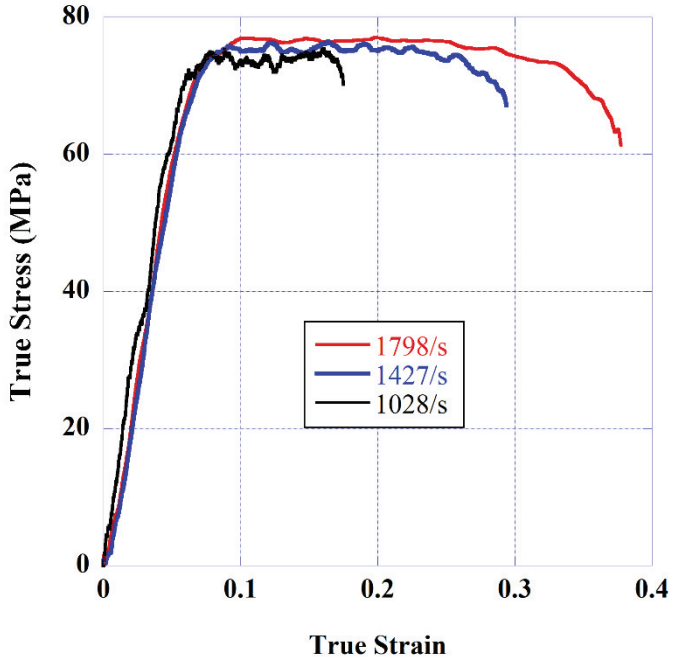


Figure 48 Comparison of compressive stress-strain curves obtained from SHPB at different strain rates

Figure 48 shows the compressive stress–strain curves of the FDM built ABS plastic at average strain rates of 1028/s, 1427/s and 1798/s. The yield stress and the maximum stress were recorded approximately as 67.8 and 76 MPa, respectively. Obtained values were consistent with the values in the literature which were conducted under the same loading conditions (Jami, Masood, and Song 2013). It is also noted that as strain rate increases, the maximum stress increases and the loading ends at higher strain values.

## 4.3 Numerical Results

Numerical analyzes were performed after obtaining parameters by conducting quasi-static and high strain rate tests. Comparison of the quasi-static tensile stress-strain curves obtained from experimental studies and numerical analyses that are modeled with *MAT_24, *MAT_81 and *MAT_187 material models are illustrated in Figure 49.

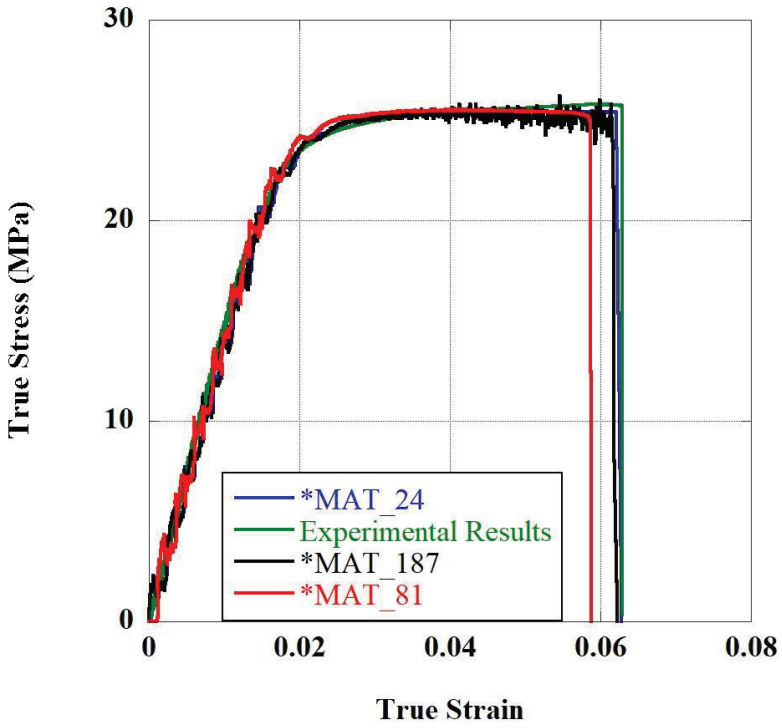


Figure 49 Comparison of material models for quasi-static tensile test

The fitted stress-strain curves has a good match in appearance and the failure stress value well correlated between the datasets. *MAT_24 and *MAT_187 models predicted the failure strain values but *MAT_81 model acted more brittle than reality and failed earlier than the experiment. Figure 50 displays the failure of the specimens simulated with *MAT_24, *MAT_81 and *MAT_187 and the specimen used in experiment.

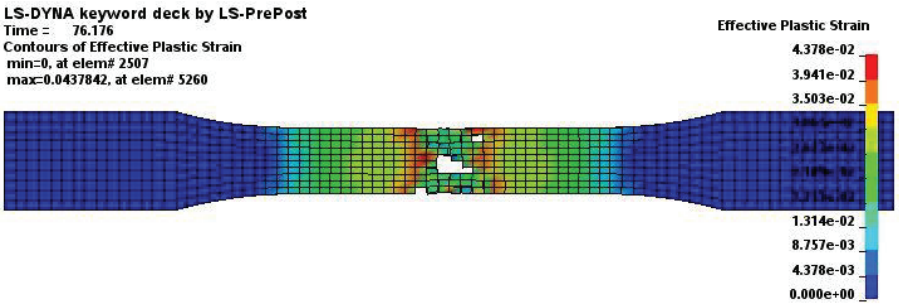


(a)

*MAT_24

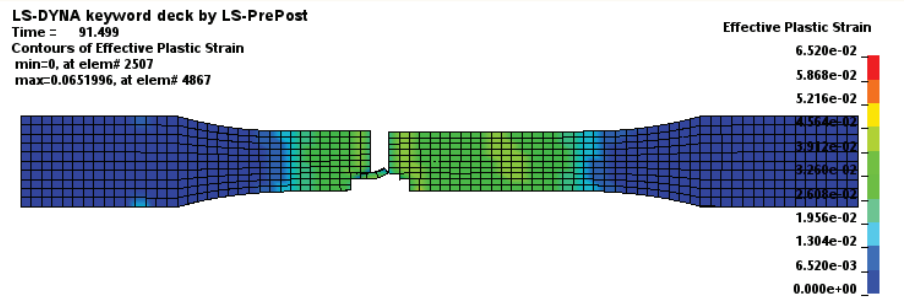


(b)

*MAT_81

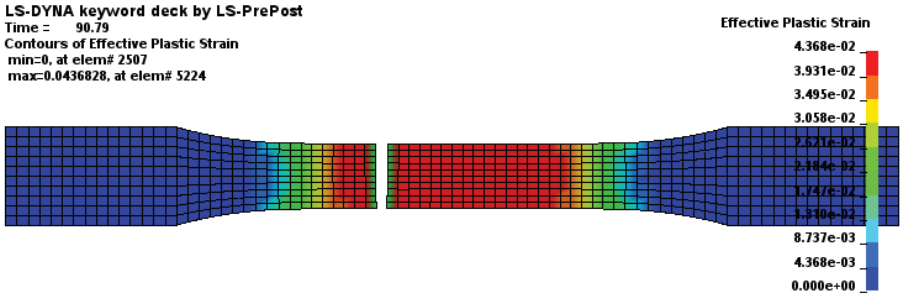


(c)

*MAT_187

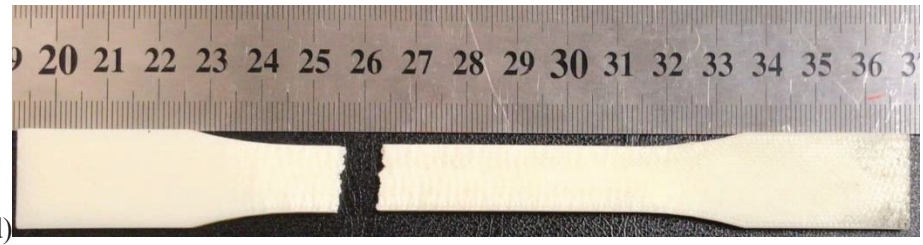


(d)

Figure 50 The D638 specimen at failure states (a) *MAT_24 (b) *MAT_81 (c) *MAT_187 (d) experiment.

Next, numerical analyzes were performed on the quasi-static compression tests. Fitted compressive stress-strain curves are shown in Figure 51. Material models well predicted the yield point but *MAT_187 model displayed inconsistent behavior in the densification region.

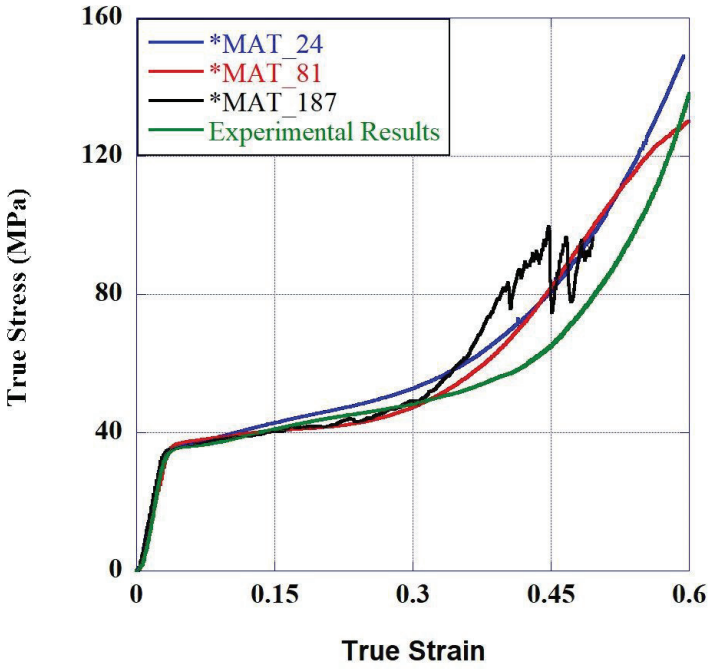


Figure 51 Comparison of material models for quasi-static compression test

Numerical studies were also conducted at the high strain rate tensile tests. The comparison of numerical models with the experiments is indicated in Figure 52.

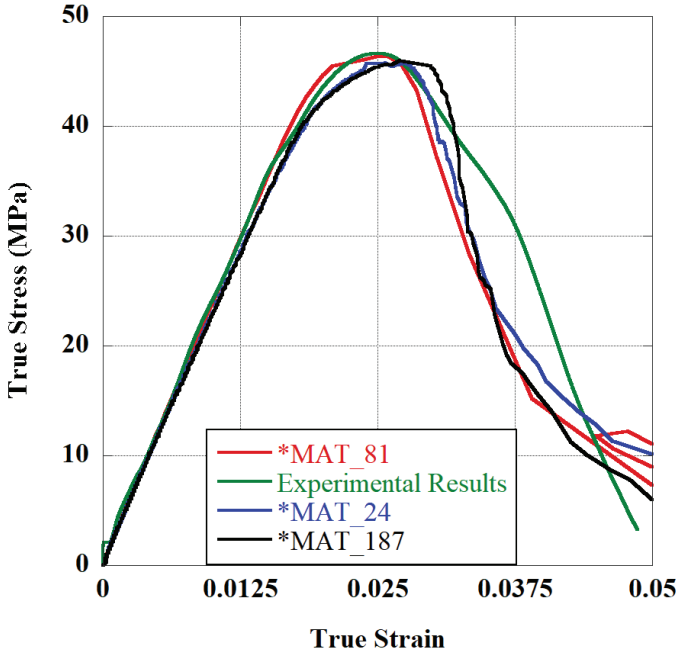


Figure 52 Comparison of material models for dynamic tensile test

The fitted curves showed that numerical models were able to predict dynamic tensile strength of the polymer. But results showed that all numerical models were failed to predict the failure strain and showed more brittle behavior in simulations than in the experiments.

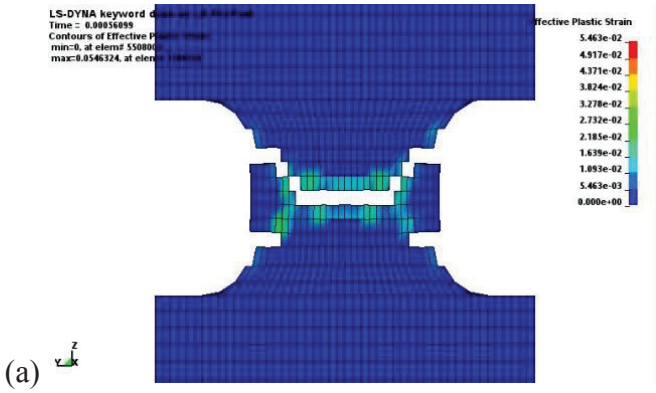


(a)

*MAT_24

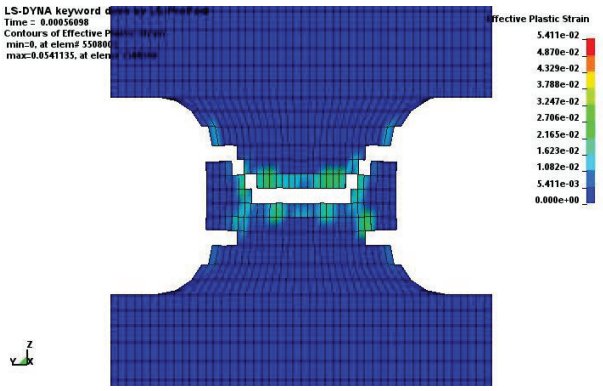


(b)

*MAT_81

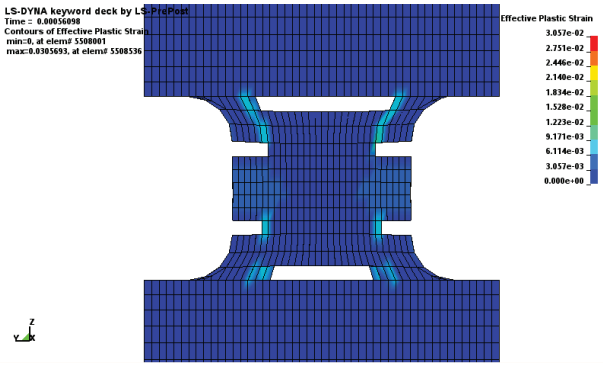


(c)

*MAT_187

(d) 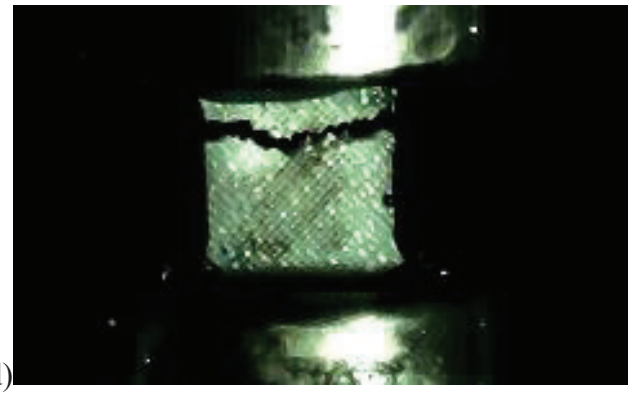

Figure 53 Failure states at STHB test, numerical and experimental comparison (a) *MAT_24 (b) *MAT_81 (c) *MAT_187 (d) experiment.

Failure modes of the specimens modelled with *MAT_24, *MAT_81 and *MAT_187 material models and the specimen used in experiment are shown in Figure 53. Numerical models with *MAT_24, *MAT_81 has a good match in appearance but *MAT_187 failed to produce a solution with accuracy.

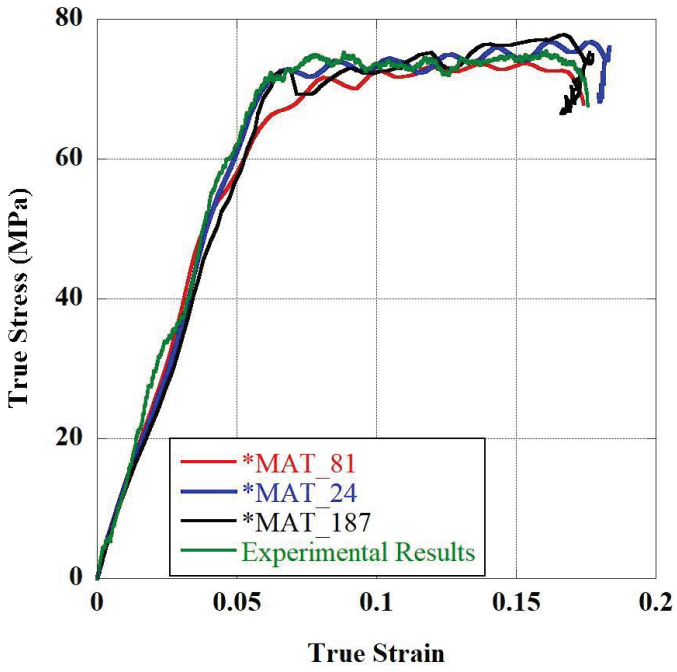


Figure 54 Comparison of material models for dynamic compression test.

Then comparison of the material models were conducted at SHPB test. The fitted stress-strain curves (Figure 54) has a good agreement in terms of maximum stress and

maximum loading values. As in the quasi-static compression test simulation, *MAT_187 models displayed inconsistent behavior at failure.

After compression and tension tests, gas gun test which was applied to a FDM built ABS plate having 5 mm in thickness was numerically modelled. Elastic modulus and effective stress vs. effective plastic strain curves obtained from mechanical characterization tests were defined in gas gun model input. Experimental velocities of the projectile before and after penetrating ABS plate having 5 mm in thickness are recorded as 121 m/s and 107.73 m/s, respectively. Front and back face of deformed ABS is illustrated in Figure 55.

Figure 55 Front and back face of the deformed ABS plate.

Numerical analyzes of gas gun test were also performed for the plates having 3 mm, 7 mm and 9 mm in thickness to observe the effect of the change of thickness. Comparison of initial and final velocity of the projectile for MAT_24 and MAT_187 material models for different thickness values are shown in Figure 56.

The specific absorbed energy (SAE) graphs, obtained by dividing the area under the numerical force vs. displacement curve by the mass are illustrated in Figure 57 for *MAT_24 and *MAT_187 material models.

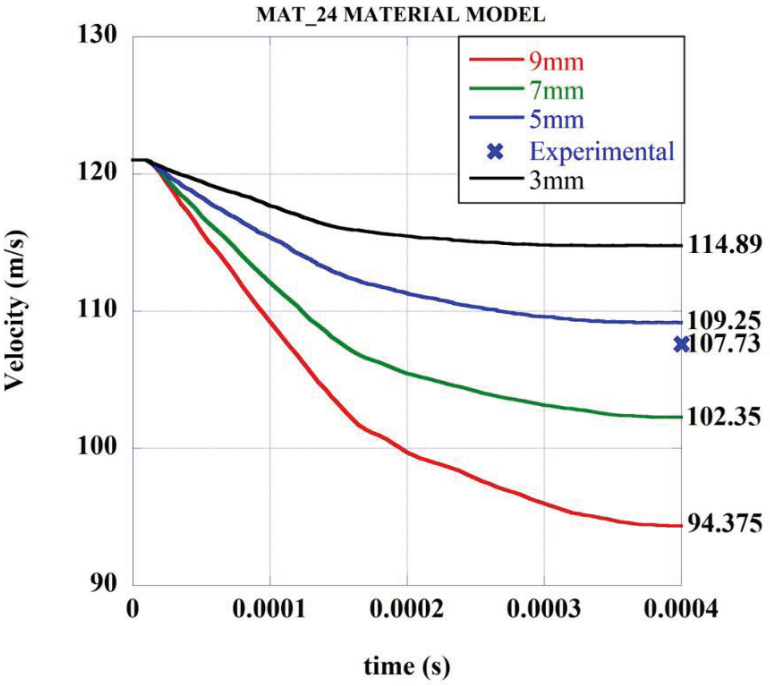


(a)

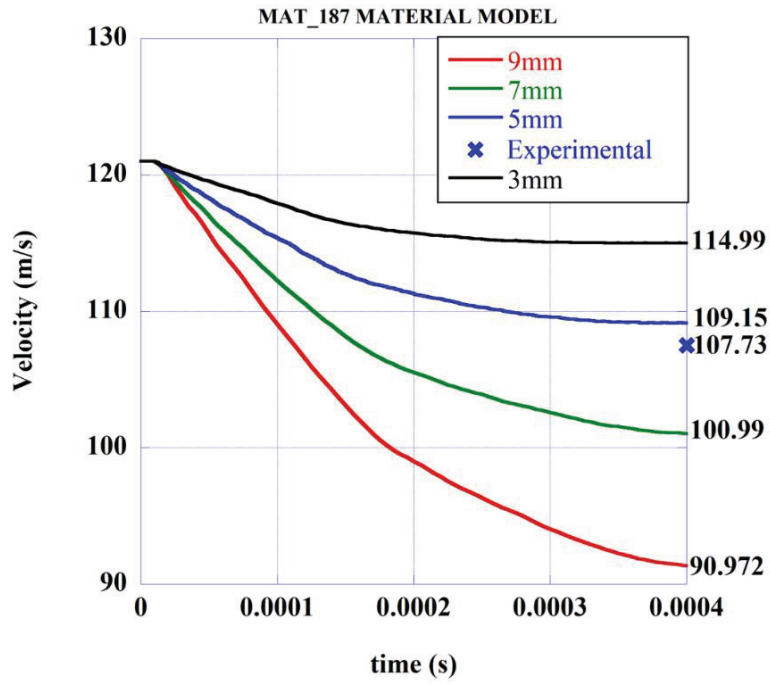


(b)

Figure 56 Comparison of initial and final velocity of the projectile for (a) MAT_24 and (b) MAT_187 material models for different thickness values.

Results showed that energy absorption was 10% and 6% higher in specimens that are modeled with *MAT_187 and having 9 mm and 7 mm in thickness, respectively. And energy absorption levels for *MAT_24 and *MAT_187 were nearly equal in the specimens having 5 mm and 3 mm in thickness.

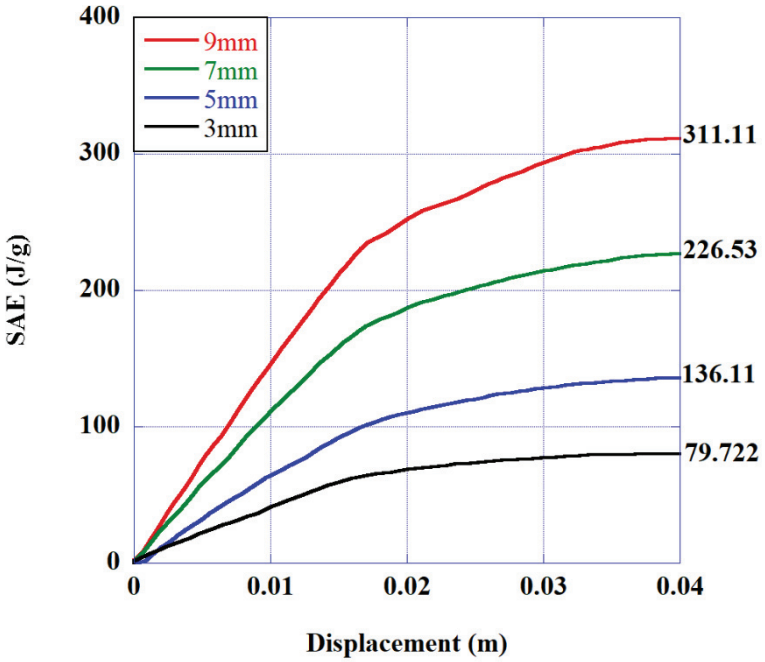


(a)

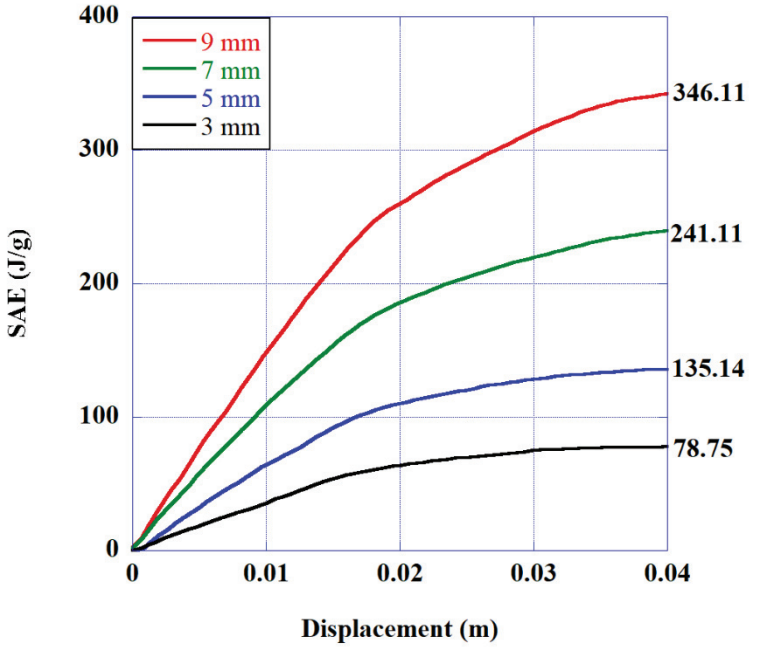


(b)

Figure 57 Comparison of SAE-Displacement Graphs for (a) MAT_24 and (b) MAT_187 material models for different thickness values.

### 4.3.1. Integration of GISSMO

The calibration of the GISSMO for the description of damage consists essentially in the determination of the fracture curve $\varepsilon_f(\eta)$, instability curve $\boldsymbol{\varepsilon}_{v,loc}$, damage exponent n, and fading exponent m . In order to obtain these parameters preliminary numerical

models of notched, shear and tensile specimens were created. The specimens, with an element size of 0.5 mm, were tested under a tensile load and damage criteria was added to the *MAT_24 material model. The reason of choosing *MAT_24 in GISSMO analyzes is because the material model showed stability in all numerical analyzes especially under compressive loadings. LS-OPT analyzes were done separately for each case to make sure that the models were accurate and to get close initial values for the combined optimization.

The main reason of the optimization is to match the force vs. displacement curves obtained from the numerical models with the experimentally obtained curves with as small error as possible. An initial value and upper and lower values were set so that the software could choose the parameters for the simulations. The flowchart for the optimization of one example case is seen in Figure 58.

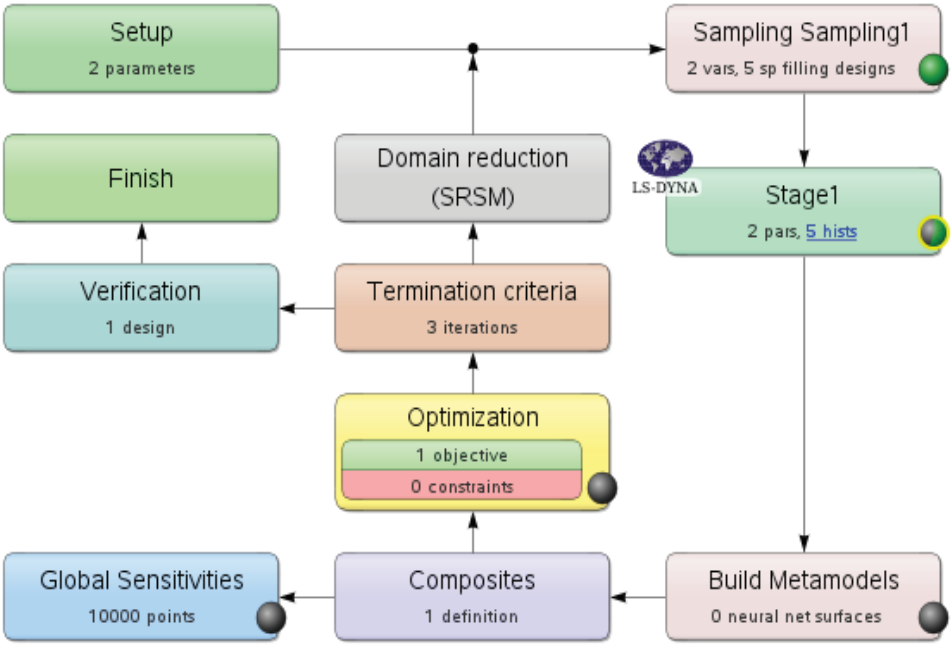


Figure 58 Flowchart in LS-OPT analysis describing the optimization of shear 60º case.

Then, the optimization was done for all specimen geometries at the same time in order to get good parameters and to make GISSMO able to predict different load cases. In this case the number of unknown parameters is 12. Therefore, 20 simulations had to be performed in each case according to Equation 3.5.

The GISSMO curves obtained from the combined LS-OPT analysis can be seen in Figure 59 and the corresponding parameters can be seen in Table 6.

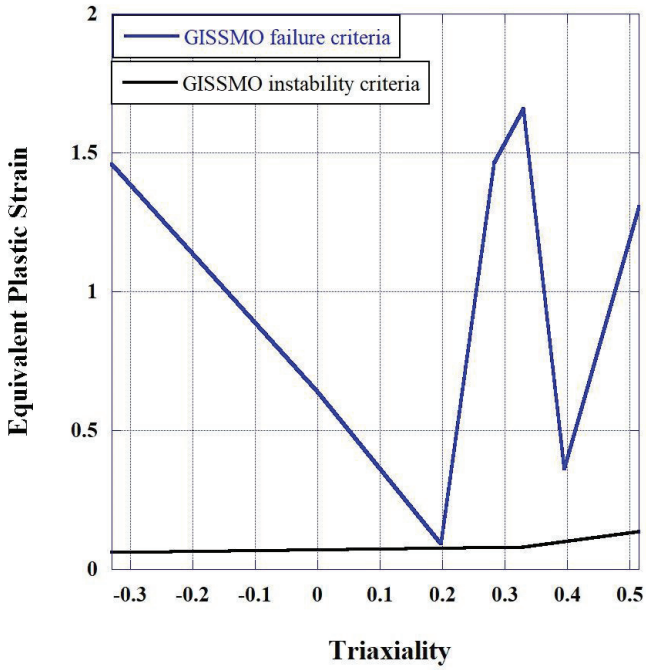


Figure 59 The GISSMO instability and failure criteria curves for all cases.

Table 6 The best parameters achieved from LS-OPT® for all cases

| **a1** | **a2** | **a3** | **a4** | **a5** | **a6** | **a7** |
|---|---|---|---|---|---|---|
| 1.4600 | 0.63834 | 0.090724 | 1.4645 | 1.6574 | 0.36156 | 1.3066 |
| **b1** | **b2** | **b3** | **m** | **n** | | |
| 0.060168 | 0.081234 | 0.13682 | 11.6087 | 2.62602 | | |

Peak force and displacement values for the specimens representing a specific triaxiality state obtained from the experiments are presented in the following sections. Single and multi case optimizations were compared with experimental data and results were discussed.

### 4.3.1.1. Double Notched

Experimental peak force of the double notched specimen was recorded approximately as 197 N and displacement value was determined as 0.6 mm. Force-displacement curves of the double notched specimen obtained from the single case optimization and the experiments are presented in Figure 60.

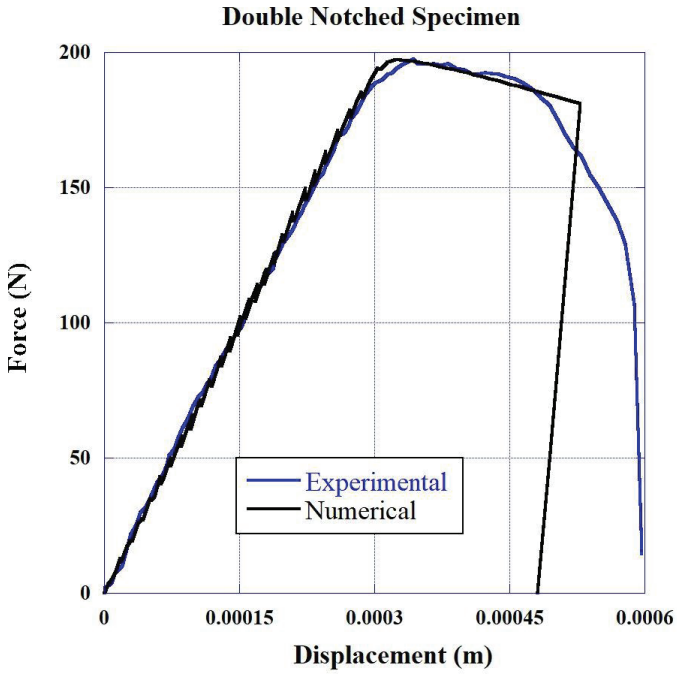


Figure 60 Experimental vs. single case optimization force–displacement curves of the double notched specimen.

The single case optimization results were consistent with the experimental ones in terms of peak force but failed earlier than the experiments and showed more brittle behavior.

Then, multi case optimization force-displacement curve for the double notched specimen is illustrated in Figure 61 together with the experimental data.

There was a good correspondence between the simulation and experiment in terms of peak force but simulation failed to predict the maximum displacement value and exhibited more brittle behavior as in the single case optimization.

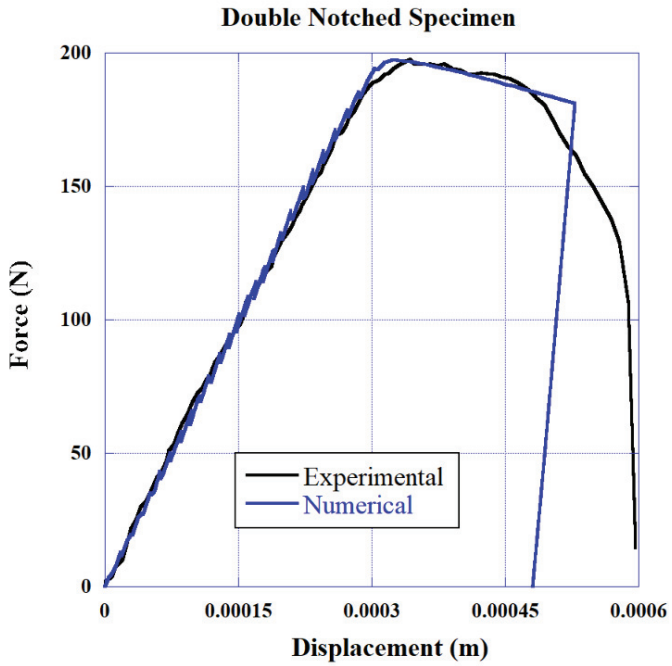


Figure 61 Experimental vs. multi case optimization force–displacement curves of the double notched specimen.

Figure 62 displays the states of failure of double notched specimen in the experiment and the single and the multi case optimization. Good agreement was observed for the localization of the deformation between both of the simulations and experiment.

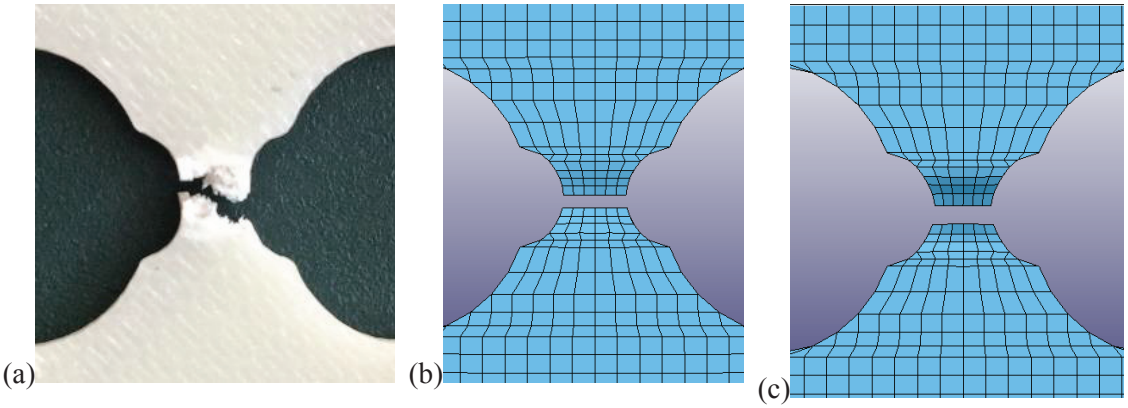


Figure 62 The state of failure of the double notched specimen in (a) experiment (b) single case optimization and (c) multi case optimization.

### 4.3.1.2. Notched

The obtained experimental peak force of the notched specimen was approximately as 220 N and displacement value was approximately as 0.9 mm. Force-displacement curves of the notched specimen obtained from the single case optimization and the experiments are presented in Figure 63.

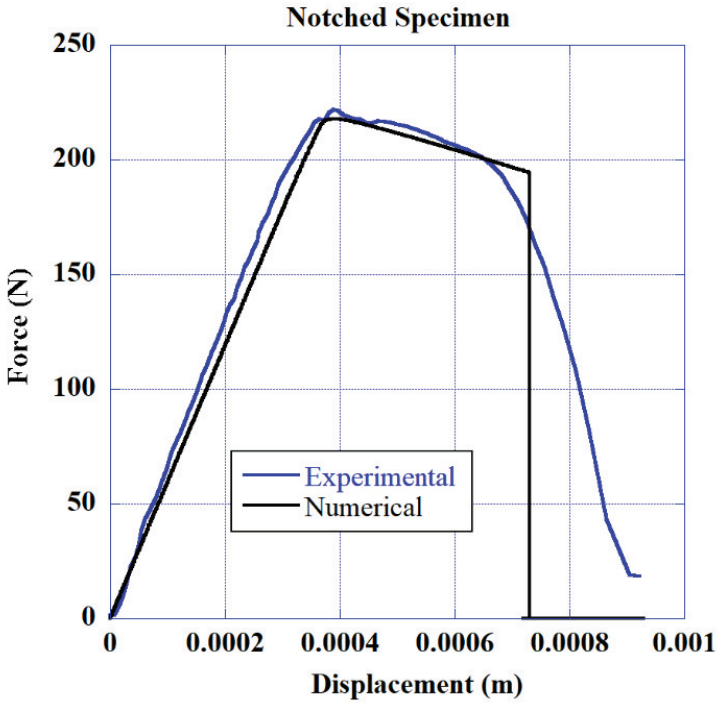


Figure 63 Experimental vs. single case optimization force–displacement curves of the notched specimen.

Single case optimization was able to capture the peak force value but exhibited more brittle behavior and failed 0.15 mm earlier than the experiment.

The fitted force displacement curve of the multi case optimization and the experiment is presented in Figure 64. Multi case optimization results showed slightly better agreement in terms of maximum displacement than the single case optimization.

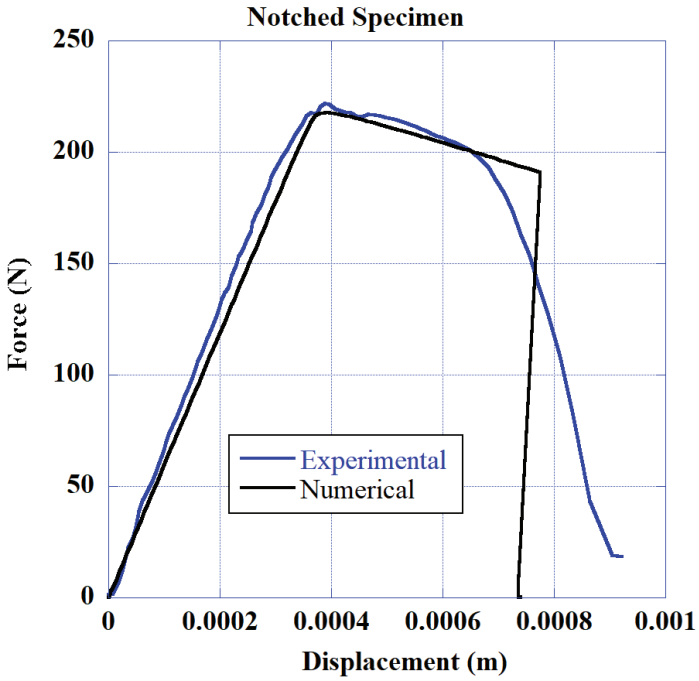


Figure 64 Experimental vs. multi case optimization force–displacement curves of the notched specimen.

States of failure of the notched specimen in the experiment and the single and the multi case optimization are shown in Figure 65. Good agreement was achieved between the numerical models and experiments for the localization of deformation.

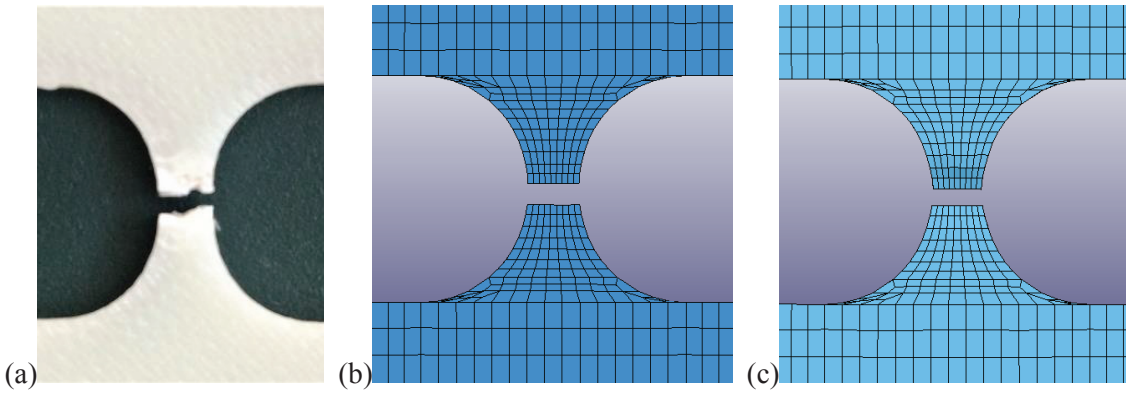


Figure 65 The state of failure of the notched specimen in (a) experiment (b) single case optimization and (c) multi case optimization.

### 4.3.1.3. Shear 0°

Peak force of the shear 0° specimen from the experiments was recorded approximately as 131 N and displacement value was determined approximately as 1.57 mm. Force-displacement curves of the shear 0° specimen obtained from the single case optimization and the experiments are presented in Figure 66.

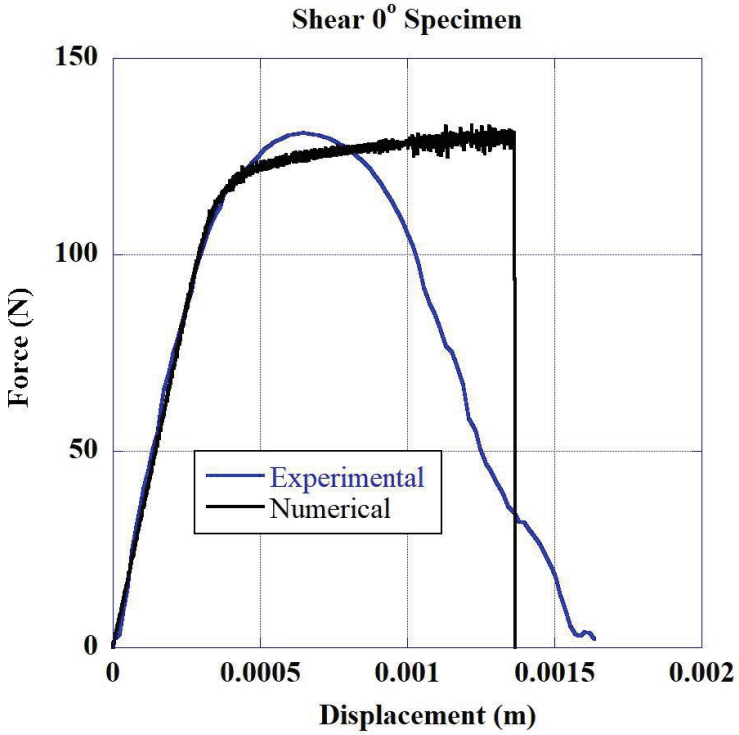


Figure 66 Experimental vs. single case optimization force–displacement curves of the shear 0° specimen.

It is clearly seen in the Figure 66, force decreased smoothly after reaching peak force in the experiment. But in the single case optimization, force proceeded increasing until a sudden failure appeared in the specimen.

The force displacement comparison of the multi case optimization and the experiment is presented in Figure 67. Smooth decrease in the force after reaching peak force was also observed in the multi case optimization. There was good agreement between the multi case optimization and the experiment in terms of maximum displacement.

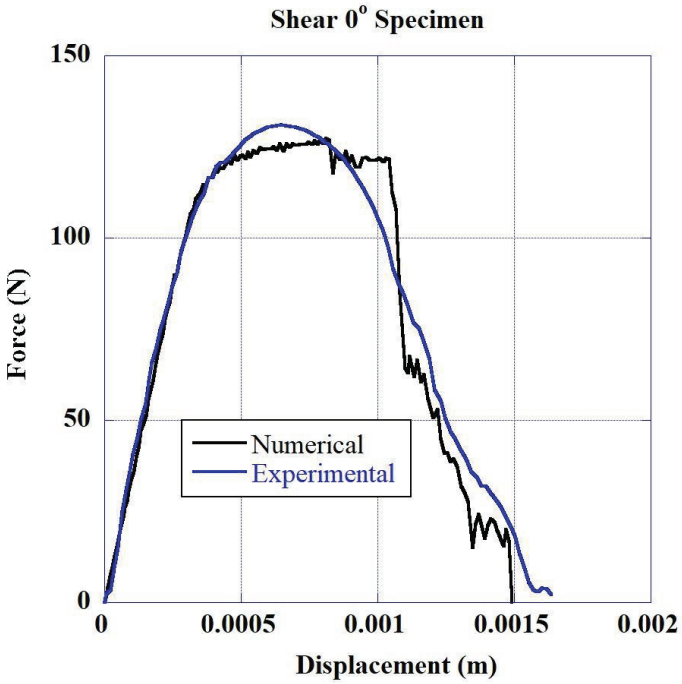


Figure 67 Experimental vs. multi case optimization force–displacement curves of the shear 0° specimen.

Figure 68 displays the failure of the shear 0° specimen used in the experiment and the simulations. The appearance of the deformation was well predicted in the multi case optimization compared to the single case optimization.

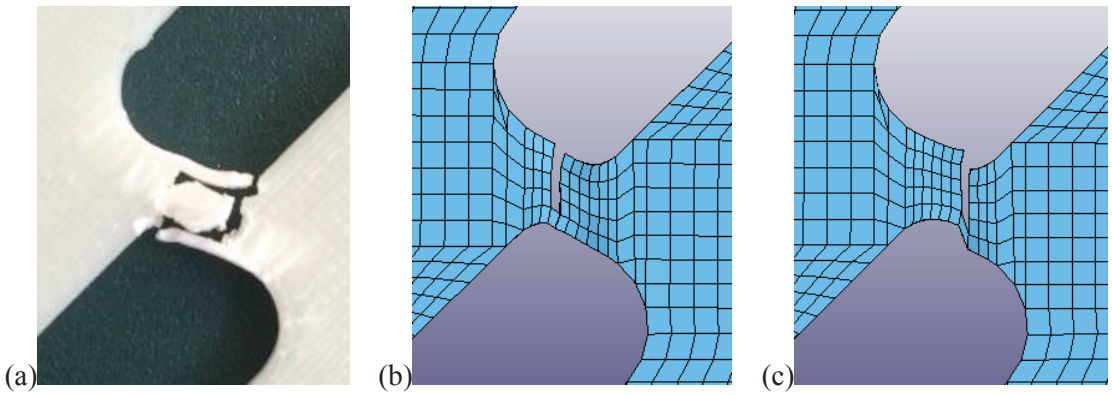


Figure 68 The state of failure of the shear 0° specimen in (a) experiment (b) single case optimization and (c) multi case optimization.

### 4.3.1.4. Shear 60°

Experimental peak force of the shear 60° specimen was recorded approximately as 280 N and displacement value was determined approximately as 1 mm. Single case optimization force-displacement curve for the shear 60° specimen is illustrated in Figure 69 together with the experimental data. The fitted force-displacement presented a good match in appearance and the peak force and maximum displacement values well correlated between the datasets.

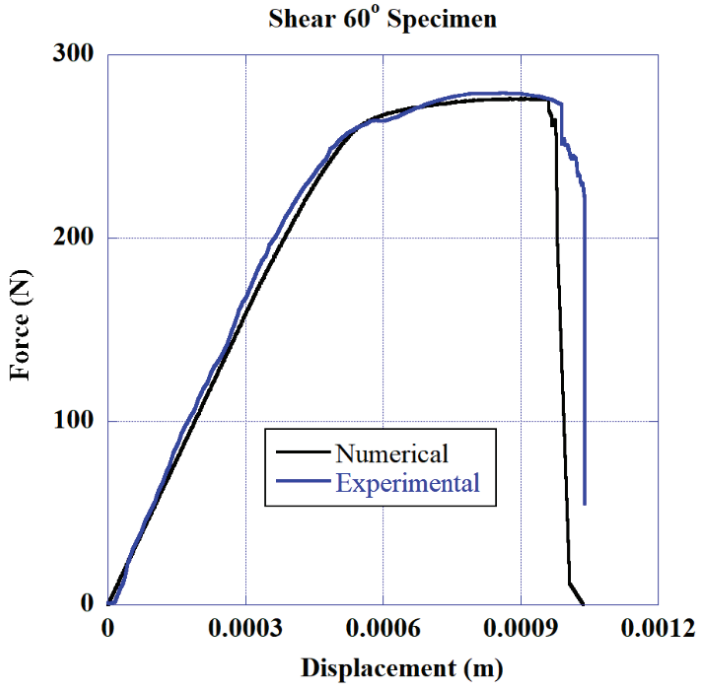


Figure 69 Experimental vs. single case optimization force–displacement curves of the shear 60° specimen.

Then the multi case optimization force-displacement curve of the shear 60° specimen compared with experimental data is displayed in Figure 70. Results from the multi case optimization was consistent with the experimental ones in terms of peak force but failed later than the experiments and showed more ductile behavior.

Figure 71 presents the failure of the shear 60 ° specimens used in the experiment and the simulations. The appearance and localization of the deformation was well predicted in both of the single and the multi case optimizations.

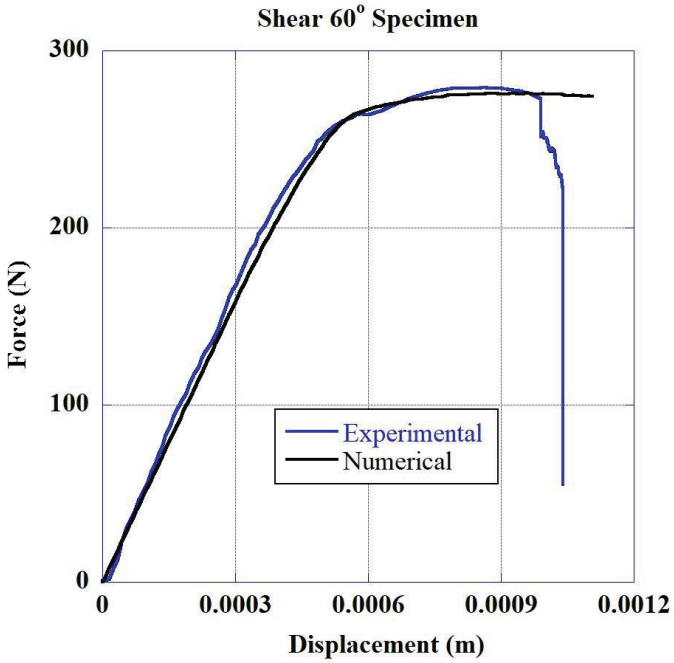


Figure 70 Experimental vs. multi case optimization force–displacement curves of the shear 60° specimen.

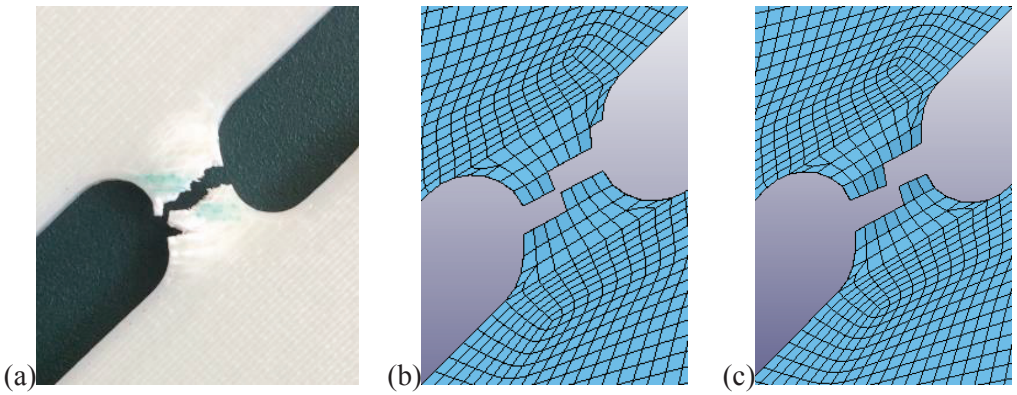


Figure 71 The state of failure of the shear 60° specimen in (a) experiment (b) single case optimization and (c) multi case optimization.

### 4.3.1.5 Shear 45°

Peak force of the shear 45° specimen in the experiments was obtained approximately as 135 N and the maximum displacement was obtained approximately as 1.9 mm. Force-displacement curves of the shear 45° specimen obtained from the single case optimization and from the experiments are presented in Figure 72. The peak force and maximum displacement values were well predicted in the single case optimization of the shear 45° specimen.

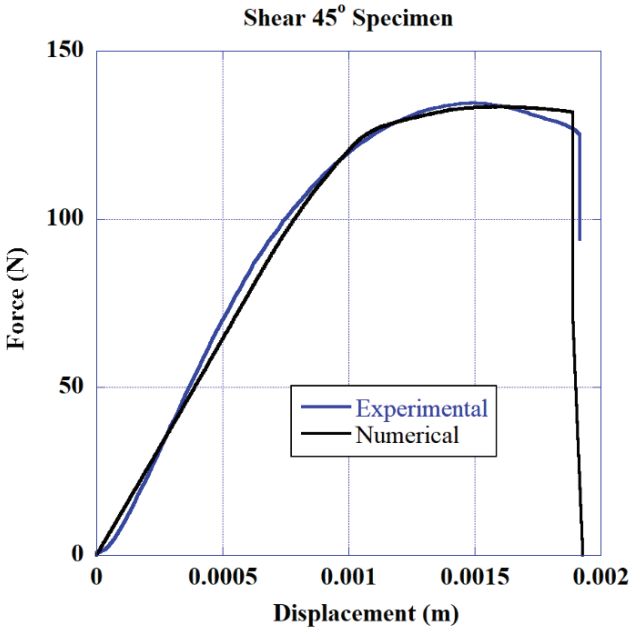


Figure 72 Experimental vs. single case optimization force–displacement curves of the shear 45° specimen.

Then the comparison of the multi case optimization and the experimental force vs. displacement curves of shear 45° sample is illustrated in Figure 73. In multi case optimization, the displacement values were consistent with the experimentally achieved results but force decreased earlier than in the experiment.

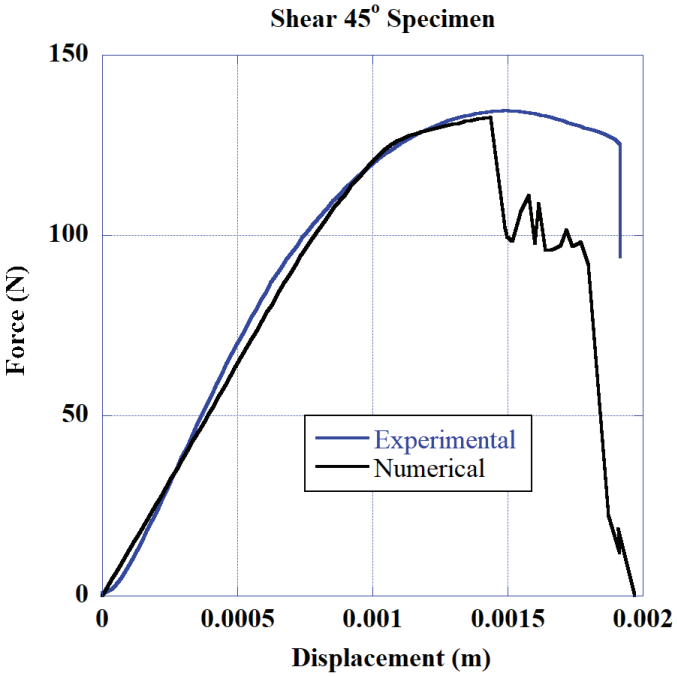


Figure 73 Experimental vs. multi case optimization force–displacement curves of the shear 45° specimen.

Figure 68 presents the failure of the shear 45° specimen used in the experiment and the simulations. A good correspondence was observed in both of the single and multi case optimizations with the experiment in terms of appearance of the deformation.

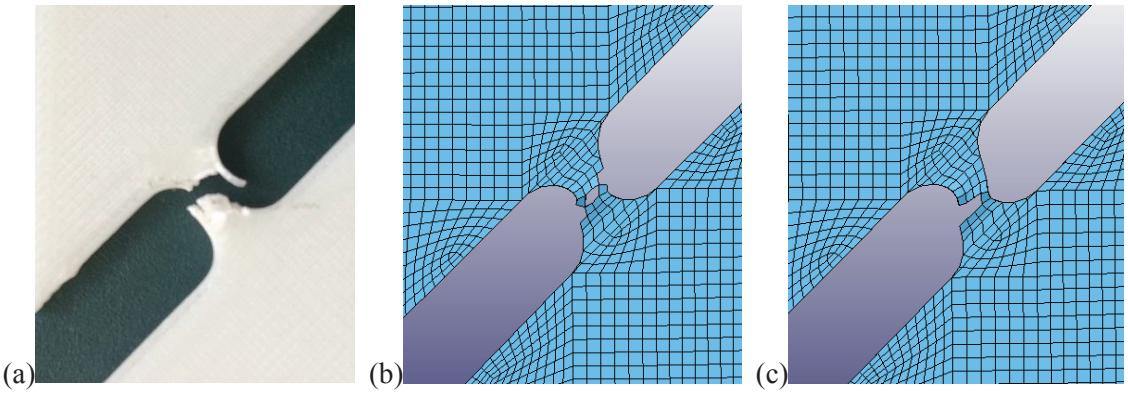

Figure 74 The state of failure of the shear 45° specimen in (a) experiment (b) single case optimization and (c) multi case optimization.

### 4.3.1.6 Mini Tensile

Peak force and displacement values of the mini tensile specimen are recorded approximately as 485 N and 4.8 mm respectively. The fitted force displacement curves From single case optimization with the experiment is illustrated in Figure 75.

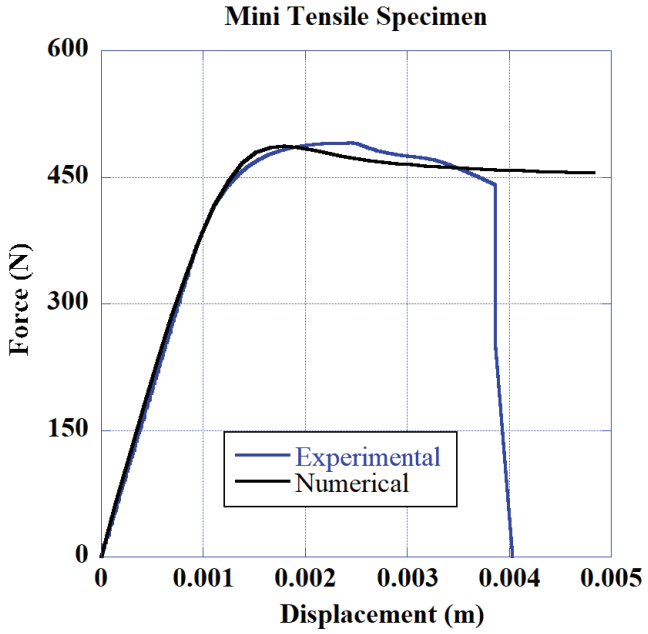


Figure 75 Experimental vs. single case optimization force–displacement curves of the mini tensile specimen.

There was a good agreement between the single case optimization and experimental data in terms of peak force value but specimen in the simulation exhibited more brittle behavior and failed 0.8 mm earlier than in the experiment.

Then the multi case optimization results for the mini tensile specimen is presented in together with the experimental data. The value of the peak force was consistent with the experimental data but specimen showed more brittle behavior and failed earlier than in the experiment.

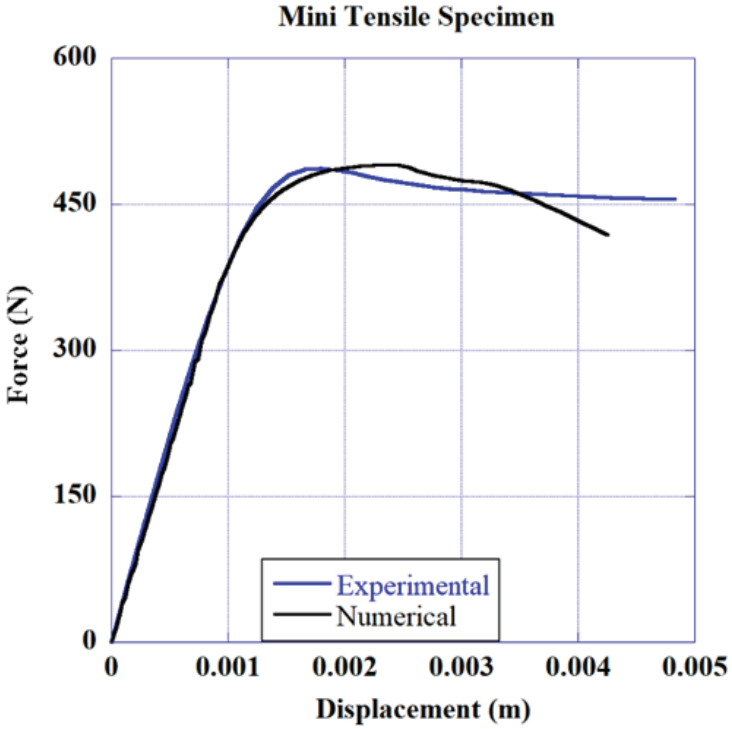


Figure 76 Experimental vs. multi case optimization force vs. displacement curves of the mini tensile specimen.

The failure of the mini tensile specimen used in the experiment and the simulations is presented in Figure 77. The appearance of the deformation was well predicted in both of the single and the multi case optimizations.

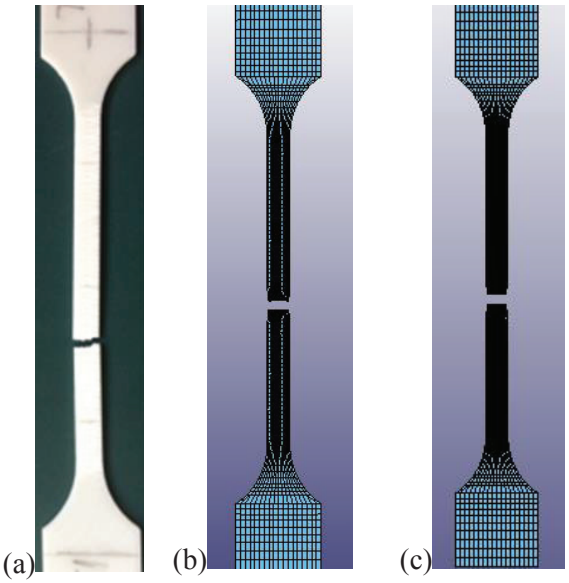


Figure 77 The state of failure of the mini tensile specimen in (a) experiment (b) single case optimization and (c) multi case optimization.

Once it was observed that models were showing good correlation between simulations and experimental results, fading exponent, damage exponent and the instability and failure curves achieved from combined LS-OPT analysis were implemented to the gas gun and SHTB simulations to get more accurate results and to validate the parameter values.

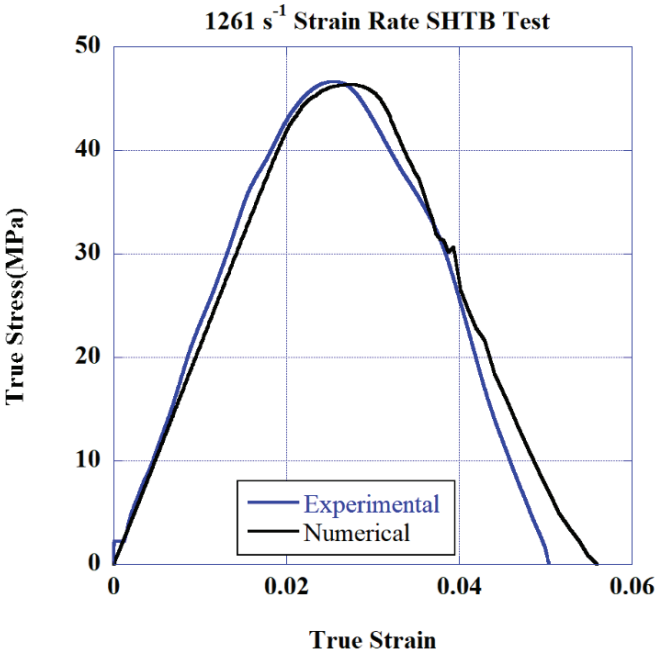


(a)

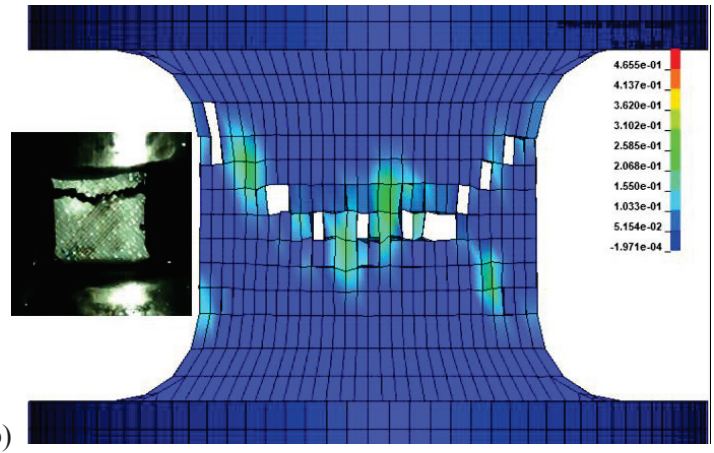


(b)

Figure 78 Comparison of experimental and numerical (a) true stress strain curves (b) appearance of failure for the SHTB test

As it seen in Figure 78.a with the use of GISSMO criteria, correlation was observed between the simulation and experiment in terms of failure strain and failure stress values. A good correspondence was displayed in Figure 78.b in terms of appearance of the failure of both the simulated specimen and the experimental.

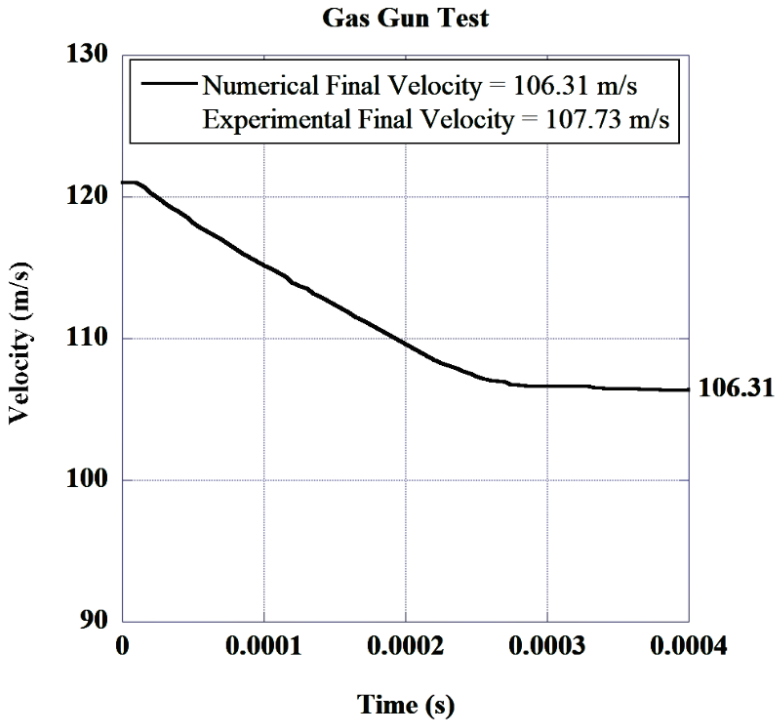


(a)

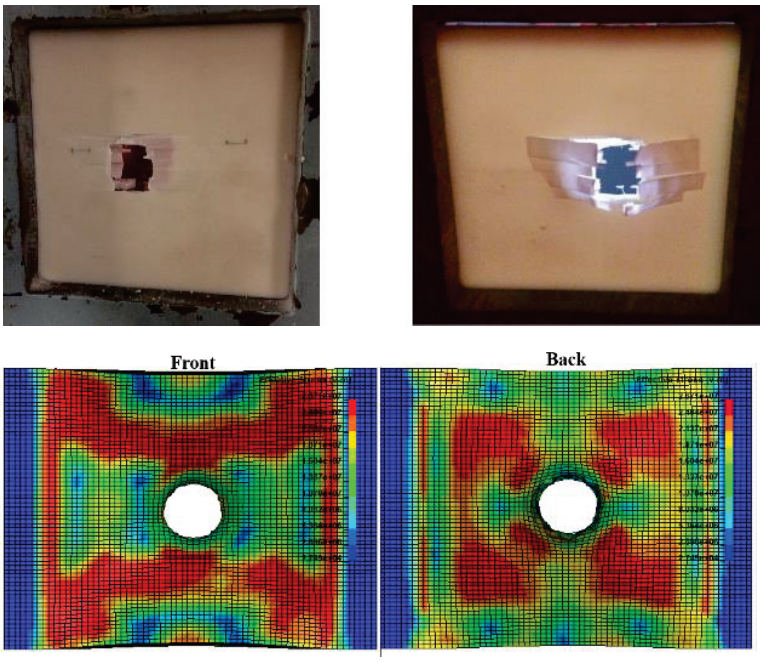


(a)

Figure 79 Experimental and numerical comparison of (a) initial and final velocity of the projectile (b) deformation on the front and back face of the plate.

Initial and final velocity of the projectile in the numerical model is presented in Figure 79.a. Experimental and numerical final velocity of the projectile correlated well with using of GISSMO criteria. As it is seen in Figure 79.b good correspondence between the numerical and experimental results was observed for the appearance of the deformation. GISSMO damage model showed good correlation for also the gas gun and SHTB test data and was able to catch the failure characteristics of the FDM built ABS polymer.

Elastic triaxiality values for the different specimens are presented in Table 7. After the elastic region, triaxiality values were not able to stay constant and changed throughout the simulation in each case. As it was stated in the study of Chen et al. finding the parameters for the GISSMO critera by an optimisation tool, LS-OPT was an efficient way.

Table 7 Elastic triaxiality values for the different specimens (Effelsberg et al. 2012)

| | **Shear 0°** | **Shear 45°** | **Shear 60°** | **Notch** | **Double Notch** | **Mini Tensile** |
|---|---|---|---|---|---|---|
| **Elastic Triaxiality** | 0.000 | 0.197 | 0.283 | 0.395 | 0.515 | 0.333 |

The results for both of the single and multi case optimizations matched well with the experiments in appearance and occurrence of the failure. Single case fittings were slightly better than the combined analyzes. In the study of Hörling et al. with the use of GISSMO card for the steel, better agreement was observed between tests and simulations when the specimens are optimized individually. But in the current study, combined optimizations were found to be more advantageous because this way, common parameter values were found for all of the cases. These parameter values were used in different loading cases and successfully correlated with the experiments in terms of the necking and localization of deformation behavior.

# CHAPTER 5

# CONCLUSIONS

This investigation focuses on identifying suitable material models that fulfil the need of representation of static and dynamic constitutive behaviour of the FDM built ABS plastics and determination of the material model constants.

In accordance with this purpose, quasi-static and high strain rate experimental test were performed on the FDM built ABS material and results were presented. Static and dynamic experimental study proceeded with the determination of material model parameters. *MAT_024, *MAT81 and *MAT_187 computational constitutive material models were selected to characterize static and dynamic behavior of the FDM built ABS plastic. Numerical simulations were performed in LS-DYNA software. Altair HyperMesh and Ls-PrePost programs were used as a preprocessor in the modeling study.

The compressive and tensile stress–strain behaviors of the material were found to be strain rate sensitive and the modulus of elasticity and maximum stress increased with increasing strain rate.

Following these, numerical models were developed and comparisons of the material models were conducted for all cases. Results showed that, in the case of quasi-static tensile test, there was a good correspondence between the simulation and experiment in terms of failure stress and good agreement was observed on the localization of the deformation. *MAT_24 and *MAT_187 models predicted the failure strain values but *MAT_81 model acted more brittle than reality and failed earlier than in the experiment. And in the case of quasi-static compression test, good correspondence was observed for all three material models, in terms of yield point. In the densification region, *MAT_187 model displayed inconsistent behavior.

In the case of the SHTB test, numerical models were successfully correlated with the experiment in terms of tensile strength. But results were not satisfying for the prediction of damage initiation and progression. And in the case of SHPB test, good agreement was observed between the simulations and experiment in terms of maximum stress and maximum loading values.

In order to improve these models and to catch the failure behavior of the material

for different load cases, the Generalized Incremental Stress-State-dependent Model (GISSMO) was implemented. Thus, the fading exponent, damage exponent and the instability and failure curve of the material were found by LS-OPT. First the optimization was done for each case individually to find the initial values for the combined optimization. Then, the optimization was done for six specimen types at the same time and common parameter values were found for all cases.

Results showed that when GISSMO parameters were optimized for a single case there were better potential predicting the damage comparing to combined optimization. But combined optimization presents global parameter values for FDM built ABS. Multi case optimization would probably show better results if number of iterations were increased but the simulations took more or less two weeks so it would be a time consuming problem. Nonetheless, found parameter values were reasonable, considering fading exponent and damage exponent values for a perfectly plastic material are 8.0 and 2.0, respectively (Tabacu and Ducu 2020). These implied that there was potential in predicting the failure characteristics of the material for different loading cases. Therefore parameter values obtained from multi-case optimization were implemented to the gas gun and SHTB simulations for validation. GISSMO damage model showed good correlation for also the gas gun and SHTB tests, eventually.

# REFERENCES


Ahn, Sung-Hoon, Michael Montero, Dan Odell, Shad Roundy, and Paul K %J Rapid prototyping journal Wright. 2002. 'Anisotropic material properties of fused deposition modeling ABS'.

Alejano, Leandro R., and Antonio Bobet. 2012. 'Drucker–Prager Criterion', *Rock Mechanics and Rock Engineering*, 45: 995-99.

Andrade[1], Filipe, Markus Feucht, and Andre Haufe[1]. 2014. 'On the Prediction of Material Failure in LS-DYNA®: A Comparison Between GISSMO and DIEM'.

Aydar, Alev Yüksel. 2018. 'Utilization of response surface methodology in optimization of extraction of plant materials', *Statistical approaches with emphasis on design of experiments applied to chemical processes*: 157-69.

Bertarelli, Alessandro. 2016. 'Beam-induced damage mechanisms and their calculation', *arXiv preprint arXiv:1608.03056*.

Cantrell, Jason T, Sean Rohde, David Damiani, Rishi Gurnani, Luke DiSandro, Josh Anton, Andie Young, Alex Jerez, Douglas Steinbach, and Calvin Kroese. 2017. 'Experimental characterization of the mechanical properties of 3D-printed ABS and polycarbonate parts', *Rapid Prototyping Journal*.

Cinelli, Lucas, Gabriel Chaves, and Markus Lima. 2018. *Vessel Classification through Convolutional Neural Networks using Passive Sonar Spectrogram Images*.

co., https://sgprototype.en.made-in-china.com/ SG Prototype manufacturer. 2019.

Croccolo, Dario, Massimiliano De Agostinis, and Giorgio Olmi. 2013. 'Experimental characterization and analytical modelling of the mechanical behaviour of fused deposition processed parts made of ABS-M30', *Computational Materials Science*, 79: 506-18.

Crump, S Scott. 1991. 'Fast, precise, safe prototypes with FDM', *ASME, PED*, 50: 53-60.

Dawoud, Michael, Iman Taha, and Samy J %J Journal of Manufacturing Processes Ebeid. 2016. 'Mechanical behaviour of ABS: An experimental study using FDM and injection moulding techniques', 21: 39-45.

Diaconescu, Claudiu, Stefan Tabacu, and Alexandru Oltean. 2017. 'Design and Analysis of a Fused Deposition Modelling Manufactured Part', *IOP Conference Series: Materials Science and Engineering*, 252: 012040.

Dizon, John Ryan C, Alejandro H Espera Jr, Qiyi Chen, and Rigoberto C Advincula. 2018. 'Mechanical characterization of 3D-printed polymers', *Additive Manufacturing*, 20: 44-67.

Edgar, Jonathan, and Saxon Tint. 2015. 'Additive manufacturing technologies: 3D printing, rapid prototyping, and direct digital manufacturing', *Johnson Matthey Technology Review*, 59: 193-98.

Effelsberg, J, A Haufe, M Feucht, F Neukamm, and P Du Bois. 2012. "On parameter identification for the GISSMO damage model." In *12th International LS-DYNA Users Conference*, 1-12. Metal Forming.

Erhart, Tobias. 2016. 'Tips and tricks for successful implicit analyses with LS-DYNA', *Dynamore GmbH 2016*.

Hallquist, John o. 2006. 'LS-DYNA theory manual', *Livermore software Technology corporation*.

Hörling, Daniel. 2015. "Parameter identification of GISSMO damage model for DOCOL 1200M: A study on crash simulation for high strength steel sheet components." In.

International, ASTM. 2015. *ASTM D638-14, Standard Test Method for Tensile Properties of Plastics* (ASTM International).

Jami, Hesamodin, Syed H Masood, and WQ Song. 2013. "Dynamic response of FDM made ABS parts in different part orientations." In *Advanced Materials Research*, 291-94. Trans Tech Publ.

Kazmer, David. 2017. 'Three-dimensional printing of plastics.' in, *Applied Plastics Engineering Handbook* (Elsevier).

Kucewicz, Michał, Paweł Baranowski, Jerzy Małachowski, Arkadiusz Popławski, Paweł %J Materials Płatek, and Design. 2018. 'Modelling, and characterization of 3D printed cellular structures', 142: 177-89.

Lemaitre, Jean. 1985. 'A Continuous Damage Mechanics Model for Ductile Fracture', *Journal of Engineering Materials and Technology*, 107: 83-89.

LSTC. 2020. 'Ls-Dyna Keyword Users's Manual.'", *LS-DYNA R12.0 Keyword User's Manual*, II: 608-09.

Macdonald, Eric, Rudy Salas, David Espalin, Mireya Perez, Efrain Aguilera, Dan Muse, and Ryan B Wicker. 2014. '3D printing for the rapid prototyping of structural electronics', *IEEE access*, 2: 234-42.

Neukamm, Frieder, Markus Feucht, and André Haufe. 2009. 'Considering damage history in crashworthiness simulations', *Ls-Dyna Anwenderforum*.

Peterson, Alex, Denzell Bolling, Adewale Olasumboye, Ed Habtour, Jaret C Riddick, Michael Coatney, and Gbadebo Owolabi. 2015. "Dynamic Behavior of Acrylonitrile Butadiene Styrene Under Impact Loads." In *ASME International Mechanical Engineering Congress and Exposition*, V009T12A01. American Society of Mechanical Engineers.

Rankouhi, Behzad, Sina Javadpour, Fereidoon Delfanian, and Todd Letcher. 2016. 'Failure Analysis and Mechanical Characterization of 3D Printed ABS With Respect to Layer Thickness and Orientation', *Journal of Failure Analysis and Prevention*, 16: 467-81.

Reithofer, P., A. Fertschej, B. Hirschmann, B. Jilka, and M. Rollant. 2018. "Material Models For Thermoplastics In LS-DYNA® From Deformation To Failure." In.

Sood, Anoop Kumar, Raj K Ohdar, and Siba S Mahapatra. 2010. 'Parametric appraisal of mechanical property of fused deposition modelling processed parts', *Materials & Design*, 31: 287-95.

Tabacu, Stefan, and Cătălin Ducu. 2020. 'Numerical investigations of 3D printed structures under compressive loads using damage and fracture criterion: Experiments, parameter identification, and validation', *Extreme Mechanics Letters*, 39: 100775.

Tabacu, Stefan, and Cătălin %J Thin-Walled Structures Ducu. 2018. 'Experimental testing and numerical analysis of FDM multi-cell inserts and hybrid structures', 129: 197-212.

Tasdemirci, A, and G Tunusoglu. 2017. 'Experimental and numerical investigation of the effect of interlayer on the damage formation in a ceramic/composite armor at a low projectile velocity', *Journal of Thermoplastic Composite Materials*, 30: 88-106.

Vaezi, Mohammad, Hermann Seitz, and Shoufeng Yang. 2013. 'A review on 3D micro-

additive manufacturing technologies', *The International Journal of Advanced Manufacturing Technology*, 67: 1721-54.

Wang, Gary, and S. Shan. 2007. 'Review of Metamodeling Techniques in Support of Engineering Design Optimization', *Journal of Mechanical Design - J MECH DESIGN*, 129.

Wang, Xin, Man Jiang, Zuowan Zhou, Jihua Gou, and David Hui. 2017. '3D printing of polymer matrix composites: A review and prospective', *Composites Part B: Engineering*, 110: 442-58.

Witowski, Katharina, Markus Feucht, and Nielen Stander. 2011. "An effective curve matching metric for parameter identification using partial mapping." In *8th European LS-DYNA, Users Conference Strasbourg, pgs*, 1-12.

Zhang, Xiong, Zhen Chen, and Yan Liu. 2017. 'Chapter 6 - Constitutive Models.' in Xiong Zhang, Zhen Chen and Yan Liu (eds.), *The Material Point Method* (Academic Press: Oxford).